The multi-phase interstellar medium in a high resolution simulation of a dwarf starburst

Konstantina Maria Fotopoulou

München 2022

The multi-phase interstellar medium in a high resolution simulation of a dwarf starburst

Konstantina Maria Fotopoulou

Dissertation
der Fakultät für Physik
der Ludwig-Maximilians-Universität
München

vorgelegt von
Konstantina Maria Fotopoulou
aus Marousi, Griechenland

München, den 30.09.2022

Erstgutachter: Prof. Dr. Volker Springel

Zweitgutachter: Prof. Dr. Simon D.M. White

Tag der mündlichen Prüfung: 16.12.2022

Contents

List of Figures

List of Tables

Zusammenfassung

Wir präsentieren die Ergebnisse der Analyse des multiphasigen interstellaren Mediums (eng: interstellar medium, ISM) in einer hydrodynamischen Simulation einer gas-reichen Zwerggalaxie Verschmelzung, aufgelöst mit individuellen massiven Sternen bei subparsec (0.1 pc) räumlicher Auflösung und Sonnenmassen (4 $M_\odot$) Massenauflösung. Die Simulation bekräftigt ein schnelles Disruptionsmodel für sternformende Wolken durch stellarer Strahlung und Supernova Feedback.

Unsere Analyse des multiphasigen ISM offenbart eine erweiterte Sternentstehungsexplosion in Raum und Zeit. Sternentstehung tritt durchweg auf, selbst bei großen Distanzen zum Zentrum des Systems (d.h. $r = 5$ kpc) und während der gesamten Simulationszeit (457 Myr). Dies demonstriert, dass die erweiterte Sternentstehungsexplosion in unserem System Ausflüsse generiert, die insuffizient darin sind das gesamte Gasreservoir, in dem sich Sterne formieren, über den Zeitraum der Simulation hinweg zu erschöpfen. Die Sternentstehungsrate $\dot{M}_*$ (eng: star formation rate, SFR) folgt dem Verhalten der Ausflussrate $\dot{M}_{\rm out}$ (eng: outflow rate, OFR). Die Ausflussraten, gemessen bei variierenden Entfernungen vom Zentrum, sind größer je näher sie dem Zentrum sind. Der Massenverbrauchsfaktor η ist von Größenordnung über 1. Die "warme" Phase des ISM ($300\,{\rm K} \leq T_{\rm gas} < 2 \times 10^4$ K) zeigt die stärksten Ausflüsse auf, welche primär atomaren Wasserstoff (H) und ionisierten Wasserstoff (H+) beschleunigen. Metalle werden ebenfalls vom Ausfluss rausgetragen, speziell bei Temperaturen $2 \times 10^4\,{\rm K} \leq T_{\rm gas} < 2 \times 10^5$ K ("warm-heiße" Phase)

Die erweiterte Sternentstehungsexplosion hat signifikante Auswirkungen auf die Morphologie und Evolution des Systems. Die kalte, sternformende Phase ($T_{\rm gas} < 300$ K) ist durch die Sternentstehungsexplosion in kompakte Klumpen und Filamente strukturiert. Wir identifizieren Hunderte von kalten Wolken in jedem Schnappschuss der Simulation mit typischen irregulären Strukturen, Massen und Größen von Molekülwolken und wir verfolgen deren Lebenszyklus. Die simulierten kalten Wolken folgen einer Potenzgesetzmassenfunktion (eng: cloud mass function, CMF): $dN/dM \propto M^\alpha$ mit $\alpha_{\rm mean} = -1.78(\pm 0.08)$, was gut in Übereinstimmung mit Beobachtungen ist. Die Steigung α bleibt konstant während der gesamten Simulationszeit hinweg und ist ungefähr dieselbe für verschiedene Gasteilchen Dichtegrenzwerte, was indikativ für selbstähnliche Strukturen ist. Die Eigenschaften der simulierten kalten Wolken folgen den Larson-Relationen und sind durchaus in Übereinstimmung mit Beobachtungen. Beim Verfolgen des Lebenszyklus der kalten Wolken identifizieren wir die Wachstumsphase, in der die Wolken

genug Masse ansammeln für gravitativen Kollaps und dem Beginn von Sternentstehung, sowie die Zerstörungsphase, in der die Energie- und Impulseinspeisung der neu entstandenen Sternen zur Dispersion der Wolke führt. Wir finden Korrelationen zwischen der maximalen Masse und Ausdehnung der kalten Wolken, wenn sie ihre Maximalmasse erreichen: $R_{M_{\rm max}} \propto M_{\rm max}^{1/2}$. Hochmassige Wolken leben länger (bis zu 8 Myr) als geringmassige Wolken mit einer Maximalmasse von $M_{\rm max} < 10^4 {\rm M}_\odot$. Sie beschreiben eine Potenzgesetzlebenszeitverteilung von $\tau_{\rm life} \propto M_{\rm max}^{0.3}$. Schlussendlich entwickeln sich diese kalten Wolken in Sternhaufen mit wohl definierten Umlaufbahnen, sowie Lebensspannen von bis zu 300 Myr und Massen bis zu 10^5 $\rm M_\odot$.

Abstract

We present the results of the analysis of the multi-phase interstellar medium (ISM) in a hydrodynamical simulation of a gas-rich dwarf galaxy merger resolved with individual massive stars at sub-parsec (0.1 pc) spatial and solar-mass (4 $M_\odot$) mass resolution. The simulation supports a rapid disruption model for star-forming clouds by stellar radiation and supernova feedback.

Our analysis of the multi-phase ISM reveals an extended starburst in space and time. Star formation continues to occur even at great distances from the centre of the system (i.e. r = 5 kpc) and during the whole time of the simulation (457 Myr). This demonstrates that the extended starburst in our system generates outflows that are insufficient to completely deplete the gas reservoir, where stars are formed, during the time of the simulation. The star formation rate $\dot{M}_*$ (SFR) follows the behaviour of the outflow rate $\dot{M}_{\rm out}$ (OFR).

The outflow rates measured at various distances from the centre are higher closer to the centre with mass loadings η above unity. The "warm" phase of the ISM (300 K $\leq T_{\rm gas} < 2\times10^4$ K) exhibits the strongest outflows, which primarily accelerate atomic (H) and ionised (H+) hydrogen. Metals are also carried out by the outflows, especially at temperatures: 2×10^4 K $\leq T_{\rm gas} < 2\times10^5$ K ("warm-hot" phase).

The extended starburst impacts significantly the morphology and the evolution of the system. Due to the starburst, the cold ($T_{\rm gas} < 300$ K) star-forming gas is structured in compact clumps and filaments. We identify hundreds of cold clouds in each snapshot of the simulation with the typical irregular structure, masses and sizes of molecular clouds and we trace their life cycle. The simulated cold clouds follow a power law mass function (CMF): $dN/dM \propto M^\alpha$ with $\alpha_{\rm mean} = -1.78(\pm0.08)$, well in agreement with the observations. The slope α remains constant throughout the time of the simulation and is roughly the same for different gas particle density thresholds indicating self-similar structure. The simulated cold cloud properties follow the Larson relations and are well in agreement with observations.

Tracing the life cycle of the cold clouds we identify the growth phase, when the clouds gain enough mass for gravitational collapse and the beginning of star formation, and the destruction phase, when the energy and momentum input from newly formed stars lead to the dispersal of the clouds. We find a correlation between the peak mass and the size of the cold clouds when they reach their peak mass: $R_{M_{\rm max}} \propto M_{\rm max}^{1/2}$. High mass clouds live longer (up to 8 Myr) than lower mass clouds with peak mass $M_{\rm max} < 10^4 M_\odot$ which follow a power law lifetime distribution

$\tau_{\rm life} \propto M_{\rm max}^{0.3}$. Eventually, these cold clouds evolve into star clusters which maintain well-defined orbits for the course of their existence and have lifespans up to 300 Myr and masses of up to 10^5 $M_\odot$.

Acknowledgements

Many people have, in their own way, helped me in carrying out this project. First of all, I am most grateful to my supervisor Dr. Thorsten Naab for his unwavering support for the past four years. Aside from purely academic advice, his understanding and assistance throughout our collaboration helped to maintain my motivation even during moments of the most crippling self-doubt.

Likewise, I am grateful to the other two members of my thesis committee, Prof. Dr. Volker Springel and Prof. Dr. Eiichiro Komatsu, who have not only been keen on offering valuable feedback and advice on the project but were also remarkably supportive even when (I felt) my progress was not enough. All three created an amicable and reassuring academic environment that allowed me to work unobstructed. Needless to add, their comments and criticism greatly contributed to the final form of this thesis. Special thanks are also due to Prof. Dr. Stefanie Walch-Gassner for allowing me to work with her group and for generously sharing her insights. Finally, I am forever indebted to Prof. Dr. Kalliopi Dasyra for her unceasing guidance and encouragement from the earliest stages of my academic journey.

This latest journey would have been far more turbulent if it weren't for the generous assistance of many colleagues. I am most obligated to Dr. Ulrich Steinwandel for his assistance across many fronts: from helping me during the very early stages of my work at the Max Planck Institute for Astrophysics (MPA) and dealing with frustrating technical issues to engaging in stimulating discussions and offering me solid advice. Many thanks are also due to Miha Cernetic for the ample technical assistance he has provided me with and his great contribution to developing the tools I used in my analysis. Special thanks to Dr. Natalia Lahén for letting me post-process her rich simulation and for her overall assistance.

During my studies at MPA, I was lucky enough to share space and time with some of the most friendly and caring people I have known. I am grateful to fellow research group members and dear friends Eirini Batziou, Jessica May Hislop, Francesco Rizzuto, Matteo Frigo, Chris Byrohl and Timo Halbesma for their invaluable academic and psychological support. The working environment and the moments we shared made Munich feel a lot less gloomy than during the first days of my arrival. Special thanks to Linda Baronchelli, Vlas Sokolov and Stavros Dimitrakoudis

for our awesome DnD sessions!

Understandably, this account would be incomplete if it did not include my closest friends and family back in Greece. I am thankful to Dimitrios Athanasiou for his understanding and support while going through the same problems as me in solidarity, George P. Goulas, well. . . for being George and Haris Tzerefos for always being there for me when it mattered (and not) for the past ten years.

I am most grateful to my loving parents, Tatiana and Paraskevas, whose sheer dedication to me and my dreams made this one can come true and to my little sister Athanasia-Eirini for being the absolute best throughout these challenging years. It is only fitting that this work is dedicated to her.

My warmest thank you is due to Dr. Tim-Eric Rathjen for making life in Germany a lot more special than I had ever imagined. Thank you Tim for your rich academic insights, for the ample help in frustrating coding issues, for your unwavering faith in my capabilities, for being there no matter what, for Tuesdays and for new adventures...

This work is dedicated to my sister, Athanasia-Eirini

Somewhere, something incredible is waiting to be known...
Carl Sagan

Chapter 1

Introduction

1.1 The multi-phase interstellar medium (ISM)

There is a common perception that outer space is a complete void. In fact, among the stars there is a huge amount of matter and radiation that we call interstellar medium (ISM). The ISM[1] is defined as "everything that fills the space between the stars". It comprises of baryonic matter in the form of gas and dust, as well as electromagnetic radiation, cosmic rays, the interstellar magnetic field, the gravitational field and dark matter.
The presence of interstellar material is less obvious than the presence of stars, because the mass contained in stars has been condensed by gravity, creating a dense state immediately observable. In contrast, interstellar material is very sparsely distributed over vast distances within galaxies, with a dilution greater than any artificial vacuum that can be achieved in terrestrial laboratories. In the cold, denser ISM regions, matter is mainly in molecular form, with a number density of 10^6 cm^{-3}, while in warmer and thinner regions, matter is primarily ionised at densities as low as 10^{-4} cm^{-3} (Draine, 2011). In terms of mass, 99% of the ISM is in the form of gas whereas 1% is dust.
The ISM does not exist in isolation but is embedded in the circumgalactic medium (CGM). Parts of the gas which is transported out of the ISM via outflows can accumulate in the CGM, condense and cool down and then "fountain" back onto the ISM, replenishing the baryonic material and closing the matter cycle again. Even though a large amount of the total baryonic matter resides in the CGM, no star formation activities have yet been detected in that regime (Tumlinson et al., 2017).

[1] In the context of this work we will refer to the interstellar medium with the international abbreviation ISM.

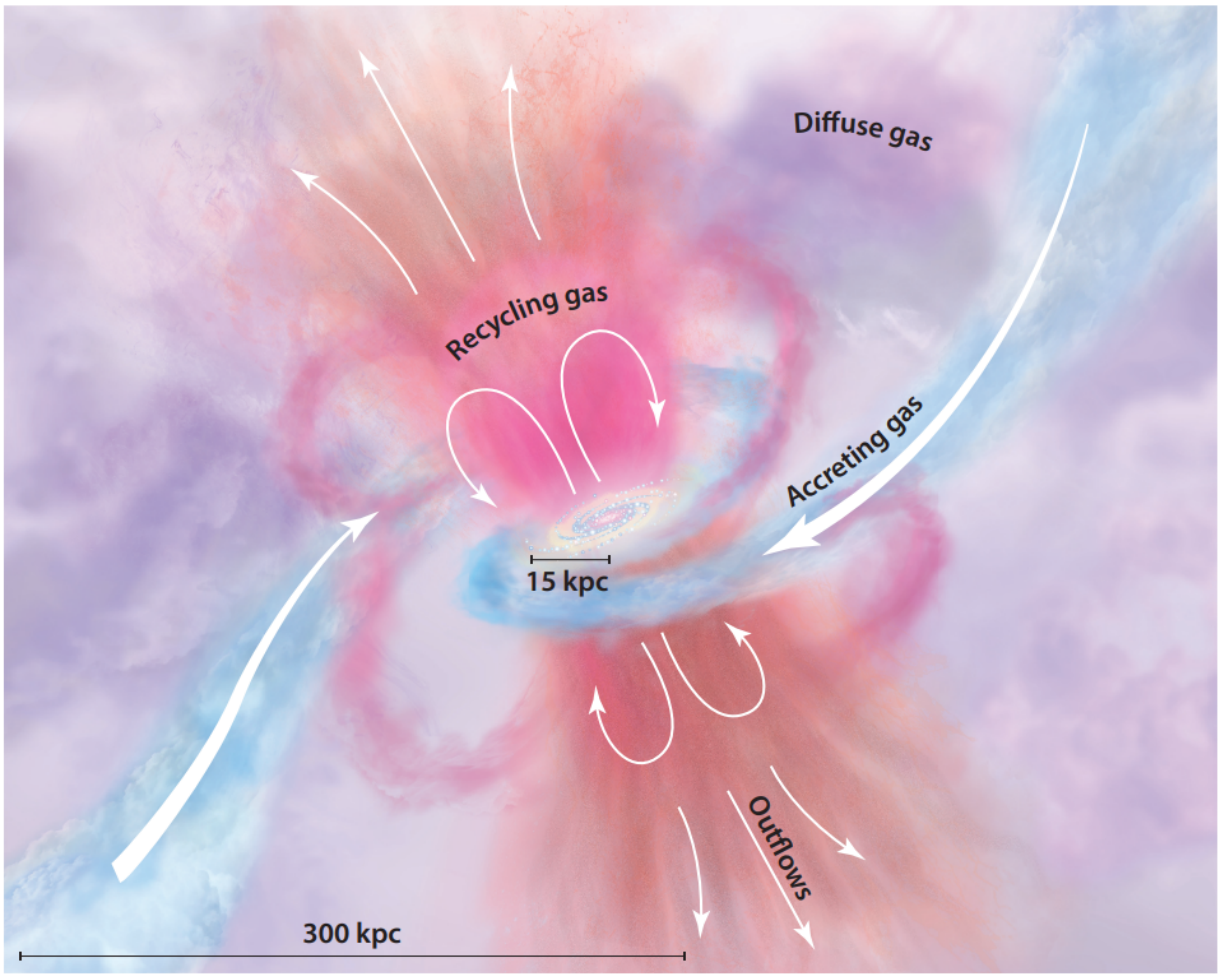

Figure 1.1: Illustration of the baryonic matter cycle in the CGM/ISM, taken from Tumlinson et al. (2017), their Figure 1.1. The colours indicate the metallicity of the gas where blue hues represent metal-poor and red hues metal-enriched gas. In addition to the "recycled" gas through the inflow/outflow boundary between the CGM and ISM, the galaxy can also replenish its ISM gas reservoir by accreting pristine gas from the intergalactic medium (IGM).

1.1.1 Gas component of the interstellar medium

In this work, we are predominantly interested in the study of the ISM gas component, since we focus on the formation, the evolution and the properties of simulated cold star-forming clouds and galactic outflows. The ISM gas is composed roughly out of 70% hydrogen (H), 28% helium (He) and 2% metals (C, O, N, etc) by mass. This shows that the chemical composition of the ISM gas is similar to the chemical composition of stars, which is known by studying the absorption and emission spectra of stellar atmospheres. This fact should not be surprising since the cold dense gas is the medium of star formation in galaxies. The ISM is not uniform, but multi-phase, comprised of gas with different temperatures and in different structures. The regions of interest in the ISM are characterised by the state of hydrogen, i.e. the so-called different "phases" of the ISM. Historically, the first theoretical model of a multi-phase ISM was proposed by Field et al. (1969) who introduced a two phase equilibrium model in order to explain the observed properties of the ISM. In their model, the ISM comprised of a warm diffuse phase with temperature $T \sim 10^3$ K known as: warm neutral medium (WNM) and a cold dense phase with temperature $T \sim 100$ K, known as: cold neutral medium (CNM). In this model, the two phases are in pressure equilibrium which has been observationally confirmed (see e.g. Wolfire et al., 2003; Cox, 2005) and gas particles can move between the phases by heating up or cooling down. McKee & Ostriker (1977) added a third dynamic phase comprising of hot tenuous ionised gas with temperature $T \sim 10^6$ K which is created when the CNM and the WNM get heated by supernova (SN) blast-waves and is known as: hot ionised medium (HIM). Due to the long cooling times of such high temperatures this phase is also considered stable. Observational data of synchrotron emission (Hoyle & Ellis, 1963), diffuse interstellar [O II] emission (Mierkiewicz et al., 2006) and faint galactic Hα and [N II] emission lines (Reynolds et al., 1973) revealed a fourth phase in the ISM with temperature $T \sim 10^4$ K known as: warm ionised medium (WIM). Unlike the shock-heated HIM, the WIM is produced through photoionisation by ultraviolet (UV) photons from hot massive O-type stars. If the photons of these stars ionise dense hydrogen gas in a cloud then this photoionised gas is referred to in the literature as an "H II region", whereas the less dense photoionised gas is called "diffuse H II". By and large, a broad picture of the ISM would be one of cool gas clouds embedded in a sea of warm and hot inter-cloud gas (Cox, 2005; Draine, 2011).
The different phases of the ISM are summarised bellow and in table 1.1:

Ionised gas

High temperature ionised hydrogen that can be further divided in **hot ionised medium (HIM)**: tenuous shock-heated gas by blast-waves from supernova (SN) explosions, collisionally ionised and **warm ionised medium (WIM)**: gas photoionised by UV photons from hot O-type stars. The warm ionised medium can be further divided into **H II regions**: dense material associated with regions of star formation, i.e. bright nebulae and **diffuse H II**: extended, lower density inter-cloud medium. Most cooling mechanisms are very inefficient at the high temperatures ($T \geq 10^{5.5}$ K) of

the hot ionised gas. The main cooling channels for this gas phase is adiabatic expansion and X ray emission, which is also the main observational tracer for the HIM. Additionally, radio synchrotron emission can be detected from the HIM. The photoionised WIM has a typical temperature of $T \approx 10^4$ K and can cool via optical and fine structure line emission. One of the most efficient coolants for the WIM is the fine structure line emission of C^+. The WIM is easily observable via optical recombination lines like Hα and Hβ or classical forbidden emission lines like [O III] and [N II].

Atomic gas

It is atomic hydrogen gas that can be divided in **warm neutral medium (WNM)**: diffuse H I gas with temperature $T \sim 10^{3.7}$ K and **cold neutral medium (CNM)**: H I gas bound in clouds with temperature $T \sim 10^2$ K). Photoelectric heating of dust grains which are thermally coupled to the gas is the main heating process of the atomic gas in the ISM. The most prominent line to observe the atomic ISM is the hyperfine transition of hydrogen (21-cm line) with $\lambda = 21$ cm and $\nu = 1420$ Mhz. This line can be observed as an emission or an absorption line. Even though this forbidden line transition only carries energy of $\sim 5 \times 10^{-6}$ eV and has a transition rate of $\sim 3 \times 10^{-15}$ s^{-1}, i.e. a lifetime of ~ 10 Myr, it is an excellent tracer for atomic hydrogen due to the shear vast amount of atomic hydrogen in galaxies. The 21-cm line finds application especially in radio astronomy for the mapping of hydrogen and the measuring of galaxy rotation curves, as well as in cosmology because it is the only emission in the time between recombination and reionisation.

Molecular gas

It is mainly molecular hydrogen and CO gas that can be further divided into **diffuse molecular gas**: gas similar to the cool H I clouds, but with sufficient densities for H_2 self-shielding and **dense molecular gas**: gravitationally bound, star-forming regions. The main heating channels are photoelectric heating by dust and cosmic ray ionisation and heating. Observing CO is possible due to rotational-vibrational lines of the molecule and CO line emission is a major coolant of dense molecular gas. H_2, on the other hand, does not have an electric dipole moment and therefore cannot be observed with allowed electronic transitions. Therefore, H_2 can only be indirectly observed, for example with the CO-to-H_2 conversion factor, χ_{CO} (Bolatto et al., 2013). The correct value of this conversion factor is, however, not generally undisputed and a source of systematic uncertainties. Another possible way of detecting dense molecular gas is via far infrared (FIR) emission of dust, under the assumption that regions of dense cold gas are also hosts for a lot of dust, which is a plausible assumption since dust is the main catalyst for H_2 formation. In Fig. 1.2, we show the major heating and cooling rates per unit volume for the various processes discussed above as a function of gas number density for a initially fully molecular medium, taken from Glover & Clark (2012).

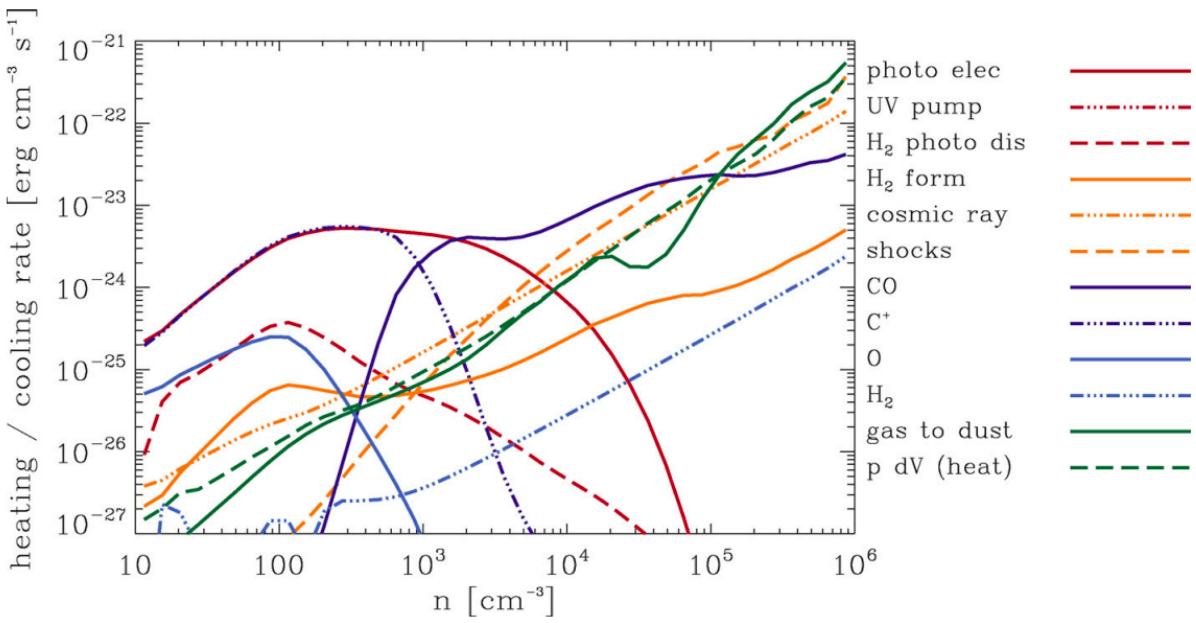

Figure 1.2: Median heating and cooling rates per unit volume for various processes in an initially fully molecular medium as a function of the gas number density, taken from Glover & Clark (2012).

In the following table we summarise the temperatures T, number densities n_H, and volume filling factors (VFF) of each phase in the Milky Way (Draine, 2011; Ferrière, 2001):

Phase	T [K]	n_H [cm^{-3}]	VFF [%]
Hot Ionised	$> 10^5$	~ 0.004	~ 50
Warm Ionised (H II regions & diffuse H II gas)	10^4	$0.2 - 10^4$	~ 10
Warm Atomic/Neutral (H I)	$\sim 5 \times 10^3$	0.6	~ 40
Cold Atomic/Neutral (H I)	~ 100	30	~ 1
Diffuse Molecular (H_2)	~ 50	~ 100	~ 0.1
Dense Molecular (H_2)	$10 - 50$	$10^3 - 10^6$	~ 0.01

Table 1.1: Temperature, T [K], number density, n_H [cm^{-3}], and volume filling factors, VFF, of the different phases of the ISM in the Milky Way (Draine, 2011).

Another useful distinction of the ISM phases can be performed by combining and re-arranging

the aforementioned categories not by the state of hydrogen but by temperature. In this case, we talk about: hot, warm and cold ISM.

- **Hot phase**: H II regions and hot ionised medium.
- **Warm phase**: Warm ionised medium and warm neutral medium.
- **Cold phase**: Cold neutral medium and molecular gas H_2.

The ISM mass is mostly in warm, cold and molecular medium, but the ISM volume is filled with hot ionised, warm ionised and neutral gas (Ferrière, 2001). The cold and the warm phases are in pressure equilibrium (Cox, 2005), the hot medium generated primarily from SN explosions ($T > 10^5$ K) creates a meta-stable phase (McKee & Ostriker, 1977; Ferrière, 2001) and the molecular gas component of the ISM is predominantly found in molecular clouds.

1.1.2 Other baryonic and non-baryonic components

As mentioned previously, the ISM does not only consists of baryonic matter in the gas phase but also of a plethora of other baryonic and non-baryonic components which we briefly discuss here.

Dust

Interstellar dust is a crucial component of the ISM. Dust grains are typically elongated and follow a size distribution with an average size in the order of $\sim \mu$m (Mathis et al., 1977). Dust grains are mainly carbonous or consist of amorphous silicates and are formed in the winds of asymptotic giant branch (AGB) stars, SN ejecta, or even within molecular clouds, even though to a lesser rate. Dust is so very important because of three main features. First, dust grains are the catalysts for molecule formation. On the surface of icy dust grains, single atoms can accumulate and they by chance encounter each other to form molecules, primarily molecular hydrogen H_2. The chance of those encounters is highly increased by the dust (Wakelam et al., 2017). Additionally, metals in the ISM deplete from the gas phase onto the surface of dust grains. The other major contribution from dust is the reprocessing of electromagnetic radiation. Dust grains can absorb radiation with wavelengths smaller than their own extent (e.g. UV radiation) and re-radiate this absorbed energy in the far infrared (FIR) with wavelengths between $5 - 600\mu$m. The last major effect of dust on the ISM is the photo-electric heating of dust grains. High energy photons can collide with dust and eject electrons from the outer shell of the grain. Those electrons will then quickly thermalise with the surrounding medium via further collisions with the gas (Bakes & Tielens, 1994). The photo-electric heating is the major radiative heating process in the ISM over a vast range of densities (see Fig. 1.2.

Starlight

Ultraviolet radiation from stars is the component of the interstellar radiation field (ISRF) with the highest energy density (Draine, 2011). Over the lifetime of a massive star, the integrated UV luminosity is also the largest energy input of a star into the ambient ISM (up to 2 orders of magnitude more energy input than by the SN at the end of the lifetime of the massive star). However, radiation couples only very inefficiently to the gas dynamics of the ambient medium (see e.g. Haid et al., 2018). Nonetheless, starlight is the main driving agent for the chemical evolution of the ISM through photo-ionisation by extreme UV (EUV, $> 13.6\,\mathrm{eV}$)

Cosmic microwave background

The cosmic microwave background (CMB) is the most precisely measured black body radiation in nature with its photon temperature of 2.725 K (Fixsen, 2009). A CMB photon energy density of $0.26\,\mathrm{eV\,cm^{-3}}$ results in a photon number density of $\sim 411\,\mathrm{cm^{-3}}$, which makes CMB photons the most abundant photon species by far. However, even though the CMB is indicative for the cosmological Λ-CDM model, it is of lesser importance for the evolution and dynamics of the local ISM.

Magnetic fields

The ISM is interspersed with magnetic fields which affect the evolution of the ISM to a great extent (see Beck, 2015, for a review). The typical field strength of the ISM magnetic field is in the order of a couple μG to a couple of tens of μG. From a dynamical viewpoint, magnetic fields are the source of another pressure term which can work against gravitational collapse of dense gas structures and therefore reducing the star formation efficiency. Furthermore, magnetic fields govern the large scale motion of cosmic rays which typically have a higher diffusion coefficient along the magnetic field lines (Strong et al., 2007). Observationally, magnetic fields can best be detected by the polarised emission of elongated dust grains which align with the galactic magnetic fields, by radio synchrotron emission of charged particles deflected by the magnetic field, the Zeeman effect (Zeeman, 1897), which describes the splitting of spectral lines in the presence of a magnetic field due to the energy degeneracy of the atomic energy levels, and by Faraday rotation, which describes the measurable rotation of the polarisation plane of electromagnetic radiation when propagating through a magnetic field.

Cosmic rays

Cosmic rays (CR) are ions and electrons at relativistic velocities which propagate through the ISM via streaming, diffusion and advection by gas while gyrating along the magnetic field. The CR energy spectrum spans a staggering range between a couple MeV up to 10^{12} GeV (Aartsen

et al., 2013). However, the majority of galactic CR are relativistic protons with energies in the GeV. The currently most accepted theory for the acceleration of galactic CR is the process of diffusive shock acceleration (also called Fermi acceleration) in supernova remants (Bell, 1978; Dorfi & Breitschwerdt, 2012), in which the charged particles repeatedly oscillate through the shock surface until they reach high enough energies to break out and propagate into the ISM. Cosmic rays cool only very inefficiently via adiabatic expansion and hadronic decay channels, which makes them an important energy reservoir in the ISM. They are suspected to have a strong dynamical impact on galactic outflows (see e.g. Simpson et al., 2016; Girichidis et al., 2018) and are a primary ionisation agent for molecular hydrogen gas, where the self-shielding of the molecules is already high enough to block out most of the UV radiation.

1.1.3 Energies of the ISM

Not only are the gas phases of the ISM in pressure equilibrium but there is also an equipartition of energies, at least in the local solar neighbourhood ISM. Assuming a thermal pressure of $p/k = 3800\,\mathrm{cm^{-3}\,K}$ (Jenkins & Tripp, 2011) the thermal energy density yields $u_{\mathrm{th}} = (3/2)\,nkT = 0.49\,\mathrm{eV\,cm^{-3}}$. The turbulent kinetic energy density, $u_{\mathrm{kin}} = 0.5\,\rho v^2$, gives $u_{\mathrm{kin}} = 0.22\,\mathrm{eV\,cm^{-3}}$ for a hydrogen number density $n_{\mathrm{H}} = 30\,\mathrm{cm^{-3}}$ and root mean square velocity $v_{\mathrm{rms}} = 1\,\mathrm{km\,s^{-1}}$. For a median magnetic field strength $|B| = 6\,\mu\mathrm{G}$ the magnetic energy density yields $|B|^2/8\pi = 0.89\,\mathrm{eV\,cm^{-3}}$ (Heiles & Troland, 2005). The highest energy density is in the cosmic ray component with $u_{\mathrm{CR}} = 1.39\,\mathrm{eV\,cm^{-3}}$ for a CR spectrum which peaks at CR proton energies of 1 GeV, measured by the Voyager spacecraft (Webber & Lockwood, 2001).
Even though the energy densities in the ISM are nearly in equipartition and single gas phases are in pressure equilibrium, the ISM is far from being in a thermodynamic equilibrium. A constant input of energy from stellar feedback keeps the ISM in an nonequilibrium state. However, only a slight amount of energy is retained in the galaxy and most of the injected energy, especially in the form of high-energetic UV photons from starlight, is lost to the cold intergalactic medium (IGM).

1.1.4 Molecular clouds

Molecular gas is strongly linked to star formation (see e.g. reviews by Dobbs et al., 2014; Girichidis et al., 2020). Most stars form in star clusters (Lada & Lada, 2003) which in turn form inside the dense and cold environment of molecular clouds (see e.g. reviews by Fukui & Kawamura, 2010; Kennicutt & Evans, 2012; Heyer & Dame, 2015). In interstellar space the atomic gas is more diffuse and distributed over much greater distances than the molecular, therefore it is more suitable for the dynamical study of galaxies. However, in these less dense regions the X-rays and the gamma rays destroy the molecules and ionise the atoms, thus creating regions of ionised hydrogen H II. On the other hand, molecular gas is less extended and more

dense. This happens because the creation of molecules is enabled in dense concentrations of gas: the "molecular clouds". In other words, the molecular clouds are defined as concentrations of interstellar gas and dust where molecules can form.

As we discussed in section 1.1.1, the most abundant element in the gas component of the ISM is hydrogen, so it does not come as a surprise that the most abundant molecule in molecular clouds is H_2. In more detail, at densities $\eta \geq 100$ cm^{-3} and temperatures $T \sim 10$ K the hydrogen in the interstellar clouds no longer remains in atomic form, but the hydrogen atoms tend to react chemically to form molecules, according to the chemical equation: $H + H \rightarrow H_2$ with the catalytic effect of dust grains. In more detail, the surfaces of the dust grains act as catalysts, offering favourable reaction sites where the excess energy and momentum released during the reaction $H + H \rightarrow H_2$ is absorbed. Furthermore, the newly formed H_2 molecules will be able to survive in the environment of outer space, where UV photons tend to break molecules into atoms, only if they are protected in the dense environment of molecular clouds.

The study of molecular gas is particularly important, because the molecular clouds are the star-forming regions of a galaxy. A cloud will remain in hydrostatic equilibrium as long as the average kinetic energy $\overline{E}_K$ balances its average gravitational potential energy $\overline{E}_U$, i.e. the virial theorem applies:

$$-2\overline{E}_K = \overline{E}_U \tag{1.1}$$

If a cloud is massive enough that the pressure of the gas is not enough to compensate for its gravity, then the cloud will begin to collapse gravitationally, according to the Jeans criterion:

$$2\overline{E}_K < |\overline{E}_U| \tag{1.2}$$

The low temperatures of molecular clouds combined with their high densities favour the fulfilment of the Jeans criterion, i.e. the collapse and subsequent formation of stars within these regions.

A property of molecular clouds (and star clusters) is the mass function. In more detail, the mass distribution of molecular clouds is usually described in differential form by the cloud mass function (CMF), which is the number of clouds in a mass range divided by that range: $dN/dM = f(M)$. Molecular clouds typically have power law CMF of slope α, i.e. $dN/dM \propto M^{\alpha}$. The mass spectrum in molecular clouds varies between power law indexes of $\alpha = -1.5$ and $\alpha = -2.1$ (Rosolowsky, 2005) with typical values of $\alpha \sim -1.8$ (Heyer et al., 2001), which are similar to the values reported for stellar clusters (Zhang & Fall, 1999; Hunter et al., 2003; Fall & Chandar, 2012).

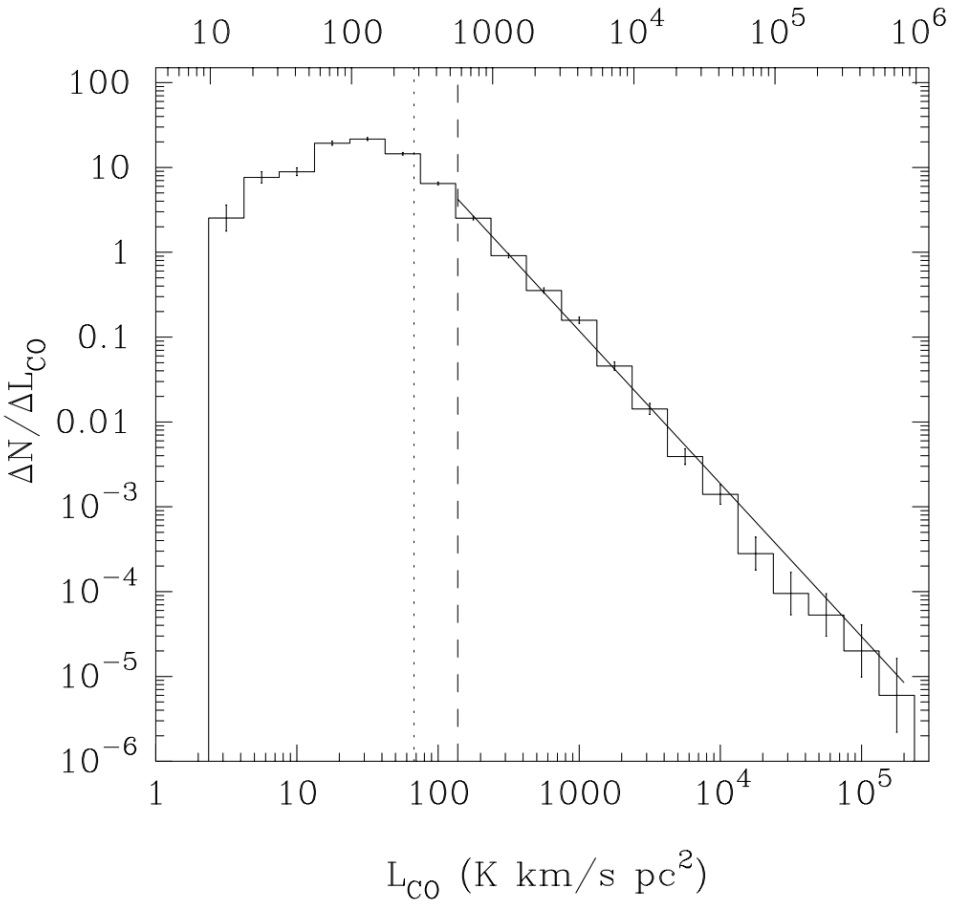

Figure 1.3: CO luminosity function $\Delta N/\Delta L_{\rm CO}$ of the molecular clouds observed by Heyer et al. (2001) in the outer Galaxy (FCRAO Outer Galaxy Survey). The top coordinates on the x-axis correspond to the mass scales assuming a constant CO-to-H_2 conversion factor. The power law distribution $\Delta N/\Delta L_{\rm CO} \propto L_{\rm CO}^{\alpha}$ has a slope of $\alpha = -1.8(\pm 0.03)$.

Observationally, it was established in the 1980's that molecular clouds follow a set of three scaling relations between their kinematic and structural properties, which are coupled such that a third relation follows if the other two are valid (Larson, 1981). The first relation is a power law dependence of the cold cloud one-dimensional velocity dispersion along the line of sight $\sigma_{\rm v}$ (from CO line-width observations) with cloud size $R_{\rm cc}$ of the form: $\sigma_v\ [{\rm km\,s^{-1}}] \propto R_{\rm cc}^{0.38}$. Later on, Solomon et al. (1987) and Heyer & Dame (2015) report slope values of ~ 0.5, for example in Heyer et al. (2001) observations, for clouds with sizes larger than ~ 3 pc. The observations typically cover a bit more than two orders of magnitude in could size and slightly more than one order of magnitude in velocity dispersion. The second relation is between velocity dispersion and cloud mass $M_{\rm cc}$. This relation connects the virial mass estimate of the clouds $M_{\rm vir}$ (from the velocity dispersion) to the measured mass of the cloud $M_{\rm cc}$. The relation has the form $\sigma_{\rm v} \propto M_{\rm cc}^{0.2}$.

The third Larson relation shows the inverse correlation of average cloud density with cloud size in the form of $\rho_{cc} \propto R_{cc}^{-1.1}$. These three scaling relations have been confirmed by many observations (see e.g. Heyer & Dame, 2015, for a review).

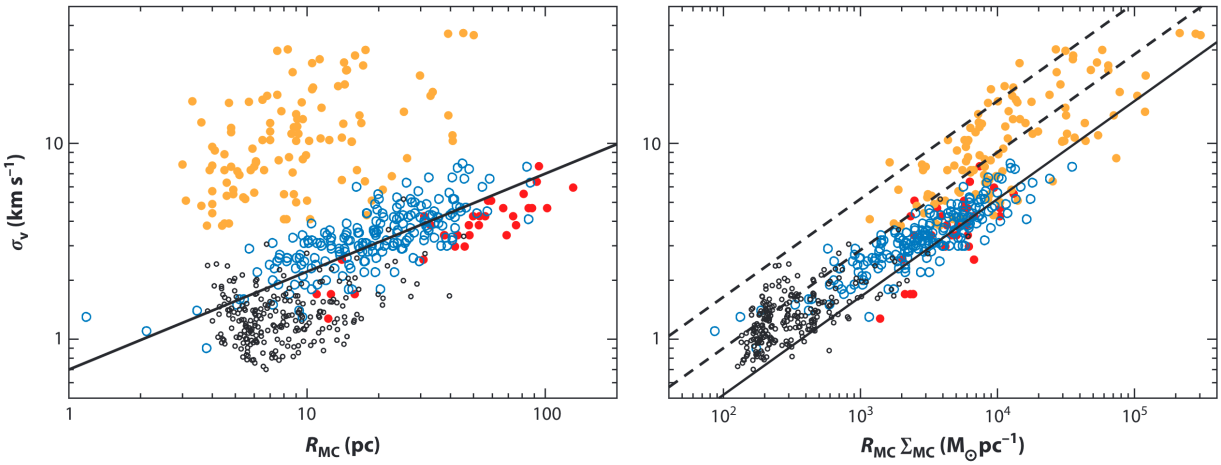

Figure 1.4: Reproduction of the fundamental "Larson relations" by Heyer & Dame (2015), from catalogues of molecular clouds at different regions of the Galaxy. In both panels, the data used are as follows: Dame et al. (1986) - red (molecular ring), Solomon et al. (1987) - blue (molecular ring), Oka et al. (2001) - orange (Galactic centre) and Heyer et al. (2001) - black (outer Galaxy). *Left panel*: Power law correlation of the ^{12}CO velocity dispersion σ_v with cloud size R_{MC}. *Right panel*: Variation of the velocity dispersion of observed Galactic molecular clouds with the product of size R_{MC} and mass surface density Σ_{MC}. The solid line corresponds to Eq. 4.2 for virial parameter $\alpha_{vir} = 1$. The dashed line is derived from Eq. 4.1 for $\alpha_{vir} = 3$ and the dotted line for $\alpha_{vir} = 10$. These equations are discussed extensively in section 4.3 of the present work.

The scaling relations for molecular clouds by Larson (1981) have been studied extensively in simulations that investigate the role of turbulence and external pressure in the fragmentation and sustainability of sefl-gravitating clouds (Bertoldi & McKee, 1992; Klessen, 2000; Ballesteros-Paredes et al., 2007; McKee & Ostriker, 2007; McKee et al., 2010; Ballesteros-Paredes et al., 2011; Field et al., 2011; Hennebelle & Falgarone, 2012; Hopkins et al., 2012; Ballesteros-Paredes et al., 2019). The time evolution of molecular clouds has been studied in isolated galaxies (e.g. Dobbs & Pringle, 2013; Benincasa et al., 2019; Fujimoto et al., 2019; Jeffreson et al., 2020, 2021). For example, Jeffreson et al. (2021) studied the time evolution of molecular clouds in simulated Milky Way-like galaxies and found self-gravitating clouds with lifetimes that scale with their sizes as $\tau_{life} \propto \ell^{-0.3}$. The lifecycle of molecular clouds is characterised by an accretion and a destruction phase (Elmegreen, 1983; Krumholz & McKee, 2005; Vázquez-Semadeni et al., 2010). During their accretion phase the clouds that accumulate enough mass for the gravitational instability to kick in will collapse marking the beginning of star formation. It is expected that

cold clouds are destroyed by the energetic feedback of the forming stars and therefore have a finite lifetime, typically in the range of 10-30 Myr (Chevance et al., 2020) and within ~ 5 Myr after the emergence of very massive stars through pre-supernova feedback (Chevance et al., 2022).

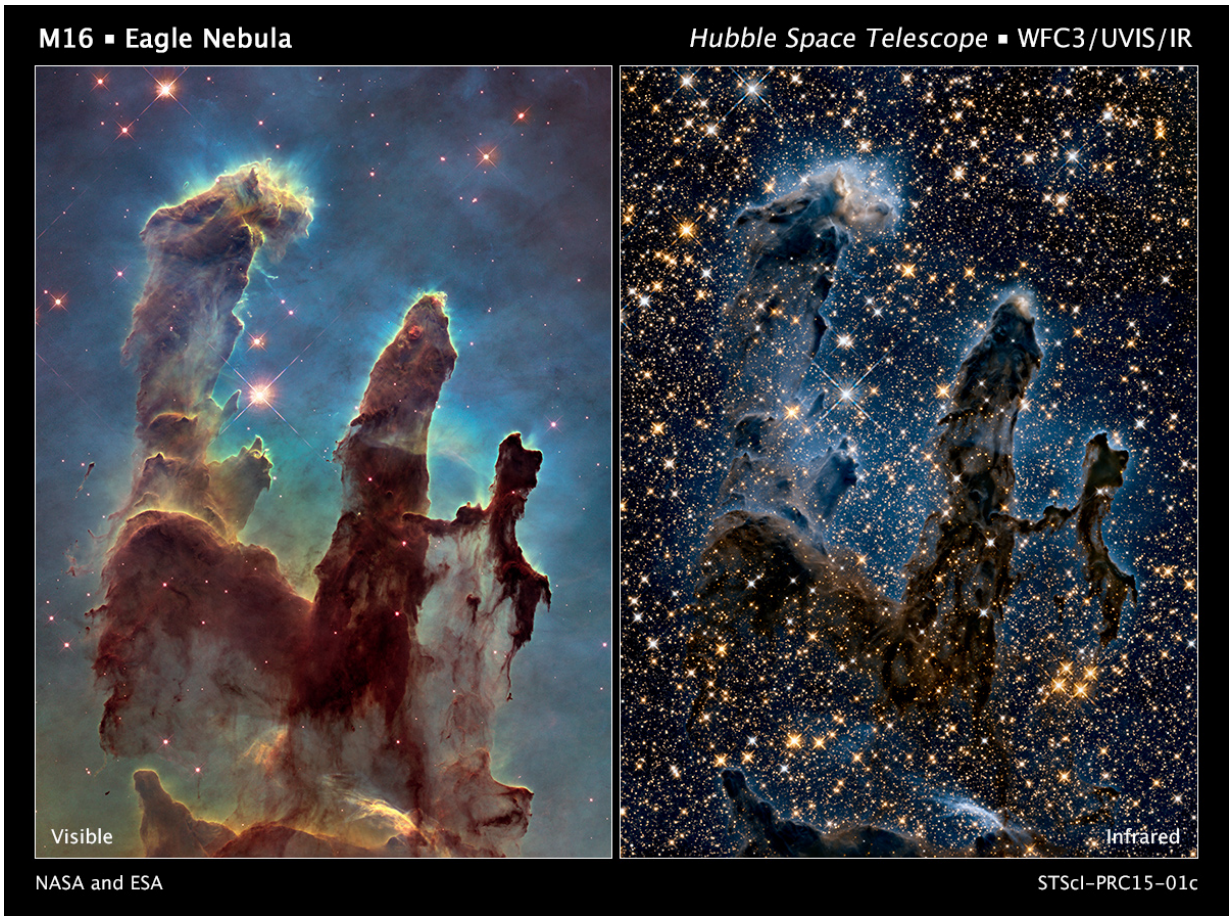

Figure 1.5: The molecular cloud "Pillars of Creation" located in the Eagle Nebula (M16) captured in optical (*left*) and near-infrared (*right*) by the Wide Field Camera 3 of the space telescope Hubble (HST). The image reveals three giant columns of cold gas where strong astrogenesis is observed.
Credits: NASA, ESA, and the Hubble Heritage Team (STScI/AURA)

1.1.5 Star formation and stellar feedback

As mentioned above, molecular clouds are the birthplaces of stars (Kennicutt & Evans, 2012). When enough gas is accumulated in a molecular cloud it can become gravitational unstable, i.e. the thermal, turbulent, and magnetic pressure of the cloud can no longer overcome the gravitational forces. Fragmentation of the collapsing cloud occurs since molecular clouds are not spherically symmetric. Those fragmented regions will further collapse under the influence of self-gravity and become the cores of star cluster formation.
Once the stars are born they start shaping their surroundings via stellar feedback. There are two main forms of stellar feedback: early type and late type. Early type feedback includes the effects of stellar radiation as well as stellar winds. The far ultra-violet (FUV) portion of the stellar radiation (photon energies of 6-13.6 eV) will heat up the gas via photoelectric heating and exerts radiation pressure on dust, especially in higher density environments (Tan et al., 2014). This radiation pressure and FUV heating can already be important factors in limiting further accretion onto the star(-cluster) and self-regulate star formation. Massive stars ($> 8\,M_\odot$) also have a significant portion of their radiation in the hydrogen ionising regime (EUV, photon energies above 13.6 eV). Through this radiation, the parental molecular clouds will be ionised and dispersed and an H II region forms (Spitzer, 1978). Additionally to early radiation feedback, massive stars also exhibit strong stellar winds (Weaver et al., 1977; MacKey et al., 2015). Those winds can have terminal wind velocities in excess of $1000\,\mathrm{km\,s^{-1}}$ (Puls et al., 2008) and are responsible for creating hot wind bubbles which further limit gas accretion and subsequent star formation. However, the most violent stellar feedback process is the explosion of supernovae (SNe) at the end of the lifetime of the massive stars. Core-collapse SN (also known as Type II SNe) occur when stars run out of fusion fuel and cannot support themselves anymore with radiation pressure against gravitational collapse. A cataclysmic chain of processes happens, in which the star first implodes and then explodes due to the generation of neutrinos in the strongly heated core. This explosion releases about 10^{51} erg into the medium which drives strong shocks and heats up the gas to temperatures higher than 10^5 K (Mac Low & McCray, 1988). Super-bubbles can be formed when multiple SN events overlap temporarily and spatially. Out of those super-bubbles a strong outflow can be launched which transports gas out of the mid-plane ISM (Kim & Ostriker, 2015). Additionally to being responsible for creating the hot gas phase, SN remnants are also the space where cosmic rays (CR) - mainly relativistic protons with energies of about ~ 1 GeV - are accelerated via diffusive shock acceleration (Bell, 1978; Dorfi & Breitschwerdt, 2012; Simpson et al., 2016). Those CR are accelerated with an efficiency of $\sim 10\%$ (Ackermann et al., 2013) and have an energy density of $\sim 1.4\,\mathrm{eV\,cm^{-3}}$, comparable to the thermal, magnetic and turbulent energy density of the ISM (Draine, 2011), and are therefore dynamically import. Recent numerical experiments have shown that CR diffusion can strongly promote galactic outflows (Simpson et al., 2016; Girichidis et al., 2018; Rathjen et al., 2021).

1.1.6 Galactic feedback

The gas is the active chemical ingredient of galaxies: not only the stars are born out of the cold dense gas, as we discussed in section 1.1.4, but their deaths impact the gas chemically and dynamically. In a galaxy, outflows can occur due to accreting black holes or stars.
The active galactic nuclei (AGN) of massive galaxies can drive strong winds through radiation pressure, accretion onto the central black hole (accretion-disk winds) and radio jets (Dasyra et al., 2015, 2016; Fotopoulou et al., 2019). More than one of these driving mechanisms can contribute to the creation of a galactic wind. The events that initiate such strong outflows can release more energy than the binding energy of a galaxy (Fabian, 2012) and can lead to acceleration (and possible eventual ejection) or heating of the gas on large scales (e.g. kpc^2, Lípari et al., 2004; Rupke & Veilleux, 2011). It is evident that such strong outflows impact the ISM, often severely, since they can be massive with gas mass flow rates exceeding star formation rates (SFRs) in galaxies even of order 100 $\mathrm{M}_\odot \mathrm{yr}^{-1}$ (see e.g. Cicone et al., 2014) and they deplete the cold molecular gas reservoir from which stars form.

1.2 Dwarf galaxies

The formation of dense and cold gas structures and the formation of star clusters therein can be triggered and enhanced in extreme environments (Elmegreen & Efremov, 1997) like starburst galaxies (Holtzman et al., 1992; Leroy et al., 2018), interacting galaxies (Whitmore et al., 2010; Herrera et al., 2012; Johnson et al., 2015) and dwarf galaxies (Johnson et al., 2000; Kepley et al., 2016; Ochsendorf et al., 2017). Dwarf galaxy mergers are typical systems to study those events. Dwarf galaxies are metal-poor systems resembling the chemical conditions in the early Universe with stellar masses less than $\sim 3 \times 10^9\,\mathrm{M}_\odot$(White & Frenk, 1991; Navarro et al., 1995; Moore et al., 1999; Robertson et al., 2005; Rodriguez-Gomez et al., 2016). They outnumber other types of galaxies, even though they do not contribute significantly to the overall mass budget of galaxies in the local universe (see e.g. reviews Mateo, 1998; Naab & Ostriker, 2017). Typical dwarf galaxy systems in the local solar neighbourhood are the Large- and Small Magellanic Clouds (see Fig. 1.6).

Generally, dwarf galaxies are metal-poor systems and exhibit less complex chemical evolution compared to larger spiral or elliptical galaxies (Tolstoy et al., 2009; McConnachie, 2012). This fact in combination with their compact sizes and their high star formation efficiencies, especially in interacting merging systems (Kepley et al., 2016), make dwarf galaxies excellent environments to study the formation and evolution of cold dense clouds and stars computationally, since low masses allow high resolution numerical studies (Saitoh et al., 2010; Hopkins, 2013; Hu et al., 2016, 2017; Lahén et al., 2019, 2020; Steinwandel et al., 2020; Hislop et al., 2022).

Figure 1.6: The Large and the Small Mangellanic clouds (LMC and SMC, respectively), as examples of observations of dwarf galaxies. The Mangellanic clouds are two irregular dwarf galaxies of the Local Group and satellite companions of our Galaxy. They are visible to the naked eye from the southern hemisphere.
The Mangellanic clouds as seen above the Auxiliary Telescopes of the European Southern Observatory's (ESO) Very Large Telescope (VLT) in Paranal, Chile.
Credits: J. C. Muñoz/ESO

In the hierarchical picture of galaxy formation within a ΛCDM Universe, dwarf galaxies are the smallest structural unit (Cole et al., 2000). However, discrepancies between theoretical predictions and observational evidence exists in e.g. the "missing satellites problem", which states that more massive satellite galaxies should exist than the observed number of Milky Way satellites (Moore et al., 1999). Already in 1974, Larson (1974) proposed that galactic outflows can have a strong impact on dwarf galaxies and be the reason for their low metallicity. Newly enriched gas by massive star feedback gets expelled out of the dwarf galaxies due to strong coupling of stellar feedback to the gas dynamics in those systems. Generally, SN are thought of to be the efficient driving mechanism of outflows in dwarf galaxies. Nonetheless, recent observations indicate that also AGN can be present in dwarfs and play an important role in the driving of large-scale outflows (Koudmani et al., 2022).

In the present work, we simulate a dwarf galaxy starburst. Simply put, starbursts are galaxies that have bursts of very high star formation rates (SFRs), from hundreds to thousands times higher than the SFR of "normal" galaxies (for instance, a "normal" galaxy like our Milky Way has a star formation rate of about 3 $M_\odot\, yr^{-1}$) (see e.g. Holtzman et al., 1992; Gallagher, 1993; Heckman, 1997; Kennicutt et al., 2005; Leroy et al., 2018). Starbursts have been observed in many types of galaxies, from large spiral galaxies to dwarf and interacting galaxies. The duration of starbursts in dwarf galaxies is measured to be higher than 100 Myr (Thornley et al., 2000; Tremonti et al., 2001; McQuinn et al., 2010, 2015). Most starburst galaxies happen due to mergers or by having near encounters with neighbouring galaxies. Among the most-studied starbursts are the M82, the Arp220 and the Antennae galaxies (NGC 4038/NGC 4039) (see Fig. 1.7).

1.3 Numerical studies of the ISM

Numerical experiments of the evolution and governing processes in the ISM are needed since observations can be ambiguous and direct tests of theoretical predictions are not always feasible. The dynamical scale, however, behind those processes is so vast that a single-model-approach cannot be sufficient to resolve them all. Gas chemistry and dissipation of turbulence happens on the molecular scale. Star formation emerging out of pre-stellar cores happens on AU (astronomical unit AU $\approx 4.8 \times 10^{-6}$ pc) scales. The molecular clouds out of which the pre-stellar cores are formed can be up to hundreds of parsecs in size. Those clouds sit in an ISM which is part of galaxies which stretch over kiloparsecs. The temperature range extends from molecule formation down to tenths of Kelvin up to shock heated gas in supernova remnants with temperatures in excess of 10^7 K. Observed velocity dispersion in the solar neighbourhood is around 10 km s^{-1} while stellar wind of massive OB stars can exceed 1000 km s^{-1}. Due to this enormous range in parameters, numerical experiments have to focus on a subset of scales and build up on missing

Figure 1.7: Image of the Antennae galaxies (NGC 4038/NGC 4039) by the Hubble Space Telescope, as an example of a starburst galaxy.
Credits: ESA/Hubble & NASA

resolution of sub-grid models and approximations for the larger scale influences.

Full cosmological simulations like IllustrisTNG (Springel et al., 2017) try to model the whole universe and the formation and evolution of galaxies by focusing on the gravitational interaction of baryonic gas and dark matter. Smaller cosmological volume simulations try to incorporate more baryonic physics but still heavily rely on sub-grid models for the realisation of feedback processes (see e.g. Hopkins et al., 2018). Recent numerical improvements and developments enable the simulation of isolated disk galaxies (see e.g. Bieri et al., 2022) or less massive dwarf galaxy systems (see e.g. Lahén et al., 2019) with the inclusion of chemistry and self-consistent star formation, including early and late stellar feedback. High-resolution stratified disk simulations of a galactic patch with sizes of 500-1000 pc can incorporate chemistry and all major stellar feedback processes including on-the-fly radiative transfer but still need to employ sub-grid models for star and star cluster formation (see e.g. Kim & Ostriker, 2017; Rathjen et al., 2021). Zoom-in simulations of those multi-phase ISM simulations can reach spatial resolutions of down to 0.1 pc and are able to converge on the chemical evolution and star formation within single molecular clouds (see e.g. Seifried et al., 2017). By resolving the important processes on each individual scale and then informing the sub-grid model of the next higher scale simulations it might become feasible to archive a full picture of the evolution and governing processes of the ISM.

1.4 Aim of this work

In this work, we investigate the impact of an extended starburst in the formation, the evolution and the properties of simulated cold clouds. For this purpose we analyse the multi-phase ISM and especially the star-forming cold dense gas clouds emerging after a massive starburst caused by the merger of two gas-rich and metal-poor dwarf galaxies in the smoothed particle hydrodynamics (SPH) simulation carried out by Lahén et al. (2019). The simulation is part of the GRIFFIN project[2] (Galaxy Realizations Including Feedback From INdividual massive stars) which aims to resolve current challenges of galaxy formation (see e.g. review Naab & Ostriker, 2017) implementing a detailed model for the ISM. We focus especially on the emerging cloud mass function (CMF) of the detected cold clouds and compare the clouds to observationally informed scaling relations. We trace the life cycle of the cold star-forming clouds and we study their evolution into star clusters. With this thesis we aspire to create a thorough understanding of the processes governing the formation and evolution of cold star-forming clouds and to evaluate how well our modelling tools capture the environment for star formation in merging galaxies from an observational perspective.

[2] https://wwwmpa.mpa-garching.mpg.de/~naab/griffin-project/

1.5 Structure of this work

This work is structured as follows: chapter 1 is the introduction, where we establish the basic theoretical background and build the foundation of our study. In chapter 2, we present the methods and the tools we used throughout our analysis and introduce the underlying simulation for our study. In chapter 3, we present the results of our study of the multi-phase interstellar medium (ISM) and the gas outflows detected in our simulation. In chapter 4, we present our analysis of the cold phase of the ISM and the detection and tracing of cold clouds. In chapter 5, we present the findings of our study on the transition of the cold clouds into star clusters. In chapter 6, we summarise our findings and detail our conclusions.

Chapter 2

Simulation and methods

The underlying dwarf merger simulation was performed by Lahén et al. (2019) as part of the GRIFFIN project, utilising the SPHGAL implementation (Hu et al., 2014, 2016, 2017) of the SPH hydrodynamics code GADGET-3 (Springel, 2005). SPHGAL accounts for artificial viscosity and thermal conduction as described in (Hu et al., 2014).
Before describing and discussing the simulation used in the present work, it is useful to lay out the basics of Hydrodynamics and the numerical implementation of the equations of motion.

2.1 Basics of Hydrodynamics

2.1.1 The Euler equations

As a sub-discipline of Fluid Mechanics, Hydrodynamics studies the motion of liquids. In Classic Hydrodynamics there are two numerical approaches in the study of fluids in motion that are mathematically equal: the "Eulerian" and the "Lagrangian" approach.

Eulerian approach: In this approach, the "observer" is still and describes the variations in the motion of the fluid focusing on the space through which the liquid flows as a function of time. In the Euler formulation the reference frame is fixed in space.

Lagrangian approach: In this approach, the "observer" follows all units of the fluid and describes the variations in the motion along the fluid trajectory. In the Lagrange formulation we have a co-moving reference frame.

Despite the difference in the approach the two methods produce identical results and both use the Lagrange derivative[1] to describe the changes in the motion:

$$\frac{d}{dt} = \frac{\partial}{\partial t} + \mathbf{v} \cdot \nabla \tag{2.1}$$

The motion of a fluid can be described through the following equations:

The Euler equations

The Euler equations are a set of equations that represent the conservation of mass, momentum, and energy during the motion of a fluid. These equations of motion and continuity address an ideal fluid with inviscid flow, i.e. a fluid with no viscosity and no thermal conductivity.

- **Conservation of mass**

The "continuity equation" expresses the law of conservation of mass during the motion of a fluid. Using the Lagrange derivative 2.1, the continuity equation is given in differential form (in the Lagrangian formulation) as:

$$\frac{d\rho}{dt} + \rho(\nabla \cdot \mathbf{v}) = 0 \tag{2.2}$$

where ρ is the density and $\mathbf{v}$ the velocity of the fluid.

- **Conservation of momentum**

The conservation of momentum equation as an equation of motion is derived by the second Newton law and is given in differential form as:

$$\frac{\partial \mathbf{v}}{\partial t} + (\mathbf{v} \cdot \nabla)\mathbf{v} = -\frac{\nabla P}{\rho} + \frac{\mathcal{F}}{\rho} \tag{2.3}$$

where P is the pressure exerted on a small volume of the fluid, therefore $-\nabla P$ is the total force per unit volume exerted on the fluid and $\mathcal{F}$ is any external conservative force (e.g. gravity) acting on the fluid per unit volume (i.e. force density). Therefore the term $\frac{\mathcal{F}}{\rho}$ is equal to: $\frac{\mathcal{F}}{\rho} = -\nabla\Phi$, where Φ is the potential of the conservative force (e.g. Φ is the gravitational potential).

In the case of an incompressible fluid, the density is a constant therefore the equations 2.2 and 2.3 are a system the solution of which gives the values of the three-dimensional velocity $\mathbf{v}$ and the pressure P for the fluid at every point in space and time[2]. Nevertheless, if the fluid is compressible

[1] Throughout this work we use the convention that boldface mathematical symbols stand for vectors.

[2] Given initial and boundary conditions for the system

we need one more equation so that the system has a solution for the now five unknown quantities[3]. Ignoring phenomena of viscosity and thermal conductivity, the variations in the motion of the fluid are adiabatic therefore we can use the first law of Thermodynamics to derive the equation of energy.

• **Conservation of energy**

The conservation of energy as an equation of motion expresses the first law of Thermodynamics and is given in differential form as:

$$\rho \frac{du}{dt} = -P(\nabla \cdot \mathbf{v}) \tag{2.4}$$

where u is the specific internal energy of the system (i.e. the internal energy per unit mass).

2.1.2 The Navier-Stokes equations

The equivalent equations of motion to the Euler equations for ideal fluids are the Navier-Stokes equations, if we including viscosity in our study. The Navier-Stokes equations describe turbulent flows. Before presenting the Navier-Stokes equations, it is useful to define two quantities that describe the factor of viscosity in the flow, which differentiates the formulation from the Euler equations: the dynamic viscosity of the fluid η and the kinematic viscosity of the fluid ν, defined as the ratio of the dynamic viscosity η over the density of the fluid ρ, i.e. $\nu = \eta/\rho$. The Navier-Stokes equations in differential form are expressed as:

$$\rho \left[\frac{\partial \mathbf{v}}{\partial t} + (\mathbf{v} \cdot \nabla)\mathbf{v} \right] = \mathcal{F} - \nabla P + \eta \nabla^2 \mathbf{v} + \frac{\eta + 3\eta_{\perp}}{3} \nabla(\nabla \cdot \mathbf{v}) \tag{2.5}$$

For an incompressible fluid[4], equation 2.5 is simplified in the form:

$$\frac{\partial \mathbf{v}}{\partial t} + (\mathbf{v} \cdot \nabla)\mathbf{v} = \frac{\mathcal{F}}{\rho} - \frac{\nabla P}{\rho} + \nu \nabla^2 \mathbf{v} \tag{2.6}$$

[3]Five unknown quantities: three components of the velocity $\mathbf{v}$, pressure P and density ρ

[4]We remind that for an incompressible fluid we have -by definition- that: $\frac{d\rho}{dt} = 0$, therefore from the continuity equation 2.2 we have that $\nabla \cdot \mathbf{v} = 0$.

2.2 Numerical realisation of Hydrodynamics

2.2.1 The two approaches

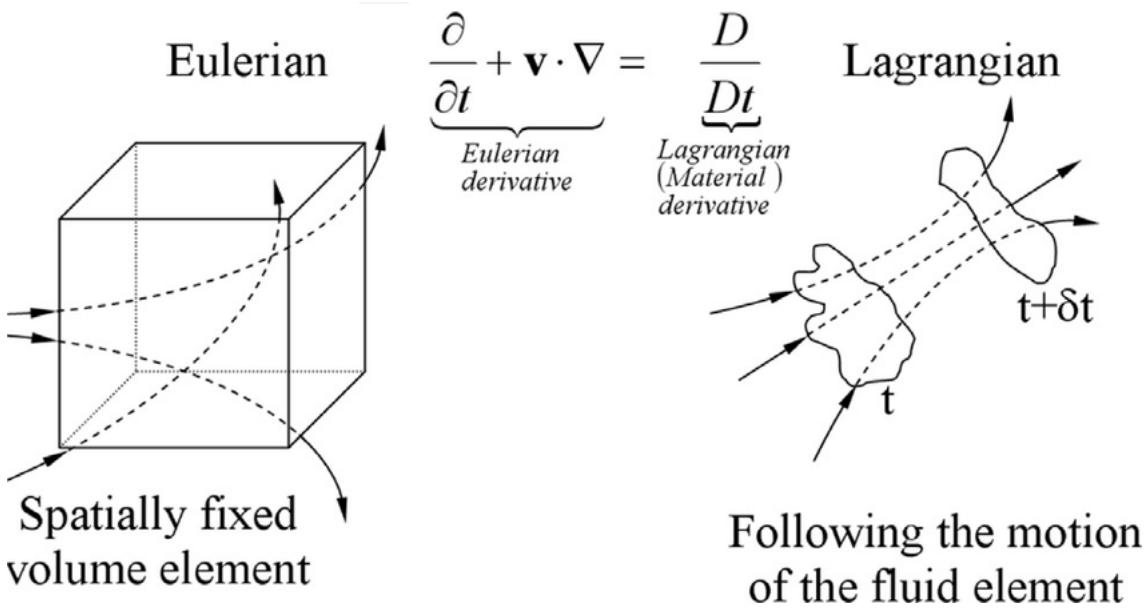

Figure 2.1: Differences between the Eulerian formalism with a fixed reference frame and the Lagrangian formalism with a co-moving reference frame, from Sampath et al. (2016).

The same two schools of thought that we discussed in the previous section are used when we approach solving the equations of hydrodynamics computationally. First, there is the Eulerian approach, in which space is discretised into a grid with a fixed reference frame. Hydrodynamical fluxes in this formulation are treated as Riemann jump problems in which the discontinuities are the grid boundaries. An example of a simulation code using the Eulerian formalism is FLASH[5]. In the Lagrangian approach, there is no fixed frame of reference, but a reference frame which is co-moving with the fluid elements. Interactions between fluid elements in this formalism are treated as $N-$body problems. An example of a simulation code using the Lagrangian approach is GADGET[6]. An illustration of the differences between the two formalisms can be seen in Fig. 2.1 (Sampath et al., 2016). In the present work, we use a simulation of a dwarf galaxy merger (Lahén et al., 2019) using the GADGET-3 code (Springel, 2005), which is a Lagrangian code. Therefore, we will focus more on this type of codes.

[5]More information on the FLASH code can be found here: https://flash.rochester.edu/site/flashcode/

[6]More information about the GADGET code can be found here: https://wwwmpa.mpa-garching.mpg.de/gadget4/

2.2.2 *N*-body problems

As we mentioned earlier, the Lagrangian formalism treats the interactions between fluid elements as N-body problems. The direct summation approach is the easiest way to determine the orbits of particles for a gravitational N-body system. By adding together the individual point masses of the particles, this approach calculates the Newtonian gravitational potential $\Phi_g(r)$ of a system of N point masses. Therefore, with this approach one can directly acquire the acceleration of each particle and then integrate it to obtain the velocities and the positions. The gravitational potential is calculated by the classic Newtonian formula as (see Dolag et al., 2008; Springel, 2010):

$$\Phi_g(r) = -G \sum_i^N \frac{m_i}{\sqrt{(r_j - r_i)^2 + \varepsilon^2}} \tag{2.7}$$

where ε is the "gravitational softening". The gravitational softening has a small finite value and it is entered in the numerical calculation of the gravitational potential, in order to prevent a zero denominator that could arise if two particles have the exact same point in space (i.e. $r_i = r_j$), thus resulting to an infinite gravitational potential at this point making the system numerically unstable.

2.2.3 Smoothed-particle Hydrodynamics (SPH)

The Smoothed-Particle Hydrodynamics (SPH) is a numerical method for solving the equations of hydrodynamics that describe the motion of a fluid, in the Lagrangian regime. With SPH we first calculate the density of a "kernel" (see Fig. 2.2).

Let us assume that we would like to calculate the mass density ρ at a distance $\mathbf{r}$ from a particle of interest. A straightforward approach would be to calculate the sum of the point masses in a sphere of radius r around the point of interest and then divide by the volume of this sphere: $V_{\text{sphere}} = \frac{4}{3}\pi r^3$, according to the equation:

$$\rho(\mathbf{r}) = \frac{3}{4\pi r^3} \sum_i m_i \tag{2.8}$$

This "Un-smoothed"-particle Hydrodynamics, if we may call it this way, works but neglects the fact that the particles located further away from the point of interest (i.e. have greater r values) contribute less to the density at the point of interest. Therefore, we would like to add a weight for the distance from the point of interest, thus "smoothing out" the density field. This happens through SPH, where we do not assume a sphere around the point of interest, but an SPH "kernel" as shown in Fig. 2.2.

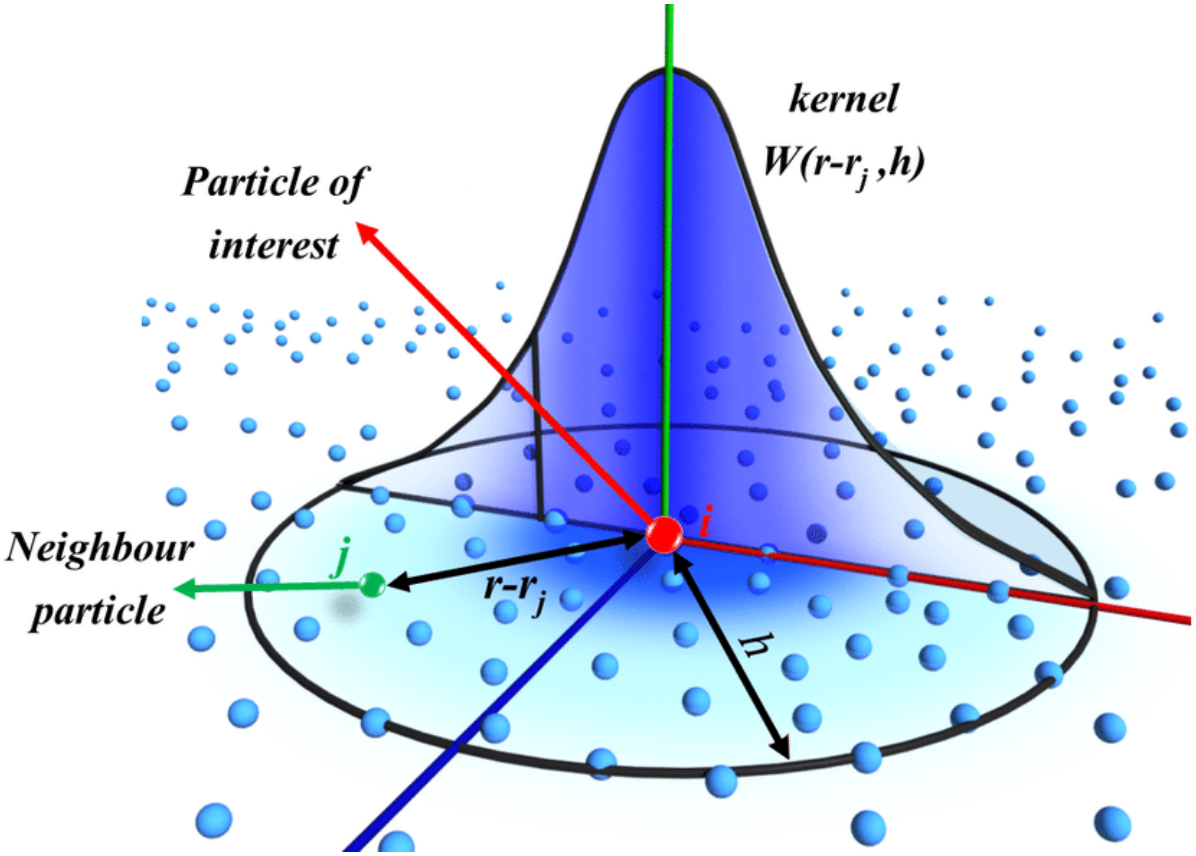

Figure 2.2: Visualisation of the SPH kernel, from Shadloo et al. (2016).

A kernel is a weighting function $W(\mathbf{r}-\mathbf{r_j}, h)$ that takes as arguments the distance of a neighbour-j from the particle of interest $\mathbf{r}-\mathbf{r_j}$ and a scaling factor h, which is called "smoothing length". The term "smoothing length" refers to the reduction in the kernel function W as the distance from the particle of interest at $\mathbf{r_j}$ increases. Therefore, the density ρ at a distance $\mathbf{r}$ from a particle of interest is calculated as (Price, 2012):

$$\rho(\mathbf{r}) = \sum_j m_j W(\mathbf{r}-\mathbf{r_j}, h) \tag{2.9}$$

where the kernel function W has to fulfil the following criterion:

$$\int_V W(\mathbf{r}-\mathbf{r_j}, h) dV' = 1 \tag{2.10}$$

After determining the density using a suitable kernel function, the next step is to define the SPH volume element. This can be done as:

$$V_j = \frac{\rho_j}{m_j} \tag{2.11}$$

However, Hopkins (2013) discuss that this definition introduces discontinuities and errors in the calculation of pressure and internal energy, therefore they propose this definition, instead:

$$V_j = \frac{X_j}{\sum_i X_i W(\mathbf{r_j} - \mathbf{r_i}, h_j)} \tag{2.12}$$

where X_j is a scalar, for example $X_j = m_j$.

After determining the density kernel and the volume element, SPH can derive all other quantities using the equations of motion of fluids (i.e. the Euler or the Navier-Stokes equations, depending on the problem). We remind also that due to the Lagrangian nature of the code, it is straightforward to derive the velocities of the SPH particles through integration of the accelerations and subsequently, derive the positions of the particles through integration of the velocities over time time.

2.3 The underlying dwarf merger simulation

In the following pages we describe the initial conditions and main physical processes of the underlying simulation by Lahén et al. (2020).

2.3.1 Initial conditions

The simulation encompasses two identical gas-rich low-metallicity isolated dwarf galaxies at sub-parsec resolution, based on the dwarf galaxy model by Hu et al. (2016, 2017). The mass resolution is $m_{\rm DM} = 7\times10^3\,{\rm M}_\odot$ for the dark matter particles and $m_{\rm baryonic} = 4\,{\rm M}_\odot$ for the baryonic matter, leading to a total of 10^7 gas, 5×10^6 dark matter, and 4×10^6 stellar particles per dwarf galaxy. The gravitational softening length is $\epsilon_{\rm DM} = 62\,{\rm pc}$ and $\epsilon_{\rm baryonic} = 0.1\,{\rm pc}$ for the dark matter and baryonic matter, respectively. Each dwarf galaxy has a virial radius of $r_{\rm vir} = 44\,{\rm kpc}$ and a virial mass of $M_{\rm vir} = 2\times10^{10}\,{\rm M}_\odot$. Each dark matter halo has a Hernquist density profile (Hernquist, 1990) whose equivalent NFW concentration parameter is $c = 10$ and NFW spin parameter is $\lambda = 0.03$. The identical dwarf galaxies also have a gas disk rationally supported by stars. The gas disk has a mass of $M_{\rm gas} = 4\times10^7{\rm M}_\odot$, a scale radius of $r_{\rm gas} = 1.46\,{\rm kpc}$ and initial metallicity of $Z_{\rm gas} \approx 0.1{\rm Z}_\odot$, which is a typical value for low-mass dwarf galaxies. The stellar disk has a mass of $M_* = 2\times10^7\,{\rm M}_\odot$, a scale radius of $r_* = 0.73\,{\rm kpc}$ and a scale height of $h_* = 0.35\,{\rm kpc}$. The dwarf galaxies are initialised with a parabolic orbit with a pericentric distance of $d_{\rm peri} = 1.46\,{\rm kpc}$ and separation of $d_{\rm init} = 5\,{\rm kpc}$.

2.3.2 Star formation and stellar feedback

We model star formation by spawning star particles if the gas is in a converging flow and the Jeans mass associated with every gas particle, $M_{\rm j,i} = \frac{\pi^{5/2} c_{\rm s}^3}{6 G^{3/2} \rho_{\rm i}^{1/2}}$, with the local sound speed $c_{\rm s}$, the gravitational constant G, and the local gas density $\rho_{\rm i}$, exceeds a threshold density of 8 SPH kernel masses ($\sim 8 \times 400\,{\rm M}_\odot = 3200\,{\rm M}_\odot$) with a star formation efficiency per free-fall time of $\epsilon_{\rm sf} = 2\,$per cent. Furthermore, we enforce instantaneous star formation for particles with a resolved Jeans mass lesser than half a kernel mass ($\sim 200\,{\rm M}_\odot$). The instantaneous star formation threshold corresponds to a hydrogen number density of $n_{\rm H} > 10^{3.5}\,{\rm cm}^{-3}$ at temperatures between $T = 10 - 100\,{\rm K}$. Once a star particle is formed we sample massive stars in a mass range of 0.08 $\rm M_\odot$ to 50 $\rm M_\odot$ from a Kroupa IMF (Kroupa, 2001) in order to track the stellar feedback component of individual massive stars. Each individually sampled massive star above $M > 1\,{\rm M}_\odot$ contributes to the ISRF. Non-ionising far ultraviolet (FUV) emission of the stars is integrated from the BaSeL library (Westera et al., 2002) and propagated into the medium considering dust shielding calculated with TreeCol (Clark et al., 2012). Additionally, young massive stars ($> 8\,{\rm M}_\odot$) also contribute with hydrogen ionising radiation which we realise with HII regions modelled as Strömgren spheres. The environmental densities at SN explosion sites will be pre-processed by the ionising radiation which enables a stronger coupling of the injected SN energy to the gas dynamics (see e.g. Rathjen et al., 2021; Smith et al., 2021). We realise Type II SNe by injected thermal energy equivalent to $E_{\rm SN} = 10^{51}\,{\rm erg}$ into the surrounding SPH kernel alongside with ejecta mass and metallicity obtained from Chieffi & Limongi (2004) at an ejection velocity of $v_{\rm ej} = 3000\,{\rm km\,s}^{-1}$. Lastly, we account for stellar winds from asymtotic gian branch (AGB) stars with metal yields from Karakas (2010).

2.3.3 Chemistry

The code allows the treatment of non-equilibrium chemistry with heating and cooling while explicitly following the species H, $\rm H^+$, $\rm H_2$, C, $\rm C^+$, O, CO and $\rm e^-$, based on the chemical network by Nelson & Langer (1997) and adapted by Glover & Mac Low (2007). We account for photoelectric heating on dust grains, cosmic ray ionisation and photo-dissociation of $\rm H_2$, as well as fine-structure and metal cooling. However, in the high-temperature regime ($T > 3 \times 10^4\,{\rm K}$), we switch to metallicity dependent cooling tables by Wiersma et al. (2009) under the assumption of an optically thin ISM subjected to an ionising UV field from the galactic background (Haardt & Madau, 1996).

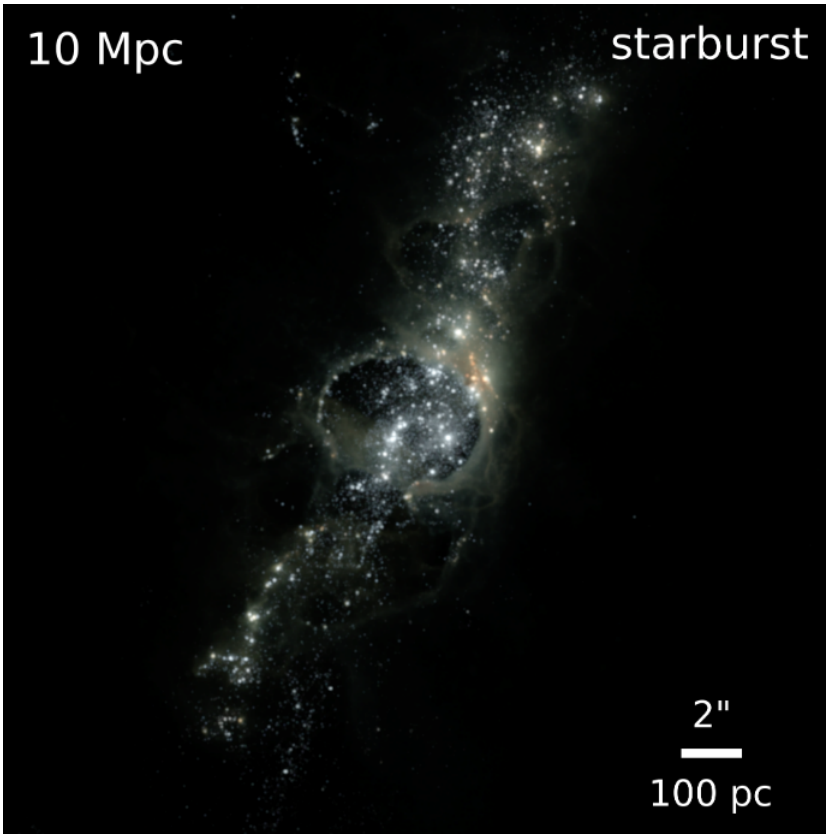

Figure 2.3: Mock observations of the dwarf galaxy merger at the time of the starburst (~170 My) from Lahén et al. (2022) (Fig. 1 in Lahén et al. (2022)). The images are colour composites of B (blue), V (green) and I (red) bands at Hubble Space Telescope resolution assuming the system is at a 10 Mpc distance, produced using dusty radiative transfer with SKIRT 9 (Camps et al., 2021).

2.3.4 Evolution of the system

An overview of the evolution of the system is shown in Fig. 2.4 from Lahén et al. (2020) (Fig. 2 in Lahén et al. (2020)). Each row depicts the system at a different characteristic phase of the simulation, which has run row for 457 Myr, on the x-y plane. From top to bottom we have: the first approach of the two identical dwarf galaxies at 5 Myr, the first pericentric passage at 50 Myr, the first apocentre at 80 Myr, the second encounter of the galaxies and the onset of the major starburst at around 160 Myr and the interaction right after the starburst at 180 Myr. Each column shows a different property of the system. From left to right we have: the surface density of the stars forming the simulation Σ_*, the surface density of the gas $\Sigma_{\rm gas}$, the gas density weighted temperature $T_{\rm gas}$ and the density weighted thermal gas pressure $P_{\rm gas}/k_{\rm B}$.
During the first approach of the dwarf galaxies, their interaction manifests itself initially at the edges of the extended gas disks of the galaxies, where outflows begin due to the tidal forces between the two systems and gas compression takes place. As the galaxies begin moving away from each

other and reaching their first apocentre, there is a rise in the star formation. When compared to interactions between more massive late-type galaxies (see e.g. Smith et al., 2007; Ellison et al., 2013), which exhibit more centrally focused star formation, the distribution of star formation is substantially more stretched because the interaction-induced gas compression is already intense further away from the galactic centres. The second approach, the tidal forces between the merging dwarf galaxies drive extended outflows in the system. During the starburst phase the interstellar medium of the merger begins having a more clumpy and filamentary structure, especially in the central 2 kpc, where star formation also peaks. When the star formation rate (SFR) reaches its maximum, the gas disks are moving towards the centre of the system, where the largest star clusters are formed. After some time from the starburst, the supernova (SN) feedback from dying stars in the star clusters that have formed, accelerates, heats up and dissipates the gas, even at the densest areas of molecular clouds, thus driving further outflows in the system and exhausting the gas reservoir from which stars form. As a consequence, the starburst is weakened and the phenomenon is halted.

2.3.5 Analysis tools

We identify and trace clouds in our simulation with the help of the analysis toolkit *pygad* (Röttgers et al., 2020) implemented in GADGET. To identify the cold clouds in each snapshot we use the friends-of-friends algorithm (FoF) implemented in *pygad*. Throughout our analysis we use a linking length of 1 pc and we only consider gas above a certain number density threshold, ρ, and below a certain temperature, T. Since our simulated system is poor in H_2 we do not form actual molecular clouds. Therefore, to compensate for the lack of molecular gas and to approach realistically the properties of molecular clouds we focus our study exclusively on sufficiently dense and cold gas. Our fiducial values are $\rho_{\rm gas} > 100\,{\rm cm}^{-3}$ and $T_{\rm gas} < 300\,{\rm K}$, based on the different ISM phases characterised by density/temperature cut-offs (e.g. Walch et al., 2015; Rathjen et al., 2021). Furthermore, we discard all potential cloud identifications which consist of less than a cut-off value of 100 SPH particles.

After using the FoF algorithm for the identification of the cold clouds in chapter 4, we track the life cycle of individual clouds via backward-tracing. For this purpose, we use a tracing routine where a group of unique particles (i.e. a cloud) in any given simulation snapshot is considered to be the same cloud at a previous stage, if at least 20% of the unique particles of the potential parental cloud in the previous snapshot are found in the current cloud. We tested a wide range of thresholds and found that 20% gives the most stable results.

For the analysis and the tracing of cold gas clouds that include star clusters in chapter 5, we use the aforementioned FoF algorithm, but this time we look for groups that consist of cold gas and stars. To do so, we use again a linking length of 1 pc and fiducial values $\rho_{\rm gas} > 100\,{\rm cm}^{-3}$ and $T_{\rm gas} < 300\,{\rm K}$ for the gas component. Furthermore, this time we include also star particles in the algorithm, to look for composite clumps. As before, we discard all potential cloud identifications

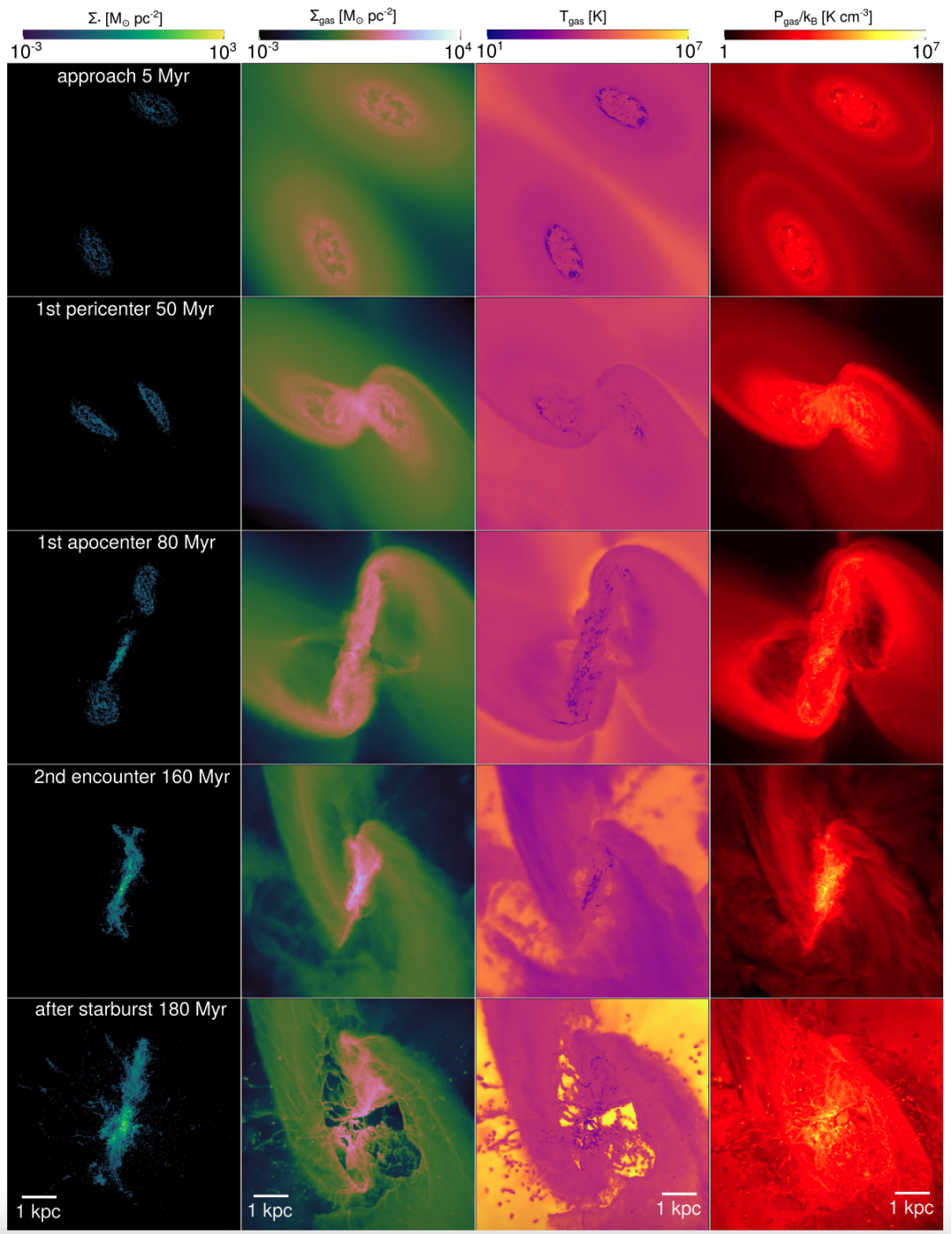

Figure 2.4: Overview of the dwarf galaxy merger from Lahén et al. (2020). The panels of each row are projections on the x-y plane at different stages of the simulation. *From top to bottom*: first approach of the dwarf galaxies, first apocentre, onset of the starburst and the interaction after the starburst. The panels of each column show different physical properties. *From left to right*: surface density of stars formed during the simulation, surface density of gas, density weighted gas temperature and density weighted thermal gas pressure. Each panel has a volume of $(7\ \mathrm{kpc})^3$.

which consist of less than a cut-off value of 100 SPH gas particles. For tracing the new objects, i.e. the clumps consisting of cold gas and stars, we use a new tracing algorithm. The new tracer implements both backward- and forward-tracing, which removed the need of specifying an arbitrary percentage threshold of unique particles from the parental cloud to be part of the cloud we analyse. Schematically, the tracing routine works as follows: for a simulation snapshot N, the tracer loads the FoF output of the previous snapshot N-1 and the next snapshot N+1. Then, it checks in both the previous and the next snapshots if there is a blob/clump with the IDs of one of the blobs in the current snapshot N (for the sake of simplicity, we are describing the process for only one blob; in reality these checks happen for multiple groups at the same time). If there is a blob with the desired IDs, then the tracer links the blob in the current snapshot N with its progenitor(s) and descendant(s) in the snapshots N-1 and N+1, respectively. In this way, we can construct full "trees" with the histories of the identified star-forming cold clouds in our simulation.

Chapter 3

The extended starbursts of dwarf galaxy mergers

In this chapter, we present the results of our analysis of the multi-phase interstellar medium (ISM) in our simulation. We discover an extended starburst both in space and time and we study the mass outflow rates $\dot{M}_{\rm out}$ and the star formation rate $\dot{M}_*$ of the system. Our study reveals the effects of the outflows in the different phases of the ISM and the impact of the starburst in the morphology and the evolution of the system.
The results of this chapter are ready to be submitted to the "*Monthly Notices of the Royal Astronomical Society" (MNRAS)* for publication.

3.1 Overview of the system

An overview of the gas distribution (top panels) and the density weighted temperature distribution (bottom panels) of the central 3 kpc of the dwarf galaxy merger is shown in Fig. 3.1. The left panels show the system at the first encounter of the galaxies after 80 Myr. The gas gets compressed and reaches surface densities in excess of $\Sigma_{gas} \gtrsim 100\,{\rm M}_\odot\,{\rm pc}^{-2}$ (top panel), about two orders of magnitude higher than the isolated system (see Hu et al., 2016, 2017). At these high surface densities, cold clouds (the blue regions in the bottom panel) are already forming in the turbulent ISM. In the middle panels we show the system around the time of the second encounter at 170 Myr. At this time the merger has the highest star formation rate and the effect of supernova (SN) feedback is visible in the form of filaments and shells at high gas surface density and bubbles at low surface density. These bubbles are filled with hot gas (red-coloured, middle bottom panel) generated by SN explosions. The central super-bubble is generated by a massive star cluster (Lahén et al., 2019, 2020). Gas surface densities here can reach extreme values of $\Sigma_{\rm gas} \gtrsim 10^3\,{\rm M}_\odot\,{\rm pc}^{-2}$ when the system reaches its highest star formation rate. The ISM now shows a clear multi-phase structure with clumpy cold (blue), volume-filling warm (green) and

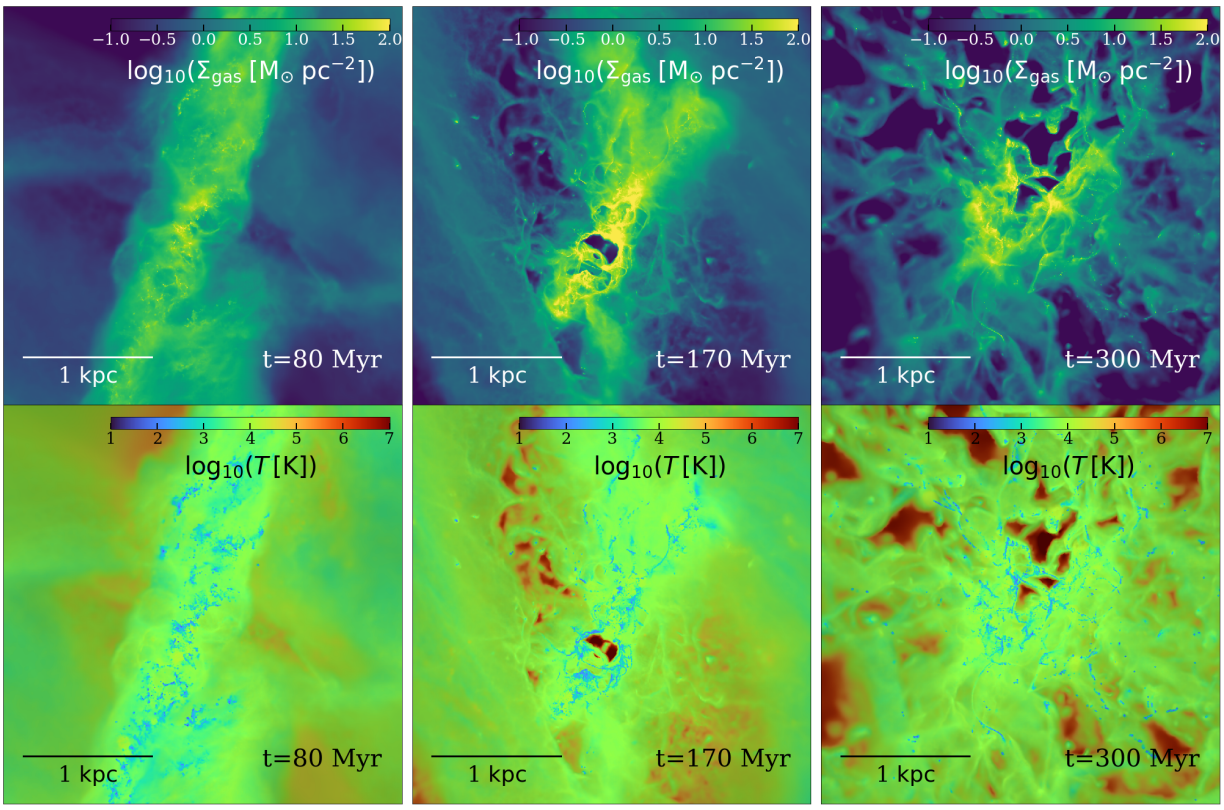

Figure 3.1: Gas surface density maps (top panels) and mass weighted gas temperature maps (bottom panels) of the central 3 kpc of the dwarf galaxy merger at three different stages: first encounter at 80 Myr (left), the second encounter and peak of star formation (middle panel), and at the new equilibrium configuration at 300 Myr (right panel). Dense (yellow) and cold (blue) gas is structured in clouds and filaments. The diffuse hot (red, bottom panel) gas is generated by supernova explosions.

hot (red) gas covering a temperature range of $10\,\mathrm{K} \lesssim T \lesssim 10^7\,\mathrm{K}$. The characteristic filamentary multi-phase structure of the ISM in the post-merger state is depicted in the right panels of Fig. 3.1, which show the system at 300 Myr. After the peak starburst at ~ 170 Myr, the remnant stays in such a highly turbulent state until the end of the simulation at 457 Myr. The diffuse hot gas (red-coloured gas in the bottom panels of Fig. 3.1) is generated by type II supernova explosions.

3.2 Star formation and gas flows in the starburst phase

We calculate the mass of the gas that moves outwards as a function of time, i.e. the outflow rate (OFR) of the gas, the mass of the gas that moves inwards as a function of time, i.e. the inflow rate (IFR) and the star formation rate (SFR) for the whole time of our simulation. In Fig. 3.2 we calculate the outflow rate (blue), the inflow rate (red) and the star formation rate (grey) at a radius of $r = 5$ kpc from the centre of the system for the time of the simulation. By dividing the outflow rate $\dot{M}_{\rm out}$ and the star formation rate $\dot{M}_*$ we define the "mass loading" η (purple in Fig. 3.2. That is: $\eta = \dot{M}_{\rm out}/\dot{M}_*$. As discussed in section 1.1.5, the mass loading measures how efficiently outflows remove gas from a system relative to the rate at which stars form in this system. In Fig. 3.2 we plot the mass loading as a function of time from 150 Myr, that is shortly before the main starburst (i.e. the second encounter of the galaxies at around 170 Myr) until the end of the simulation. This is done because as we explained in section 3.1 the system begins forming clumps, clouds and filaments efficiently after the second encounter of the individual dwarfs. The dashed purple line in Fig. 3.2 indicates unity.

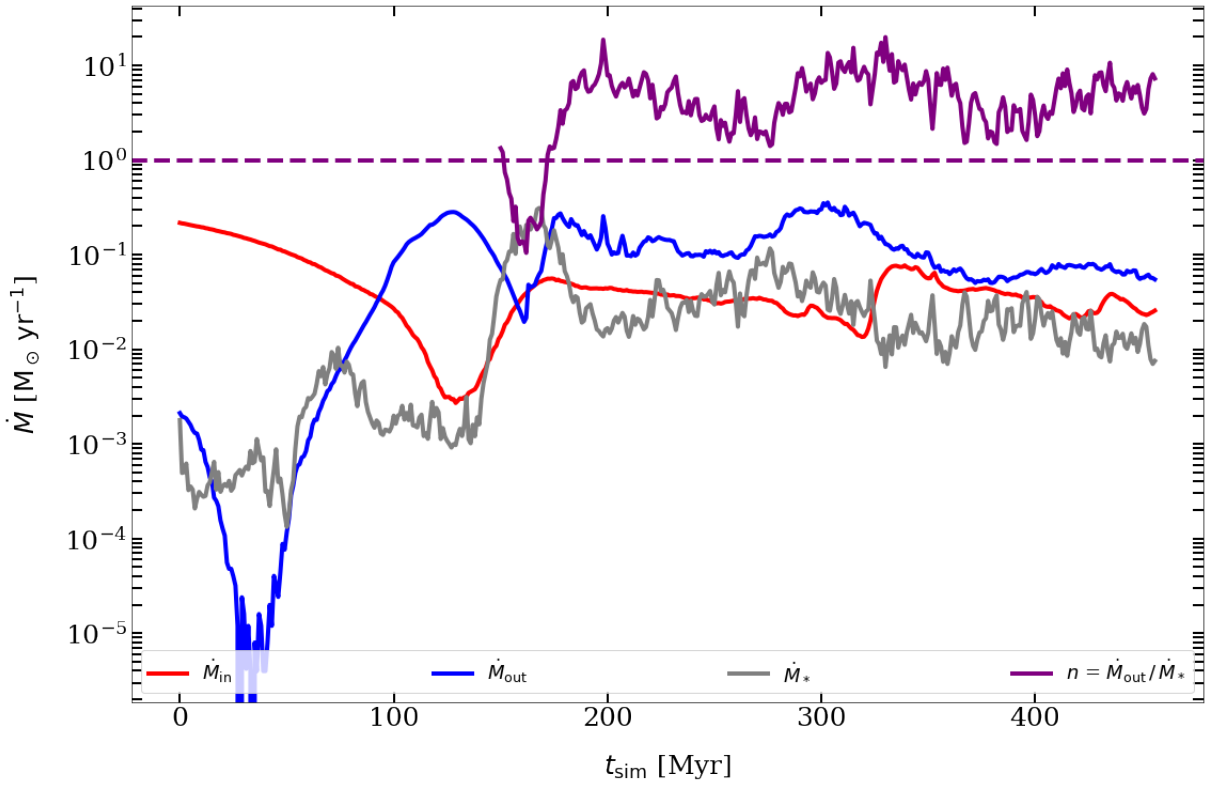

Figure 3.2: Outflow rate $\dot{M}_{\rm out}$ (blue), inflow rate $\dot{M}_{\rm in}$ (red) and star formation rate $\dot{M}_*$ (grey) at $r = 5$ kpc from the center of the system as a function of time, in units of $M_\odot yr^{-1}$. The mass loading $\eta = \dot{M}_{\rm out}/\dot{M}_*$ (purple) is plotted after the starburst when extensive star formation begins. The dashed line indicates unity.

As we see in Fig. 3.2, in the beginning most of the gas is in-flowing whereas the outflow rate is about two orders of magnitude lower that the inflow rate. However, after the first encounter (at around 80 Myr) of the galaxies the outflow rate begins increasing. After the second encounter (at around 170 Myr) of the galaxies the outflow rate has surpassed the inflow rate of the gas and stabilises at the post-merger equilibrium state of the system, dropping towards the end of the simulation. The inflow rate (red) never surpasses the outflow rate (blue) after the main starbursts indicating that not enough gas "fountains back" to prevent the depletion of the gas reservoir.

The interaction of the galaxies increases the star formation rate (grey) by about two orders of magnitude (between the time of the first and the second encounter of the dwarf galaxies) and drives the system into a starburst. The mass loading η after the starburst remains above unity until the end of the simulation indicating that gas is depleted from the system faster than new stars are born. The fact that outflow does not dissipate and the mass loading is above unity until the end of the simulation reveals a starburst that is extended in time.

In Fig. 3.2 we calculated the total outflow rate of the gas, the total inflow rate of the gas and the total star formation rate at the distance of $r = 5$ kpc from the centre of the system, in order to include the full extent of the activity regions. We should highlight that after calculating the star formation rate at different distances from the centre of the system, the results did not change significantly after 2 kpc from the centre indicating that this is the radius where the major star formation takes place. In Fig. 3.3 we repeat the same calculations as in Fig. 3.2 for the outflow rate (top panel) and the inflow rate (bottom panel), but for different radii from the centre of the system: from r = 1 kpc up to r = 5 kpc in steps of 1 kpc. The colour convention for the different radii of Fig. 3.3 will be used in all following figures where our analysis is split into different distances, that is: $r = 1$ kpc (blue), $r = 2$ kpc (orange), $r = 3$ kpc (green), $r = 4$ kpc (magenta) and $r = 5$ kpc (dark red).

In both panels of Fig. 3.3 we plot the star formation rate (SFR) in grey as in Fig. 3.2 for immediate comparison. During the first encounter of the galaxies (around 50-80 Myr) and the major merger (at around 170 Myr) the outflow rates (top panel) peak reaching $\dot{M}_{\rm out} \sim 1 {\rm M}_{\odot} {\rm yr}^{-1}$, which is not surprising considering that the tidal forces between the two dwarf galaxies that are in the process of merging drive strong outflows. The star formation rate (grey) follows the behaviour of the outflow rate, as expected since new stars are formed from the gas reservoir of the system and the events that impact the gas, dynamically or chemically, impact the star formation processes, as well.

Comparing the outflow rates at different distances from the centre of the system, we find that the larger the distance from the centre the bigger the delay of the outflow. In other words, comparing for example the behaviour of the outflow rate at $r = 1$ kpc (blue) to the outflow rate at $r = 5$ kpc (dark red), we notice that the outflow rate closer to the centre, therefore closer to the starburst event, peaks where the star formation rate peaks at the same time.

On the on the hand, the outflow rate at 5 kpc from the starburst has a similar behaviour to the outflow rate at 1 kpc and to star formation rate, but it peaks at later times than the star formation rate. This delay in the transmission of the information from the centre of the system to the outer regions is expected.

The inflow rates (lower panel) are higher in the beginning of the merger and they drop significantly (e.g. two orders of magnitude in the case of the inflow rate at 1 kpc -blue-) during the main merging event that triggers the starburst which drives outflows. The inflow rate of gas at r = 5 kpc (dark red line, bottom panel) from the centre is about an order of magnitude lower that the respective outflow rate (dark red line, top panel) during the whole post-merger equilibrium phase of the system (after 200 Myr). As in Fig. 3.2, this shows that the gas which "fountains back" is not able to replenish the gas reservoir and impede its depletion.

The mass loading η for the respective radii from the centre of the system of Fig. 3.3 is calculated in Fig. 3.4 where the dashed horizontal line indicates unity. The mass loading remains significantly above unity at all distances from the centre that we use to calculate it (i.e. r = 1, 2, 3, 4 and 5 kpc), except for the time of the main merger event ($\sim$ 170 Myr) where the star formation is highest ($\eta = \dot{M}_{\rm out}/\dot{M}_{*}$). In the post-merger equilibrium phase of the system (roughly after 200 Myr) the mass loading remains above unity at all distances from the centre, from 1 kpc up to 5 kpc revealing a starburst extended in space. Combining this result with the main result from Fig. 3.2 (i.e. that the starburst is extended in time) it follows that in our simulation we have a surprisingly extended starburst both in space and time.

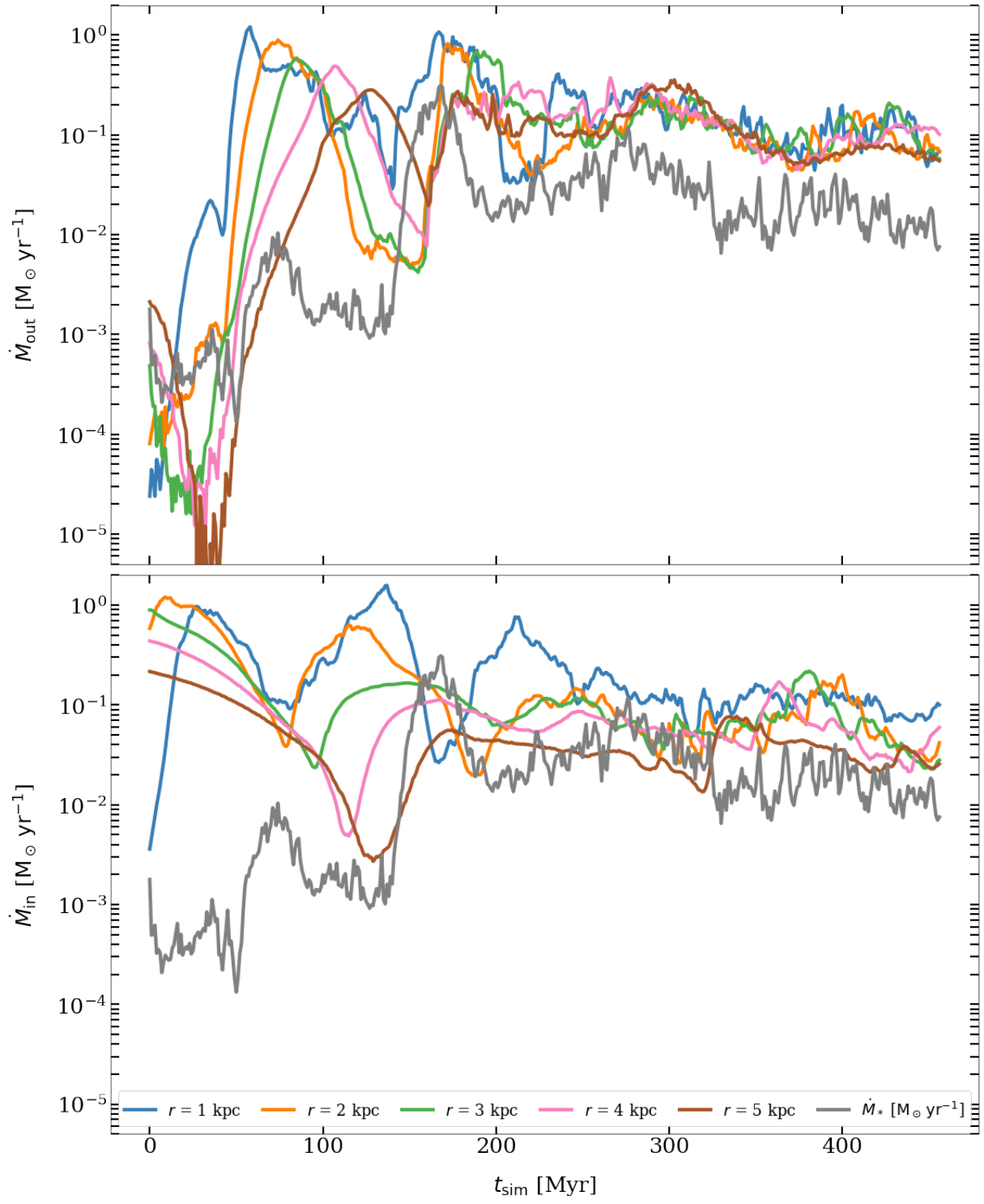

Figure 3.3: Outflow rates (OFR) (top panel) and inflow rates (IFR) (bottom panel) at different radii from the centre, from 1 kpc up to 5 kpc. The grey line shows the star formation rate (SFR) as a function of time. The mass flow rates are in units of $M_{\odot} yr^{-1}$.

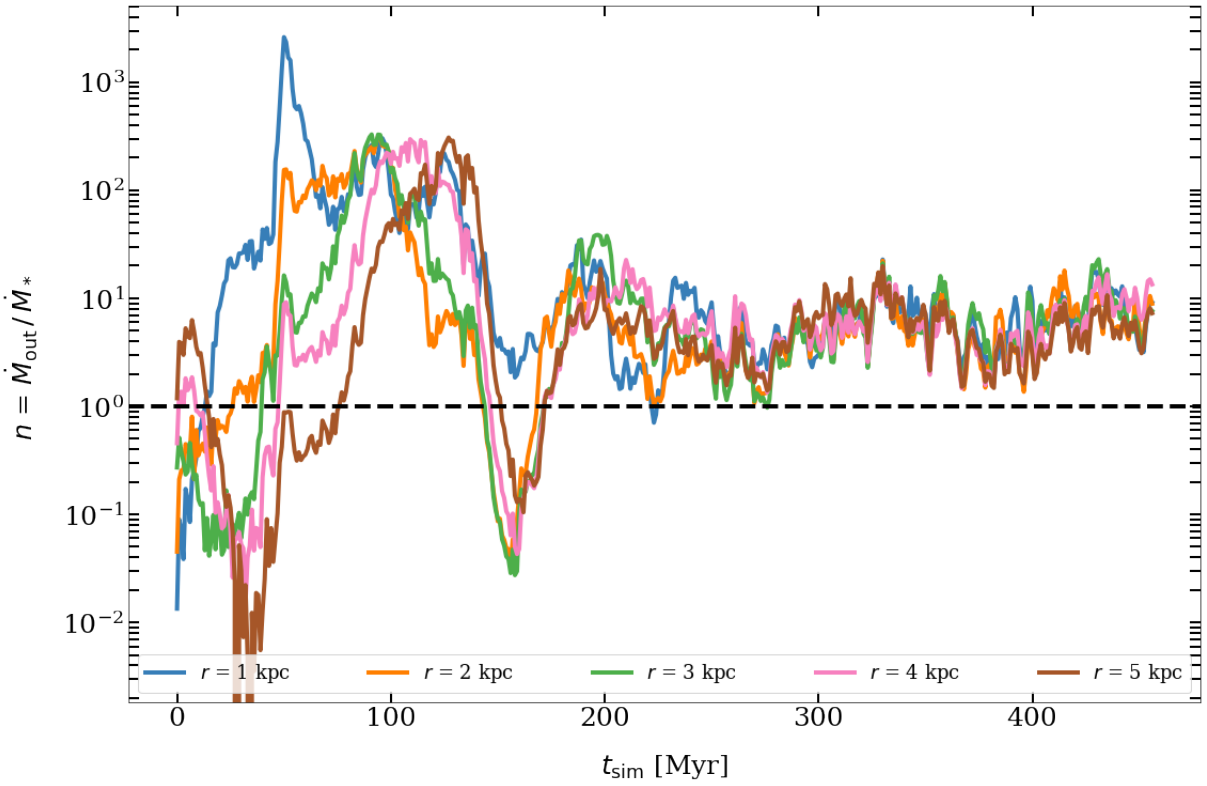

Figure 3.4: Mass loading η, defined as the fraction of the outflow rates (OFR) at different radii from the centre (from 1 kpc to 5 kpc) to the star formation rate (SFR), after the starburst. The horizontal dashed line indicates unity.

3.3 Gas phases separated by temperature

An interesting question is what is the behaviour of the outflow rate in different temperatures and more specifically what is the outflow rate of the cold gas reservoir from which stars form. As we discussed in section 1, the multi-phase ISM can be divided in phases of different temperatures (i.e., cold, warm and hot phases).

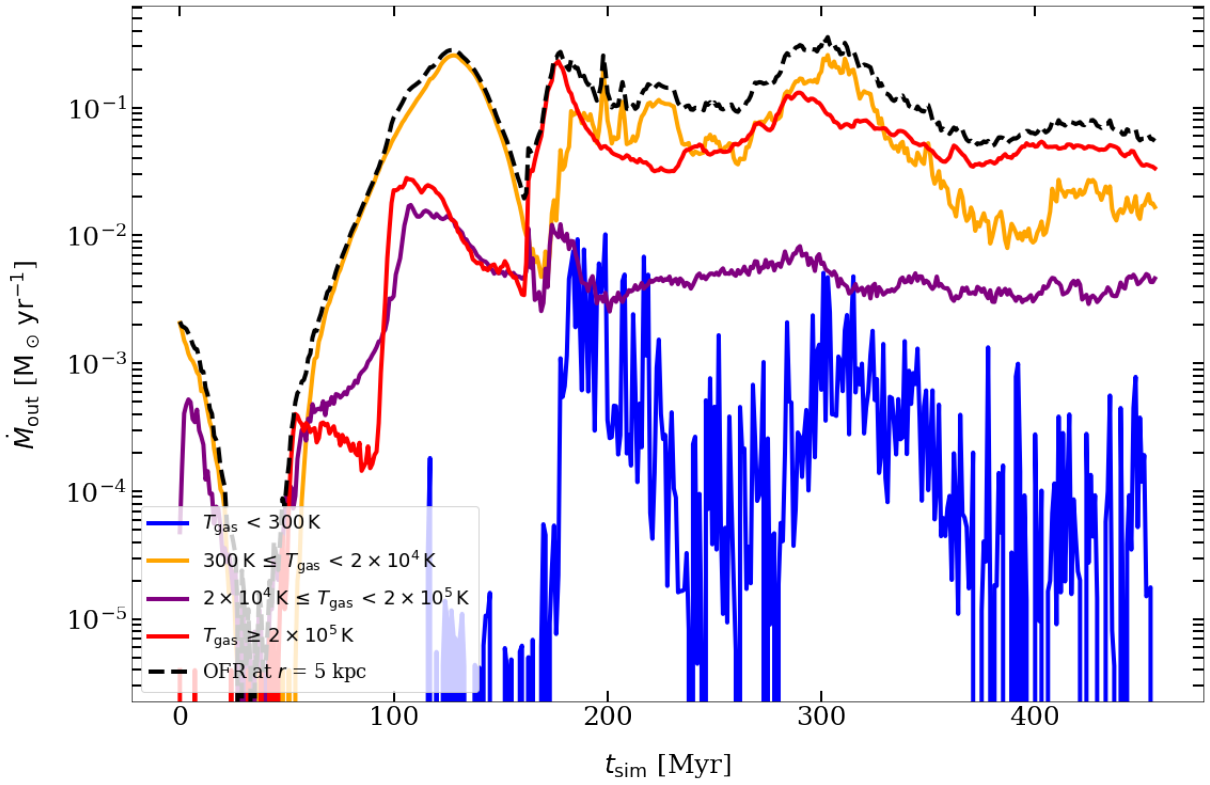

Figure 3.5: Outflow rates (OFR) at 5 kpc from the center for different gas temperatures as a function of time in units of $M_\odot yr^{-1}$. The dashed line indicates the total OFR of Fig. 3.2.

In Fig. 3.5 we calculate the outflow rate at a radius of 5 kpc from the centre (which incorporates the active region of interest) for gas at different temperature regimes: "cold" with temperature $T_{\rm gas} < 300\,{\rm K}$, "warm" with temperature $300\,{\rm K} \leq T_{\rm gas} < 2 \times 10^4\,{\rm K}$, "warm-hot" (this is the meta-stable phase of the warm ionised medium we discussed in section 1.1.1) with temperature $2 \times 10^4\,{\rm K} \leq T_{\rm gas} < 2 \times 10^5\,{\rm K}$ and "hot" with temperature $T_{\rm gas} \geq 2 \times 10^5\,{\rm K}$. The dashed line traces the total outflow rate of Fig. 3.2 for immediate comparison. The highest mass outflow rate $\dot{M}_{\rm out}$ is in the "warm phase" of the ISM and it is quite close to the total outflow rate. This is not surprising since most of the mass of the gas component of the ISM is in the warm phase (see section 1.1.1). The extended starburst drives outflows until the end of the simulation. The

outflow rate of the cold gas (blue) ($T_{\rm gas} < 300\,{\rm K}$) is lower than the outflow rates of the rest of the temperature regimes, indicating that the cold gas is not depleted from the system. This is also evident from the ongoing star formation even towards the end of the simulation (see e.g. Fig. 3.2).

Working in a similar fashion as in Fig. 3.2, we calculate the mass loading for the same temperature phases and for different distances (from 1 kpc to 5 kpc) from the centre as in Fig. 3.4 and we present the results in Fig. 3.6. In the first panel, the mass loading is calculated for the "cold" phase, in the second panel for the "warm" phase, in the third panel for the "warm-hot" phase and in the fourth panel for the "hot" phase. The colour convention for the different distances from the centre of the system is the same as in the previous Figs. 3.3 and 3.4.

In the post-merger stage of the system (after 170 Myr) the mass loading of the cold gas (first panel) is below unity, confirming that the cold gas is not yet depleted from the system even at the later stages of the simulation. However, the "warm" gas (second panel) has mass loading above unity, since it experiences the strongest outflows as seen in Fig. 3.5. The same does not apply to the meta-stable "warm-hot" phase of the gas (third panel) where the mass loading during the post-merger stage of the system remains below unity. This phase corresponds to the "warm ionised medium" we discussed in section 1.1.1 and it can easily move up to the "hot" phase if it is further heated by e.g. supernova (SN) explosions. The more stars are forming during the earlier stages of the simulation the more core-collapse supernovae are created when these stars die during the later stages of the simulation which heat up the ISM through blast-waves produced during the SN explosions. This provides the "hot" phase with more gas that can be accelerated to create outflows, as shown by its mass loading (fourth panel) that is above unity at the later stages of the simulation.

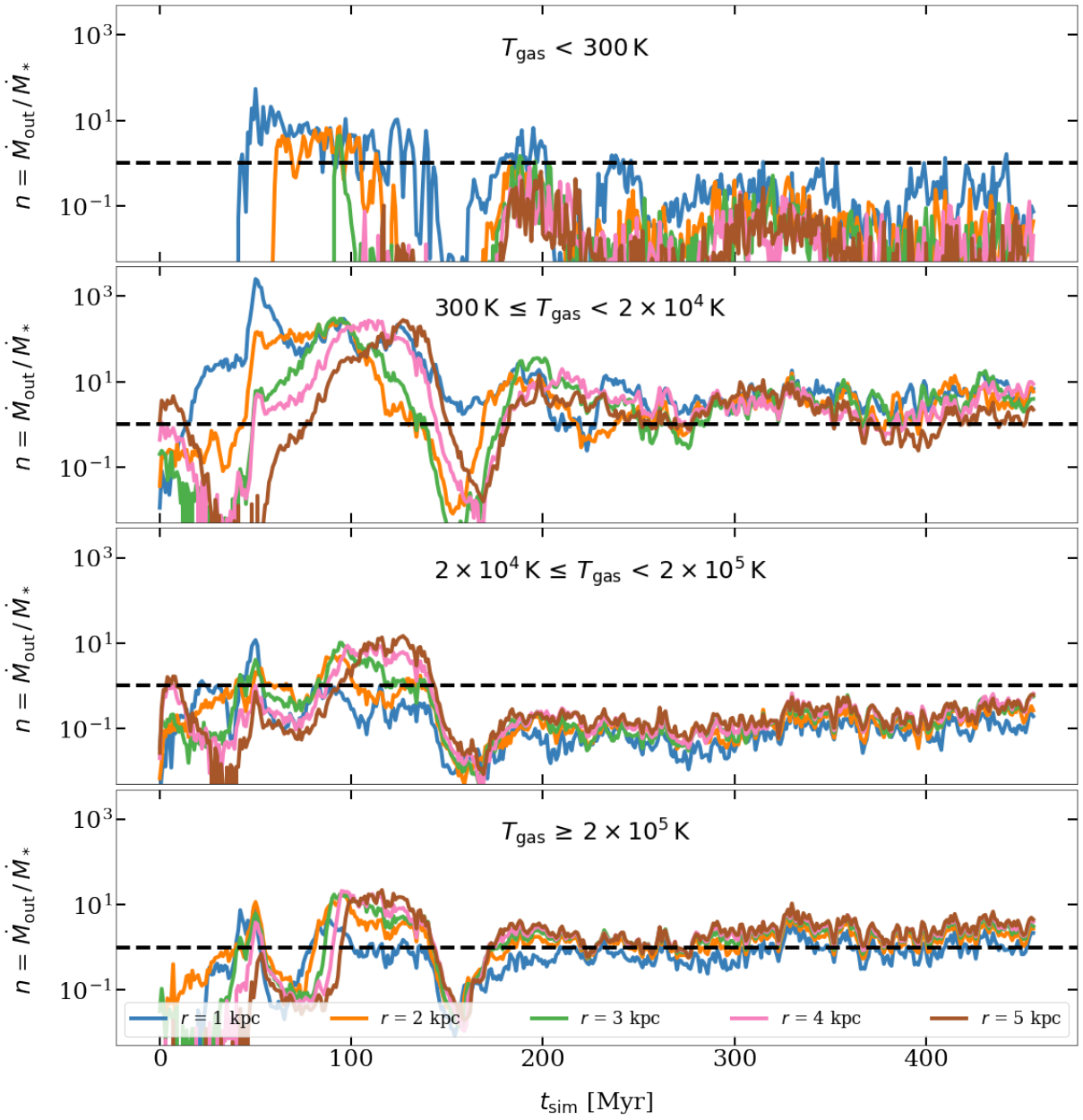

Figure 3.6: Mass loading η at different radii from the centre of the system and calculated for different gas temperatures. The different temperature regimes are stated in each panel and the different radii from the centre follow the colour convention of the previous figures (see e.g. Fig. 3.3). From top to bottom: we calculate the mass loading η for the "cold phase" of the gas: $T_{\rm gas} < 300\,{\rm K}$ (*top panel*), the "warm phase": $300\,{\rm K} \leq T_{\rm gas} < 2\times10^4\,{\rm K}$, the "warm-hot phase": $2\times10^4\,{\rm K} \leq T_{\rm gas} < 2\times10^5\,{\rm K}$ and the "hot phase" of the gas: $T_{\rm gas} \geq 2\times10^5\,{\rm K}$ (*bottom panel*). In every panel the horizontal dashed line indicates unity.

3.4 Gas phases separated by chemical species

As discussed in section 2, our simulation is poor in H_2. Therefore, we expect that the outflow rate $\dot{M}_{\rm out}$ and the mass loading η of H_2 gas will be low. By calculating the outflow rates of the different phases of hydrogen, i.e. molecular H_2 (top panel), ionised H^+ (middle panel) and atomic H (bottom panel) in Fig. 3.7, we verify that indeed the outflow rates of H_2 are low for all distances from the centre (from 1 kpc up to 5 kpc) compared to H^+ and H.

Focusing at the time shortly before the major starburst (from around 150 Myr) until the end of the simulation run we see that there is a rise of the outflow rate $\dot{M}_{\rm out}$ of H^+ (middle panel) during the starburst for all distances r from the centre of the system, then there is a small drop after the starburst and then the outflow rate is roughly stable during the final post-merger equilibrium state of the system.

From the time of the starburst ($\sim$ 170 Myr) until the end of the simulation the outflow rate measured at r = 5 kpc (dark red) remains the highest compared to the outflow rates measured at shorter distances from the centre (i.e. r = 1, 2, 3 and 4 kpc). This happens because the ionised hydrogen H^+ gas is very diffused due to its high temperature (subsequent high thermal kinetic energy of the ions). However, the differences between the different distances are small. The outflow rates of H^+ follow the behaviour of the starburst: they rise during the main merging event, then they lower and they stabilise during the post-merger equilibrium. The smaller the radius from the centre the faster the information of a event happening in the centre reaches this radius. See e.g. the blue line representing r = 1 kpc from the centre compared to the dark red line representing r = 5 kpc from the centre of the bottom panel of Fig. 3.7.

At the time of the starburst ($\sim$ 170 Myr) the outflow rate of atomic hydrogen H measured at 1 kpc from the centre (blue line) is higher than the outflow rate at 5 kpc from the centre (dark red). From then on the behaviour of the outflow rate at 1 kpc resembles the behaviour of the star formation rate (SFR), whereas the outflow rate measured at 5 kpc is delayed compared to the SFR. This expected delay in the transmission of the information with distance is clearly shown in the bottom panel of Fig. 3.7 for the delay growing the further away from the centre we measure the outflow rate. As explained in section 1.1.4, the atomic hydrogen H is more diffuse than the molecular H_2. Therefore, this delay due to distance is easily observed when analysing atomic hydrogen (bottom panel), but not when analysing molecular hydrogen which is mostly concentrated in dense regions closer to centre (top panel).

As the total outflow rate (see e.g. Fig. 3.2), the outflow rates of H^+ and H do not disappear towards the end of the simulation, but stabilise at around 0.1 $M_\odot yr^{-1}$ for all measured distances, verifying again the existence of a surprisingly extended starburst both in space and time.

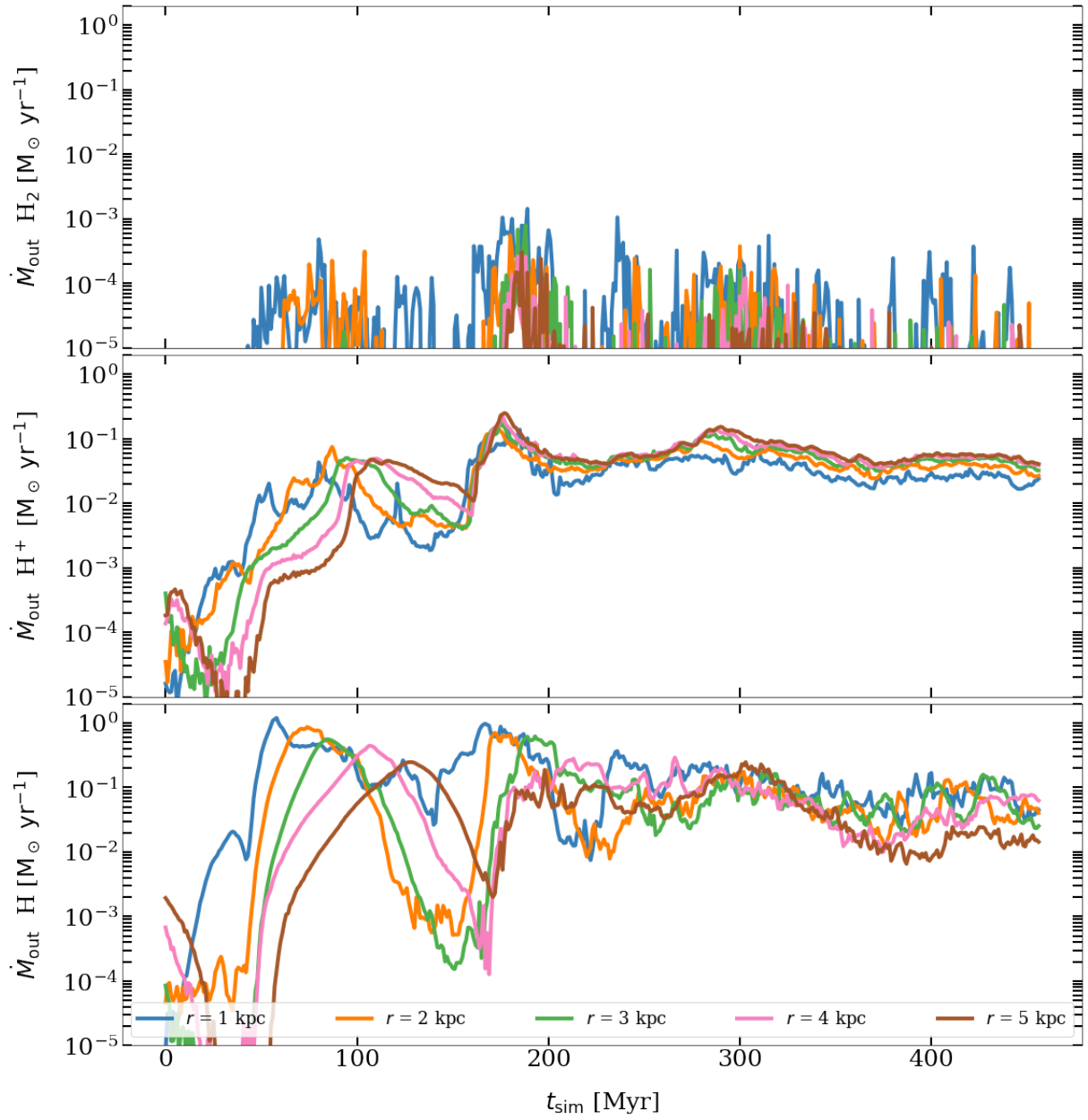

Figure 3.7: Outflow rates (OFRs) for different phases of the gas at different radii from the centre of the system. The different radii from the centre follow the colour convention of the previous figures (see e.g. Fig. 3.3). *Top panel*: Outflow rate of molecular hydrogen (H_2) gas, *Middle panel*: Outflow rate of ionised hydrogen (H^+) gas, *Bottom panel*: Outflow rate of atomic hydrogen (H) gas.

Calculating the mass loading η for the different phases of hydrogen (which correspond to the different phases of the ISM, as explained in section 1.1.1) we produce Fig. 3.8 that shows the mass loading of molecular hydrogen H_2 (top panel), ionised hydrogen H^+ (middle panel) and atomic hydrogen H (bottom panel) compared to the time of the simulation $t_{\rm sim}$. The horizontal dashed line in all panels indicates unity and the colour convention for the different distances from the centre is the same as in the previous figures (see e.g. Fig. 3.3). During the merging of the two identical dwarf galaxies that we use to create this simulated merger (see section 2) there are strong outflows due to the tidal forces from the individual dwarfs (e.g. Figs. 3.2, 3.4). Therefore, from the beginning of the simulation until the main merger event that leads to the major starburst ($\sim$ 170 Myr), the outflow rates have -as expected- higher values in all phases of hydrogen (Fig. 3.7) and the same applies to the mass loading (Fig. 3.8). Since our simulated merger is a system poor in H_2 the outflow rate of molecular hydrogen gas is low (see top panel of 3.7), therefore the mass loading of H_2 is low and more accurately, it remains below unity throughout the simulation (top panel of Fig. 3.8).

The mass loading of ionised hydrogen H^+ reaches its lowest values during the main starburst (around 170 Myr) when the star formation is highest and then stabilises above unity until the end of the simulation. This holds for all the distances from the centre that we we use to measure the mass loading (i.e. r = 1, 2, 3, 4 and 5 kpc). The atomic hydrogen H (bottom panel of Fig. 3.8) behaves in a similar manner as H^+, with a mass loading value stabilising -mostly- above unity during the post-merger equilibrium. Towards the end of the simulation at 5 kpc from the centre (dark red) there is a small drop in the outflow rate of H (Fig. 3.7) which is reflected with a small drop in the value of the respective mass loading of H (bottom panel of Fig. 3.8, dark red line) below unity. This could be a sign of depletion of atomic hydrogen in the system. However, also in the case of our "hydrogen-phases-analysis", the extended starburst both in space and time is confirmed.

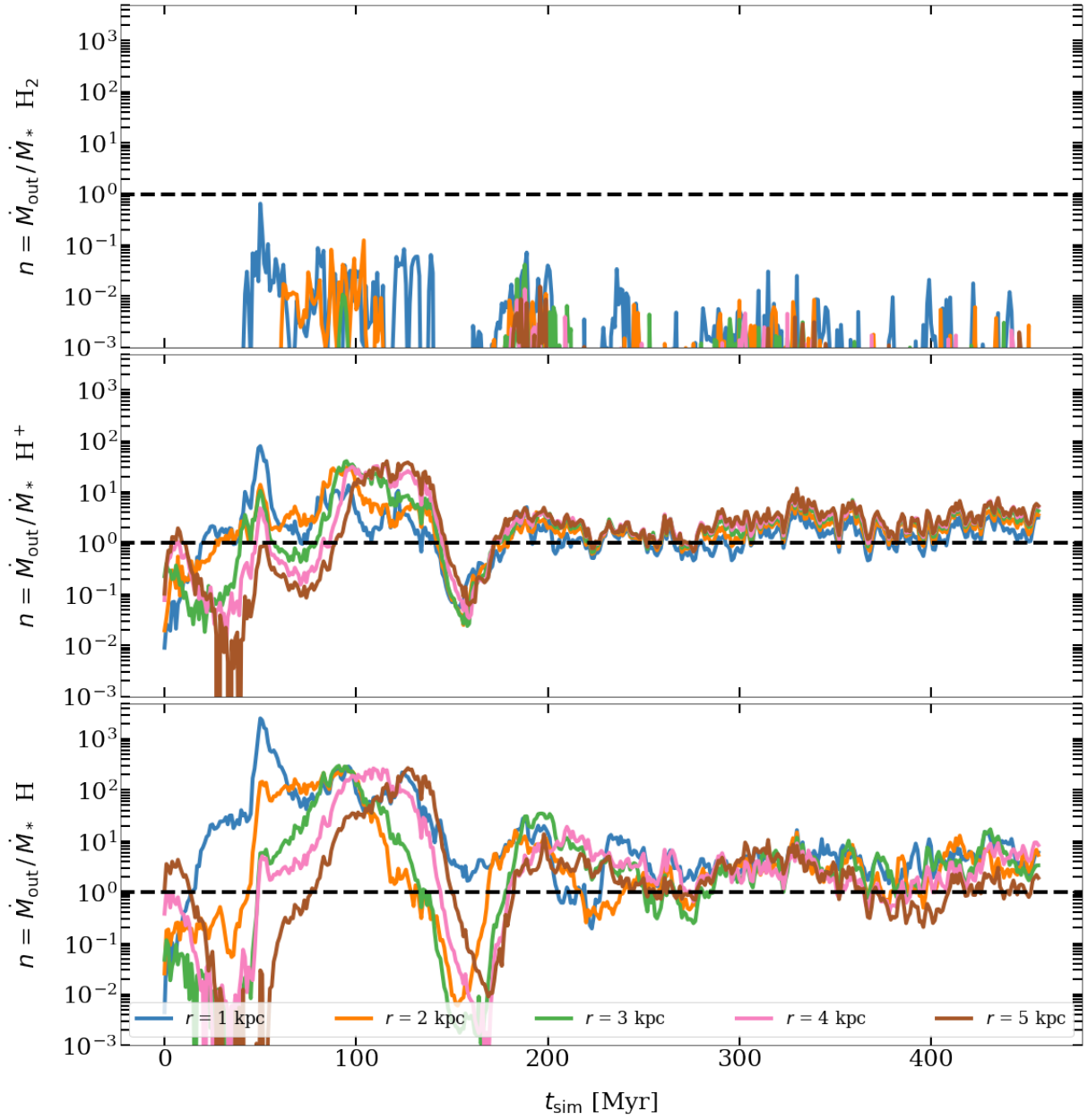

Figure 3.8: Mass loading η, defined as the fraction of the outflow rates (OFRs) of Fig. 3.7 at different radii from the centre of the system to the star formation rate (SFR) for the different phases of the gas of Fig. 3.7. *Top panel*: Mass loading of molecular hydrogen (H_2) gas, *Middle panel*: Mass loading of ionised hydrogen (H^+) gas, *Bottom panel*: Mass loading of atomic hydrogen (H) gas. The different radii from the centre follow the colour convention of the previous figures. The horizontal dashed line indicates unity.

3.5 Metal mass flows

We repeat the analysis of the previous section 3.4, but this time for the "metals". In Astrophysics, all chemical elements heavier than hydrogen (and helium) are referred to as "metals", even though this definition includes elements like carbon and oxygen, which are not typically thought of as metals in the traditional sense. As discussed in section 2, in our simulation we trace the mass of hydrogen (H), helium (He) and of ten "metals": nitrogen (N), carbon (C), oxygen (O), silicon (Si), magnesium (Mg), iron (Fe), sulphur (S), calcium (Ca), neon (Ne) and zinc (Zn). In this chapter, in the definition of metals we also include helium, thus analysing helium and the ten aforementioned elements together, keeping only the analysis of hydrogen separate.

In Fig. 3.9 we plot the time evolution of the mass outflow rates $\dot{M}_{\rm Z,out}$ of the "metals" mentioned above for different radii r from the centre of the system. The mass outflow rates calculated at the different radii from the centre (r = 1, 2, 3, 4 and 5 kpc) follow the colour convention of the previous figures (see e.g. top panel of Fig. 3.3). The behaviour of the metal mass outflow rate is similar to the behaviour of the total outflow rate (see Fig. 3.3 or the H^+ and H outflow rate (see lower panels of Fig. 3.7). However, the metals outflow rate after the major starburst (at $\sim$ 170 Myr) is at about two orders of magnitude lower than the total outflow and at about one order of magnitude lower than the H^+ outflow rate (irrespective of the distance from the centre that the outflow rate is measured). This is because the system we simulate is metal-poor which is typical for such systems (see section 1.2).

Using the outflow rates of Fig. 3.9 and the star formation rate we calculate the mass loading $\eta_{\rm Z}$ for metals for the different distances r of Fig. 3.9. The results are shown in Fig. 3.10, where the The different radii from the centre of the system (i.e. where each outflow rate is measured) follow the colour convention of the previous figures (see e.g. Fig. 3.9). The mass loading of the metals before the major starburst (before roughly 170 Myr) is higher than after the starburst, but overall below unity with the exception of a brief phase above unity at r = 1 kpc from the centre (blue line) before the first encounter of the system ($\sim$ 50 Myr). The metals mass loading remains below unity after the starburst until the end of the simulation, due to the fact that the system remains metal-poor throughout the time of the simulation.

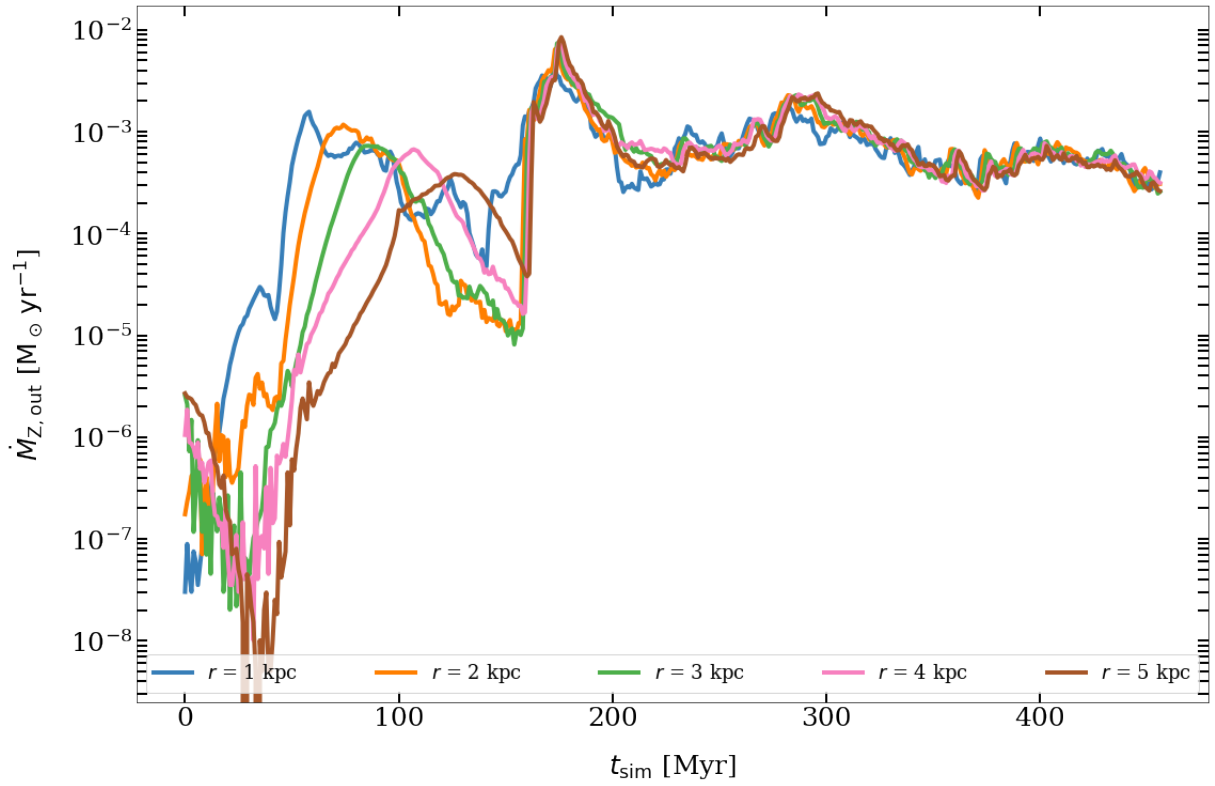

Figure 3.9: Outflow rates of the metals mass of the gas at different radii r from the centre of the system (r = 1, 2, 3, 4 and 5 kpc). The different radii follow the colour convention of the previous figures. The "metals" traced in this simulation are: He, N, C, O, Si, Mg, Fe, S, Ca, Ne, Z. The outflow rate of metals after the major starburst (i.e. after $\sim$ 170 Myr) is roughly two orders of magnitude lower than the total outflow rate of Fig. 3.3 (top panel). This is expected since we simulate a metal-poor system

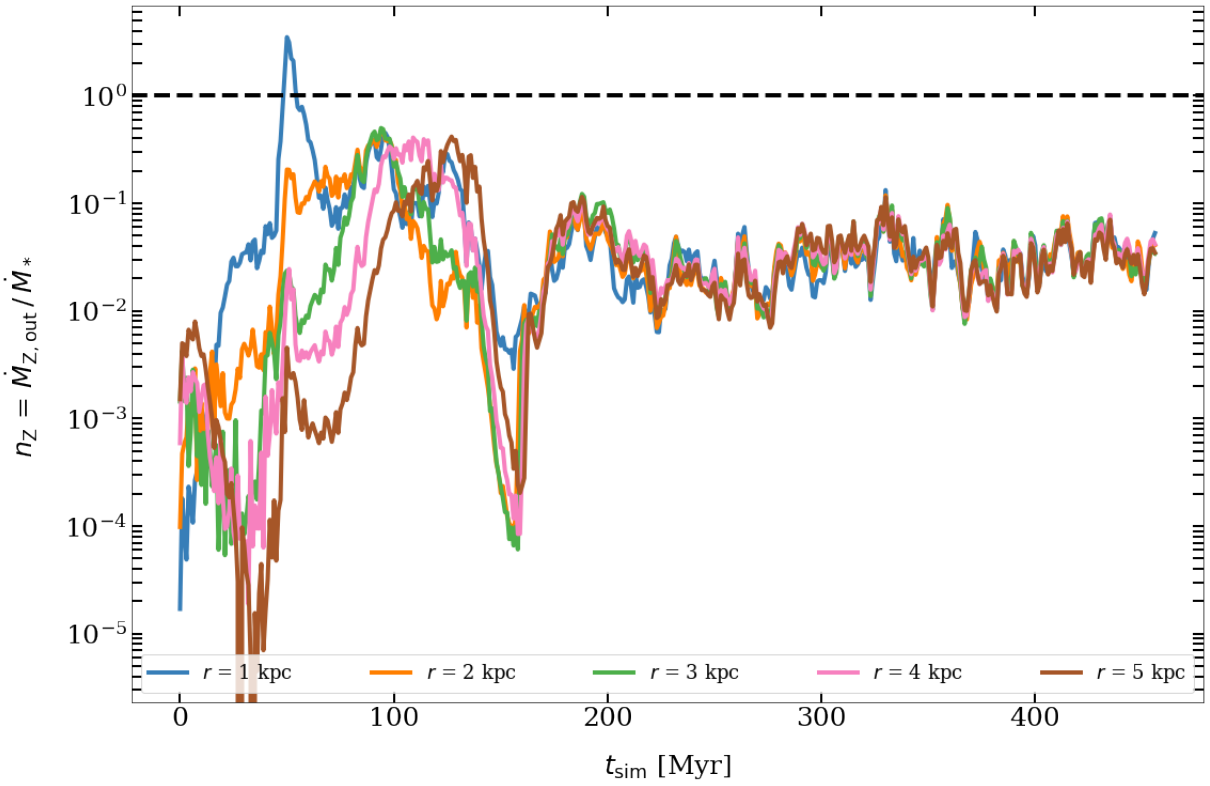

Figure 3.10: Mass loading η_Z for metals, defined as the fraction of the metals gas mass outflow rate $\dot{M}_{Z,\mathrm{out}}$ at different radii of Fig. 3.9 to the star formation rate $\dot{M}_*$. The dashed line indicates unity.

In Fig. 3.11 we calculate the outflow rates of metals at the same distance from the centre r = 5 kpc, but for the different gas temperature phases: "cold": $T_{\rm gas} < 300\,{\rm K}$ (blue), "warm": $300\,{\rm K} \leq T_{\rm gas} < 2\times10^4\,{\rm K}$ (orange), "warm-hot": $2\times10^4\,{\rm K} \leq T_{\rm gas} < 2\times10^5\,{\rm K}$ (purple) and "hot": $T_{\rm gas} \geq 2\times10^5\,{\rm K}$ (red).

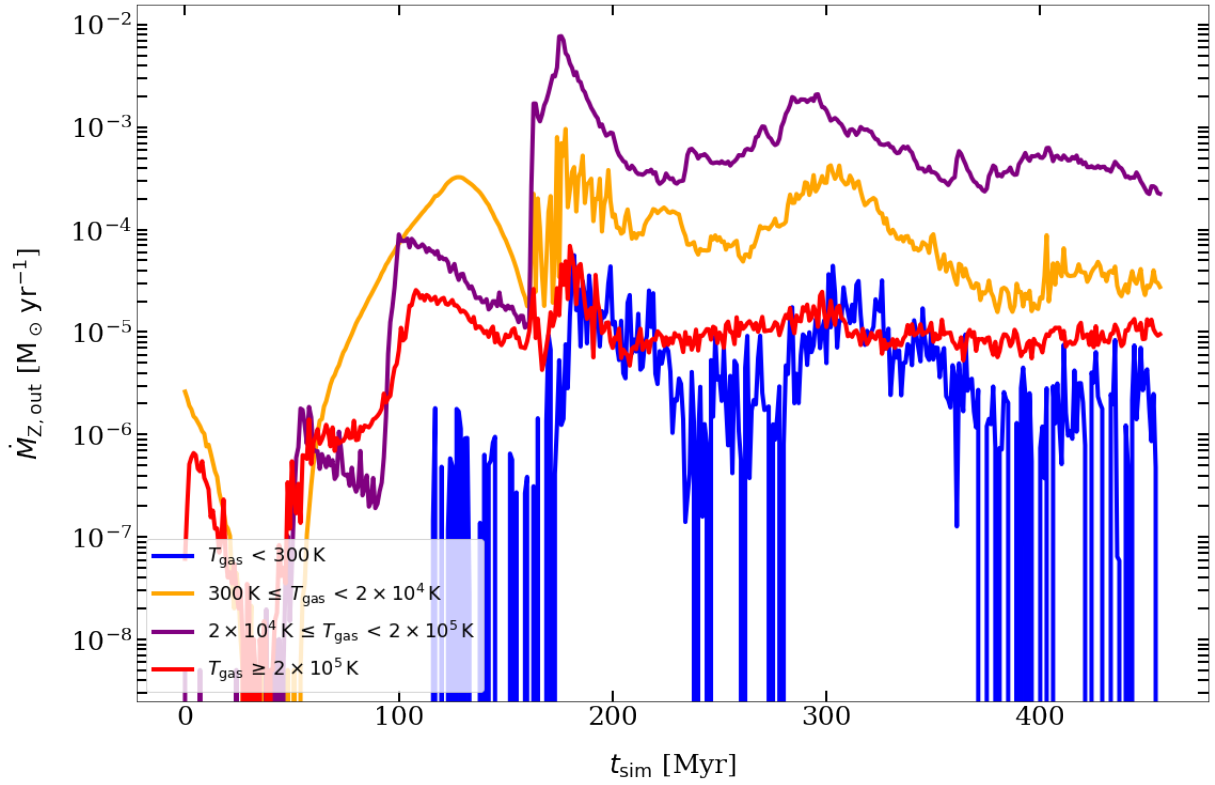

Figure 3.11: Outflow rates $\dot{M}_{\rm Z,out}$ of the metals mass of the gas measured at radius r = 5 kpc from the centre of the system. The metal outflow rates are measured for different temperature phases of the gas: "cold": $T_{\rm gas} < 300\,{\rm K}$ (blue), "warm": $300\,{\rm K} \leq T_{\rm gas} < 2\times10^4\,{\rm K}$ (orange), "warm-hot": $2\times10^4\,{\rm K} \leq T_{\rm gas} < 2\times10^5\,{\rm K}$ (purple) and "hot": $T_{\rm gas} \geq 2\times10^5\,{\rm K}$ (red).

When considering the total gas, the strongest outflows are detected in the "warm" and "hot" phases (see Fig. 3.5). However, when we calculate the outflow rates for the metals, the strongest outflows are measure in the "warm-hot" phase of the ISM (purple line in Fig. 3.11). After the major starburst, the metallicity outflow rate $\dot{M}_{\rm Z,out}$ is roughly two orders of magnitude lower than the total outflow rate $\dot{M}_{\rm out}$ in the "warm" phase (orange line in Fig. 3.5), and one order of magnitude lower than the total outflow rate $\dot{M}_{\rm out}$ in the "warm-hot" phase (purple line in Fig. 3.5). The metal outflows in the different temperature phases are overall weaker compared to the total gas outflows, as expected in such a metal-poor system. Nevertheless, we should note that even though the metal outflow rates in the "warm-hot" phase are never as high as the outflow rates

of the total gas, when considering only the metals of the system, the "warm-hot" temperature regime is the one that carries out the most material. The metal outflow in the "cold" phase is the weakest, as it is the total cold gas outflow (blue line in Fig. 3.5). The cold phase of the gas is not efficiently depleted neither in the case of metals.

3.6 Discussion

Galaxy mergers may result from gravitational interactions between galaxies (see e.g. Hopkins et al., 2008; Lotz et al., 2011) and can impact significantly the morphology (e.g. Toomre & Toomre, 1972; Patton et al., 2016) and the evolution of the system by triggering its star formation (see e.g. Ellison et al., 2008; Scudder et al., 2012) or accretion onto the central black hole (Ellison et al., 2011; Satyapal et al., 2014). Galaxy mergers can lead to starbursts, i.e. galaxies with bursts of high star formation rate, as discussed in section 1.2 of the present work. A fraction of these galaxies are known in literature as "post-starbursts", i.e. galaxies that have recently gone through a period of very high star formation that was abruptly cut short (see e.g. Dressler & Gunn, 1983). Such post-starburst galaxies have their merger-triggered high star formation terminated , after a short period of time, due to feedback that removes or heats up the gas reservoir from which stars form (Springel, 2005; Hopkins et al., 2008).

The duration of starbursts has been determined in individual galaxies (Schaerer et al., 1999; Mas-Hesse & Kunth, 1999; Tremonti et al., 2001) and in galaxy samples (Thornley et al., 2000; Harris et al., 2004) and was found to be around 5-10 Myr. These time-frames are comparable to the lifetimes of massive stars. The idea behind these estimates is that the massive star formation during a starburst results in stellar winds and supernovae (SNe) explosions that may disrupt the gas that sustains the star formation, thus putting an end to the starburst. In literature, this is often called the "self-quenching" hypothesis, meaning that the starburst itself causes its end. This hypothesis has been used extensively both in observational works (see e.g. Schaerer et al., 1999; Mas-Hesse & Kunth, 1999; Thornley et al., 2000; Tremonti et al., 2001; Harris et al., 2004) and in theoretical studies (see e.g. Kauffmann et al., 1994; Hogg & Phinney, 1997; Ferguson & Babul, 1998; Stinson et al., 2007), that assume timescales ≤ 10 Myr for the duration of a starburst.

As shown by our analysis, the starburst in our simulation is surprisingly extended both in space and time: it goes on for ~ 300 Myr and it spans at least up to a radius of $r = 5$ kpc from the centre of the system.

McQuinn et al. (2010) measured the duration of starbursts in twenty dwarf galaxies, based on the star formation histories derived from resolved stellar population data collected with the Hubble Space Telescope. The starburst durations they detected vary from 450 to 650 Myr in 15 of the

dwarf galaxies in their sample and up to 1.3 Gyr in four galaxies. These time-frames are comparable to the dynamical timescales for each system. A possible explanation is that in these systems the "self-quenching" hypothesis does not hold, because the starburst is not locally powered by the deaths of the massive stars through SNe explosions, but it is a "global" phenomenon that expands in a big portion of the galaxy and consists of a lot of individual bursts that go on for hundreds of Myr. This hypothesis seems quite plausible for our simulation, as well given that the starburst detected in our system expands not only in time, but also in space. These findings support prior claims that starbursts can continue for far longer than a few Myr (Calzetti et al., 1997; Greggio et al., 1998; Meurer, 2000; Schulte-Ladbeck et al., 2001).

Outflows generated by starbursts may feed the intergalactic medium (IGM), thus changing the host galaxy's morphology, kinematics and evolutionary course. Gas outflows that are generated due to feedback from SN explosions in low-mass galaxies -like the system we simulate- are especially significant. In such low-mass systems, the escape velocities are lower which makes it "easier" for the feedback mechanisms to drive gas-rich outflows, which enrich the IGM. Much more easily than gas, metals from the supernova ejecta in metal-rich outflows are driven to speeds greater than the galaxy's escape velocity (Mac Low & Ferrara, 1999; Martin et al., 2002; Tolstoy et al., 2009). Longer starbursts can more easily fuel such galactic outflows, therefore their impact is more significant if they are sustained over time-frames of a few hundred Myr for the bulk of dwarf starburst galaxies.

3.7 Summary

Through our analysis, we discovered an extended starburst both in space and time. The outflows measured in our system cannot deplete the gas reservoir, from which stars form, completely during the time of the simulation, so there is ongoing star formation until the end of the simulation and at distances up to 5 kpc from the centre of the system. However, the inflow rates $\dot{M}_{\rm in}$ measured after the major starburst, are systematically lower than the $\dot{M}_{\rm out}$, therefore it is possible that the gas reservoir of the system will be depleted within a few dynamical times. The outflow rates measured at different distances from the centre of the system are stronger closer to the centre, but they do not drop to zero towards the outer regions, they still exist. The strongest outflows are detected in the "warm" phase of the ISM ($300\,{\rm K} \leq T_{\rm gas} < 2\times10^4\,{\rm K}$) carrying out mostly atomic (H) and ionised (H^+) hydrogen. The outflows carry also metals especially at temperatures: $2\times10^4\,{\rm K} \leq T_{\rm gas} < 2\times10^5\,{\rm K}$ ("warm-hot" phase).

The extended starburst has a very big impact on the morphology and the evolution of the system. It drives multi-phase galactic outflows that accelerate and/or heat up the gas, thus depleting the cold gas reservoir from which stars form. On the other hand, it drives extensive star formation in

the system providing us with a detailed model for the multi-phase ISM and a perfect environment to study the formation and evolution of cold star-forming clouds, which is the subject of the following chapter.

Chapter 4

The cold cloud properties of a low metallicity starburst

In this chapter, we present the findings from the study of our simulation's cold gas. Our analysis reveals that the cold ($T_{\rm gas} < 300$ K) star-forming gas is structured in clumps and filaments. We identify hundreds of cold clouds in each snapshot of the simulation with the typical irregular structure, masses and sizes of molecular clouds and we trace their lifecycle. The simulated cold clouds follow a power law mass function (CMF): $dN/dM \propto M^{\alpha}$ with $\alpha_{\rm mean} = -1.78(\pm 0.08)$, well in agreement with the observations. The slope α remains constant throughout the time of the simulation and is roughly the same for different gas particle density thresholds indicating self-similar structure. The simulated cold cloud properties follow the Larson relations and are well in agreement with observations. Tracing the lifecycle of the cold clouds, we discover a correlation between the peak mass and the size of the cold clouds when they reach their peak mass: $R_{M_{\rm max}} \propto M_{\rm max}^{1/2}$. High mass clouds live longer (up to 8 Myr) than lower mass clouds with peak mass $M_{\rm max} < 10^4 M_{\odot}$.
The results of this chapter are ready to be submitted to the "*Monthly Notices of the Royal Astronomical Society" (MNRAS)* for publication.

4.1 Evolution of the cold ISM

As shown in Fig. 3.1 the cold gas is organised in compact clumps and filaments. As explained in section 2, to identify these structures which are the reservoir for the star forming gas in the simulations of such metal poor systems (see Hu et al., 2016, 2017, for a detailed analysis) we use a friends-of-friends (FoF) algorithm implemented in our analysis toolkit *pygad* (Röttgers et al., 2020). We look for FoF groups within the cold, i.e. $T_{\rm gas} < 300$ K and dense, i.e. $\rho_{\rm gas} > 100\,{\rm cm}^{-3}$ gas at every simulation snapshot (which are separated by 1 Myr). Using a fiducial linking length of 1 pc, we only consider groups with more than 100 SPH particles, i.e. more massive than

$\sim 400\,M_\odot$. We term such dense, cold, and coherent structures "cold clouds".

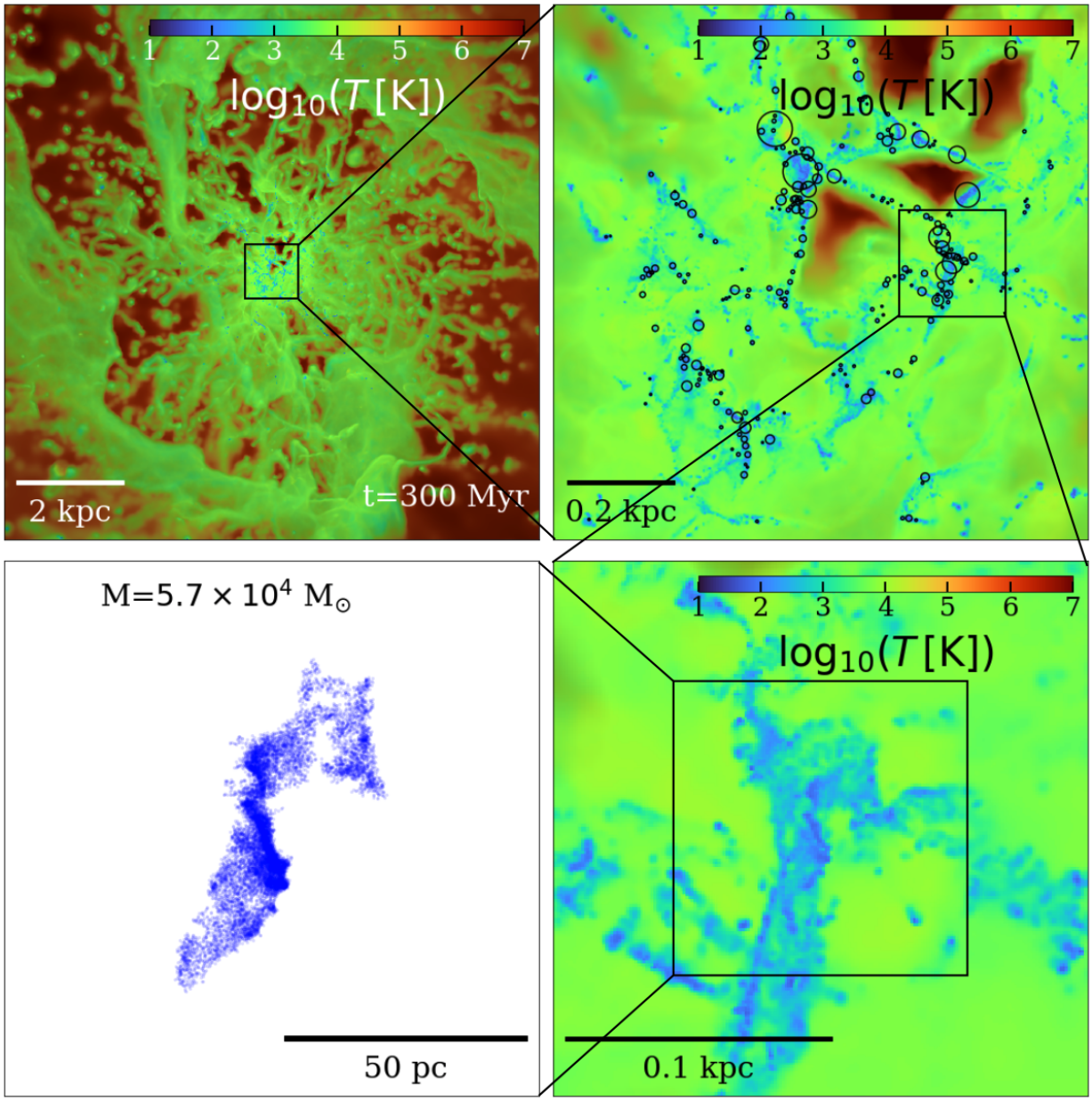

Figure 4.1: Zoom sequence (top left, top right, bottom right, bottom left) of the gas distribution colour-coded by the mass weighted temperature (first three panels) of the simulation at 300 Myr (right panel in Fig. 3.1) from 10 kpc down to 100 pc with one of the most massive cold clouds in the system ($5.7 \times 10^4\,M_\odot$). The black circles in the top right panel indicate the positions and sizes of individual cold clouds identified with a FoF algorithm. In the bottom right panel we show a zoom onto a massive cloud with its environment and the raw particle distribution identified by FoF is shown in the bottom left panel. The highly irregular shape with density substructure is typical for the massive cold clouds in the simulation.

Typically we identify hundreds of clouds at every simulation snapshot. An example of the cloud identification process is shown in Fig. 4.1 for the merger system at $t_{\rm sim}$ = 300 Myr (e.g. the right panels in Fig. 3.1). The top left panel shows the large scale gas distribution colour-coded by temperature on a 10 kpc scale. A zoom into the central kiloparsec makes the filamentary cold cloud structure visible (blue regions, top right panel). Black circles represent an identified cold cloud (FoF group) and the maximum spatial extent of the clouds is indicated by the size of the circles. A zoom into the region of one of the most massive clouds in this snapshot (bottom right panel) on a 200 pc scale depicts the typical highly irregular structure of the cold gas (blue). In the bottom left panel we show the underlying SPH particle distribution of the identified cloud with a mass of $M = 5.7 \times 10^4\,{\rm M}_\odot$. The substructure within the clouds with several dense sub-clumps becomes visible in this representation. This zoom sequence from 10 kpc down to 50 pc showcases the large dynamic range covered by the simulation.

A gallery of the morphology of the eight most massive cold clouds identified in the same snapshot at $t_{\rm sim}$ = 300 Myr of our simulation is presented in Fig. 4.2. The visualisation of the SPH particle distribution using the mass distribution as a colormap highlights the variations in shape and substructure. At this snapshot the clouds can become as massive as $9.5 \times 10^4\,{\rm M}_\odot$. The most massive cloud identified in the entire simulation has a mass of $3.9 \times 10^5\,{\rm M}_\odot$ at 156 Myr. The cloud shown in Fig. 4.1 is the third most massive cloud in this simulation snapshot. At the massive end the clouds are typically elongated with sizes up to several tens or hundred parsec and show density substructure. In the different panels each cloud is centred to its densest region.

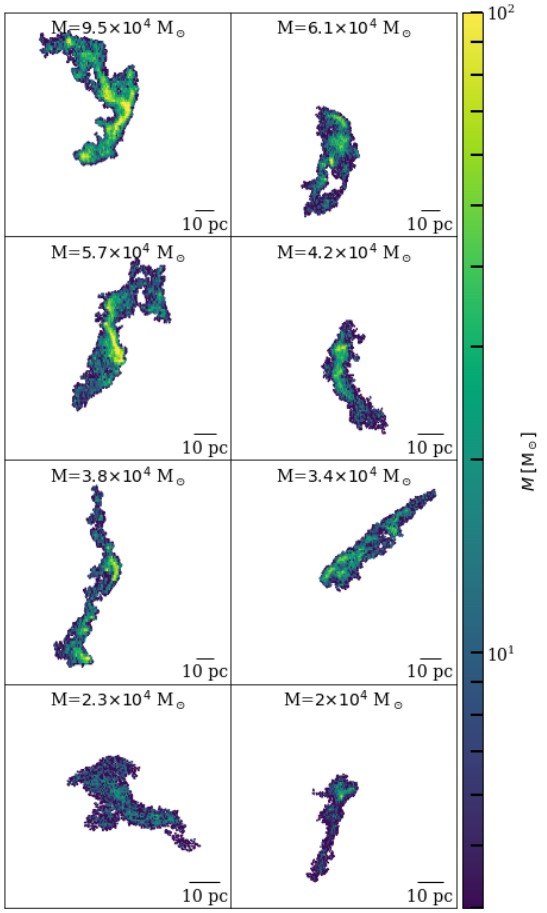

Figure 4.2: Visualisation of the FoF identified SPH gas particle distribution of the eight most massive cold clouds at 300 Myr. Each cloud is centred to its respective densest region. The massive cold clouds typically have filamentary and irregular shapes with density substructure. The colormap indicates the mass distribution of each cloud, from low mass areas in blue to high mass areas in yellow.

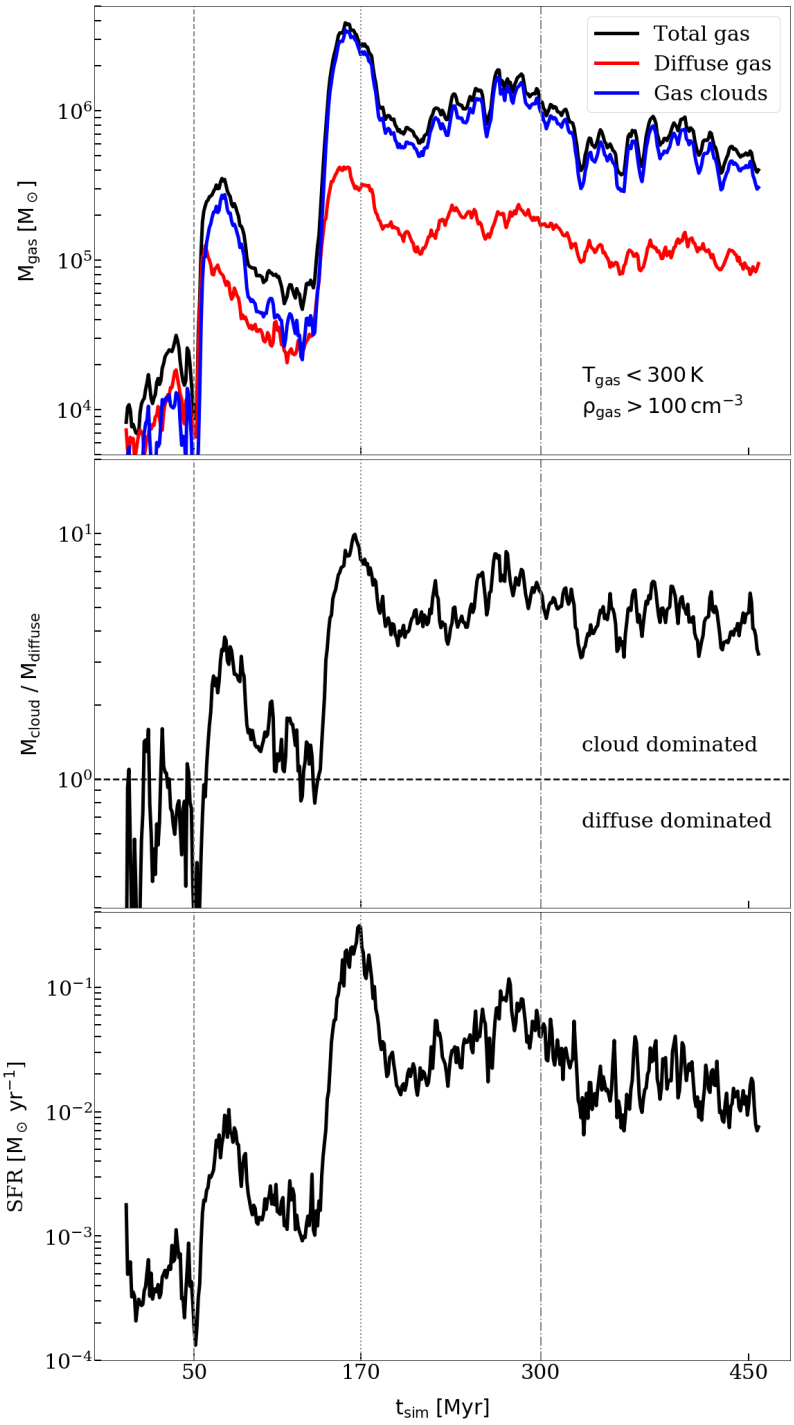

Figure 4.3: *Top panel:* Time evolution of the total mass in cold and dense gas ($T_{gas} < 300\,K$ and $\rho_{gas} > 100\,cm^{-3}$, black) split up into clouds ($T_{cl} < 300\,K$ and $\rho_{cl} > 100\,cm^{-3}$, blue) and the component not bound in clouds, i.e. the diffuse gas ($T_{diff} < 300\,K$ and $\rho_{diff} > 100\,cm^{-3}$, red). The time of the first encounter at 50 Myr, the second encounter at 170 Myr and the relaxed state at 300 Myr are indicated by dashed, dotted and dashed-dotted lines, respectively. The mass in cold gas strongly increases around the peak starburst. *Middle panel:* The mass ratio of cold clouds and cold diffuse gas. Unity is indicated by the horizontal line. The starburst drives the cold medium, which is initially dominated by diffuse gas, into a new equilibrium where the mass of the cold gas bound in clouds is now about four times the mass of the diffuse gas. *Bottom panel:* Star formation rate (SFR) as a function of time. The interaction increases the star formation rate by about two orders of magnitude and drives the system into an extended starburst. The star formation rate evolution is qualitatively similar to the mass evolution of cold gas in clouds (see top and middle panel).

With the results of the cloud analysis at hand we can now investigate the time evolution of the cold gas component for the full simulation as shown in Fig. 4.3. In the top panel we show the time evolution of the cold gas component (black), separated into a cloud (blue) and diffuse (no-cloud, red) component. The mass in cold gas is low ($\sim 10^4\,\mathrm{M}_\odot$) and dominated by diffuse gas at the beginning of the simulation. This is only ~ 0.1 per cent of the total $\sim 10^7\,\mathrm{M}_\odot$ of gas in the two merging galaxies. Already after the first encounter (vertical dashed line) the gas is compressed and the cold gas mass increases by about one order of magnitude. Now the cold phase ISM becomes dominated by clouds as can also be seen in the middle panel of Fig. 4.3. The effect becomes even stronger after the second encounter (vertical dotted line). The cold gas mass reaches $\sim 10^6\,\mathrm{M}_\odot$ and the cold ISM is now predominantly in a structured clumpy phase and stays like this until the end of the simulation. The evolution of the cold gas faction in clouds closely follows the star formation rate of the system (bottom panel in Fig. 4.3). As soon as the system enters its starburst phase, with a more than a factor of ten elevated star formation rates, the cold ISM changes its phase structure from being dominated by unbound gas to being cloud dominated. The starburst drives the cold medium into a new equilibrium where the mass of the cold gas bound in clouds is now about four times the mass of the diffuse gas.

4.2 Cold cloud mass and size functions

In Fig. 4.4 we present the simulated cold cloud mass function ranging from the minimum mass of $\sim 400\,\mathrm{M}_\odot$ to $\sim 4\times10^5\,\mathrm{M}_\odot$ at the peak of star formation at 170 Myr (top panel) and at a later phase of the system at 300 Myr (bottom panel, see Fig. 3.1 for the corresponding global gas distributions).

We compare the cloud mass functions at four different upper limits for the cold gas density. In addition to our fiducial value of $\rho_{\mathrm{gas}} = 100\,\mathrm{cm}^{-3}$ (blue) we also perform the FoF analysis for cold gas denser than $\rho_{\mathrm{gas}} = 500\,\mathrm{cm}^{-3}$ (orange), $\rho_{\mathrm{gas}} = 1000\,\mathrm{cm}^{-3}$ (green), and $\rho_{\mathrm{gas}} = 2000\,\mathrm{cm}^{-3}$ (red). For all density thresholds, the cold cloud mass functions follow similar $dN/dM \propto M^\alpha$ power law distributions with slopes in the range of $-1.9 \lesssim \alpha \lesssim -1.6$. As expected, the normalisation decreases with increasing density thresholds. The slopes of the cold cloud mass functions are comparable to observational values $\alpha \sim -1.8$ for molecular cloud mass functions inferred from the CO luminosity function (e.g. Heyer et al., 2001). The similar slopes for denser substructures indicate a self-similar density structure within the clouds.

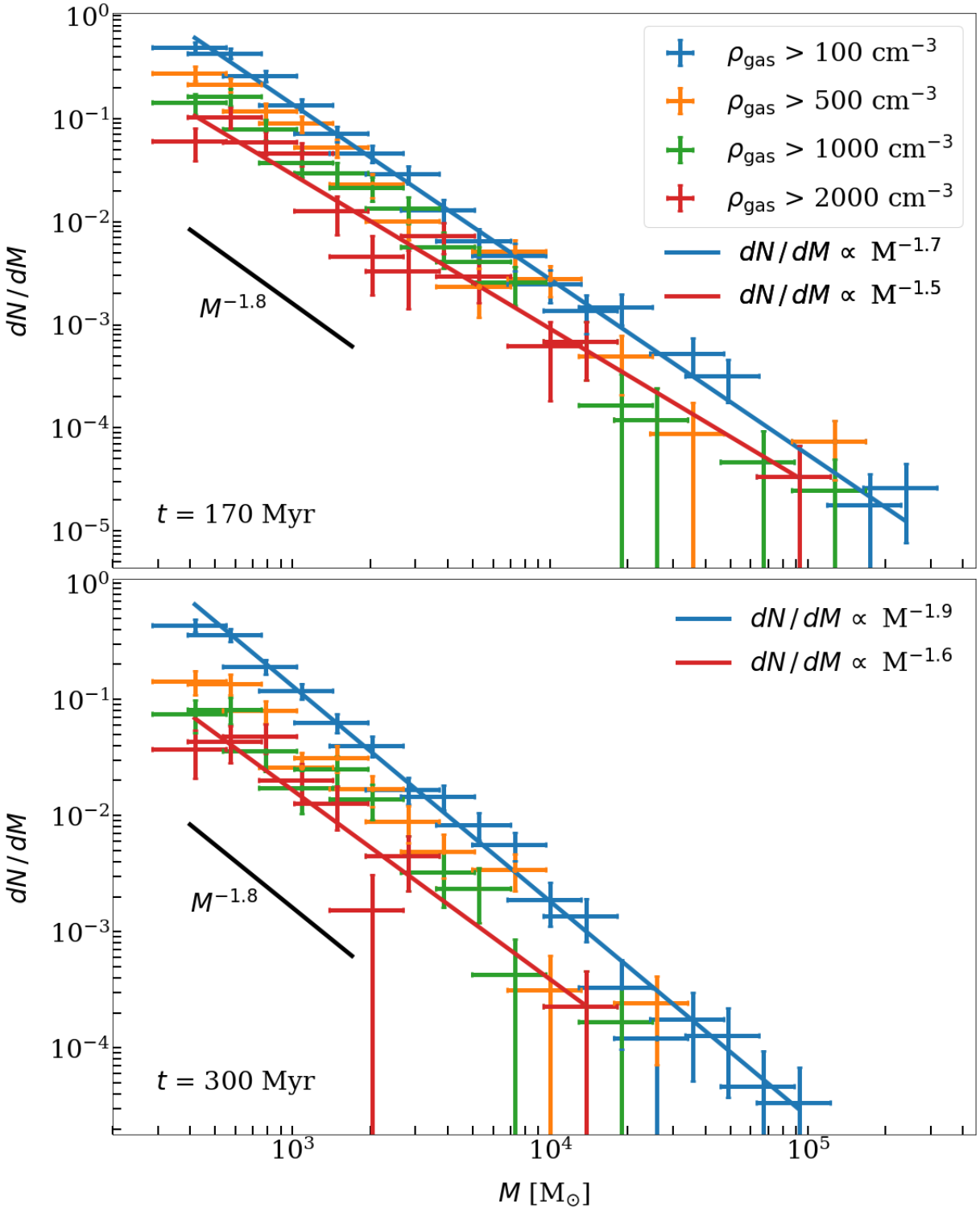

Figure 4.4: Mass function of cold ($T < 300$K) clouds at 170 Myr (top panel) and 300 Myr (bottom panel) and increasing density cuts from $\rho > 100\,\mathrm{cm}^{-3}$ to $\rho > 2000\,\mathrm{cm}^{-3}$ shown in blue, orange, green, and red, respectively. The cloud mass function follows a power law $dN/dM \propto M^{-\alpha}$ at all densities, indicating self-similar structure. The power law slope for these two snapshots ranges between $-1.6 \lesssim \alpha \lesssim -1.8$. A typical observational estimate of $dN/dM \propto M^{-1.8}$ from CO is shown by the black line (Heyer et al., 2001).

The time evolution of the cold cloud mass function for the full simulation is shown in Fig. 4.5 in steps of 10 Myr.

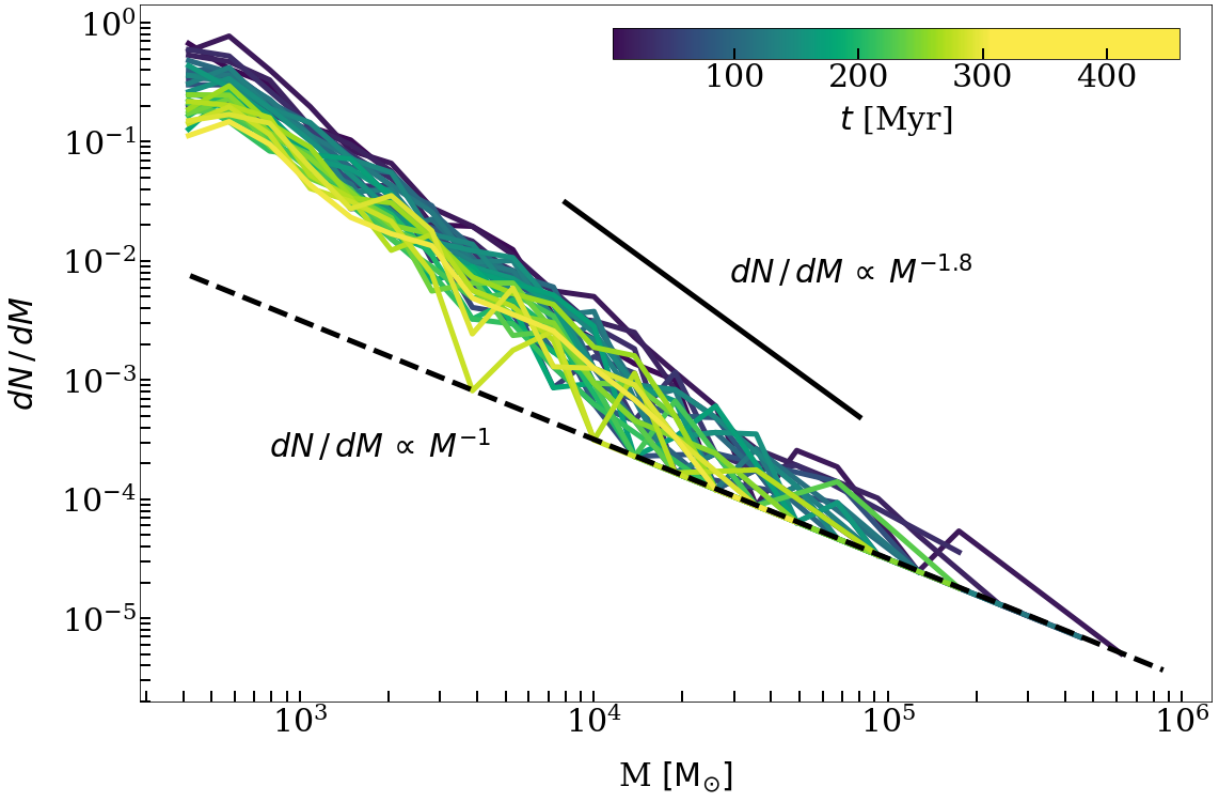

Figure 4.5: Time evolution of the cold cloud mass function from pre-merger times (dark blue) towards the new post-merger equilibrium (yellow) plotted every 10 Myr. At all phases the mass function follows a power-law distribution. For comparison we indicate by the black line ($dN/dM \propto M^{-1.8}$) the observed slope from CO from (Heyer et al., 2001). The dotted line ($dN/dM \propto M^{-1}$) indicates the one cloud per mass bin threshold.

From the early pre-merger stages of the simulation (dark blue) towards the late post-merger equilibrium (yellow) the mass function approximately follows a power-law distribution $dN/dM \propto M^{\alpha}$ at every stage. The limiting minimum slope $\alpha = -1$ for one cloud per mass bin is indicated by the black dashed line in Fig. 4.6. The slope of the cold cloud mass function is in agreement with the observed CO luminosity function slope by (Heyer et al., 2001) (solid black line, see also Fig. 4.5). In order to calculate the correlation between the slope and the normalisation of the CMF in Fig. 4.6 we need a measure of linear correlation between variables. For this purpose we use the Pearson correlation coefficient ρ that is defined as the ratio between the covariance of two variables X, Y and the product of their standard deviations σ_X, σ_Y, i.e. $\rho(X,Y) = \frac{\mathrm{cov}(X,Y)}{\sigma_X \sigma_Y}$. Calculating the Pearson correlation coefficient for the slope α and the normalisation β of the

logarithmic fits performed on the CMFs of Fig. 4.6 we find that $\rho(\alpha, \beta) = -0.86$ suggesting that the slope and the normalisation are strongly anti-correlated. For over more than 300 Myr of simulated time, the best fitting slope of the cloud mass function varies little (see Fig. 4.6). The mean value is $\alpha \sim -1.8$ with a scatter of ~ 0.1 dex. Using again the Pearson correlation coefficient we find that $\rho(\alpha, \mathrm{SFR}) = 0.3$ suggesting that there is an insignificant correlation between the slope of the CMF α and the SFR. The coefficient between the normalisation of the CMF β and the SFR is $\rho(\beta, \mathrm{SFR}) = 0.2$ suggesting that the correlation between the normalisation and the SFR is negligible. However, the mass of the most massive cloud identified in each snapshot between 150 Myr and 458 Myr correlates strongly with the SFR with $\rho(M_{\mathrm{max}}, \mathrm{SFR}) = 0.8$.

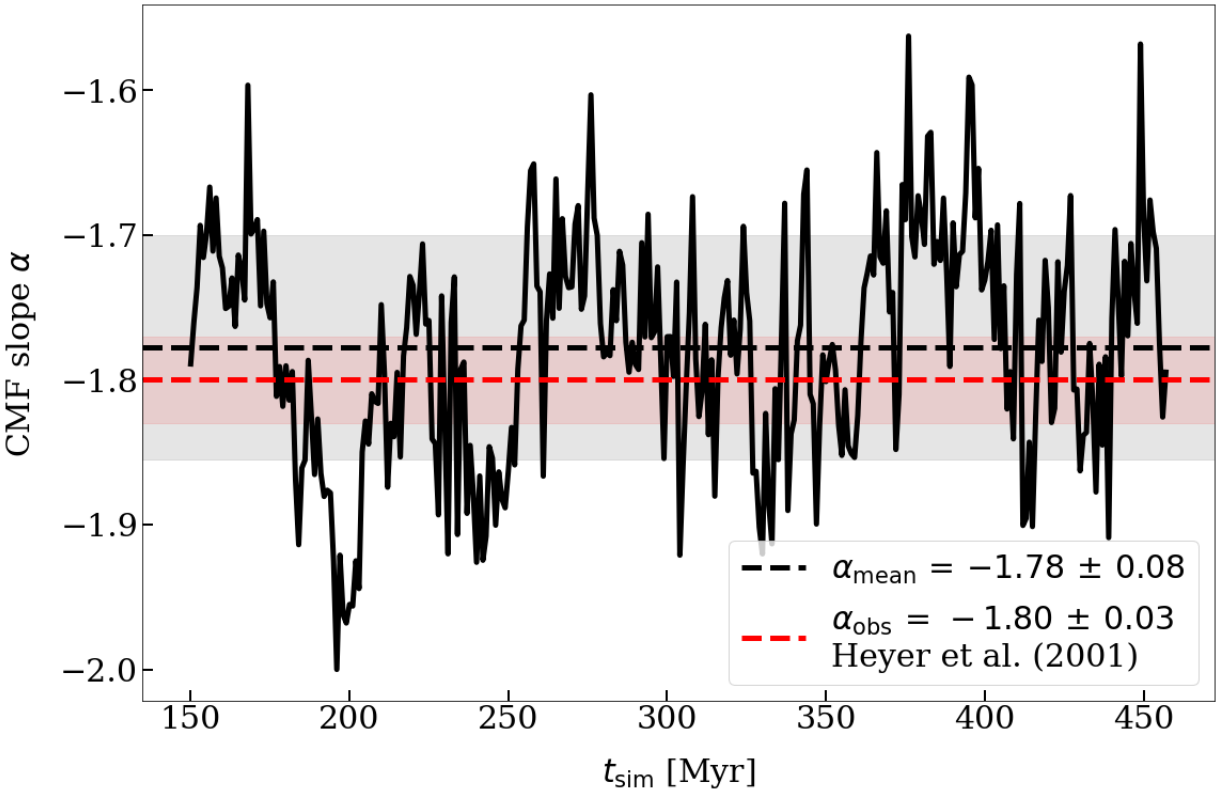

Figure 4.6: Time evolution of the power law slope α of the cold cloud mass functions shown in Fig. 4.5 starting at 150 Myr (i.e. shortly before the starburst). The mean value of the slope is indicated by the black horizontal dashed line ($\alpha_{\mathrm{mean}} = -1.78$) and the scatter of 1 σ($\pm$0.08) is indicated by the grey area. The value of the observational slope of the CO luminosity function ($\Delta N/\Delta L_{\mathrm{CO}} \propto L_{\mathrm{CO}}^{\alpha}$) is indicated by the red horizontal dashed line ($\alpha_{\mathrm{obs}} = -1.8$) and the observational scatter ($\pm$0.03) is indicated by the red area (Heyer et al., 2001). The mass function slope is similar to the observational at all stages of the simulation.

Working in a similar way as we did for the mass distribution in Figs. 4.4 and 4.5, we plot the cloud size function of the clouds at 170 Myr (top panel) and 300 Myr (bottom panel) in Fig. 4.7. Like the cloud mass function (CMF), the cloud size function is defined as the number of clouds in a specific size range divided by that range, i.e. $dN/dR_{1/2}$, plotted against the size $R_{1/2}$. As a measure for the cloud size we use the projected half mass radius $R_{1/2}$. The sizes of the simulated cold clouds range from a few parsec to $\sim$ 50 pc. The cloud size function follows a power-law distribution $dN/dR_{1/2} \propto R_{1/2}^{\alpha}$ with a typical index of $\alpha = -2.5$. This is in good agreement with the observations of Heyer et al. (2001) where the slope is $\alpha_{\rm obs} = -3.2(\pm 0.1)$. The vertical dotted line indicates the 3 pc size threshold that was the observation limit for Heyer et al. (2001). To carry out a more in-depth comparison between our results and the observations, we only use clouds with $R_{1/2} > 3$ pc for the analysis, but we display the full range of our sample in Fig. 4.7.

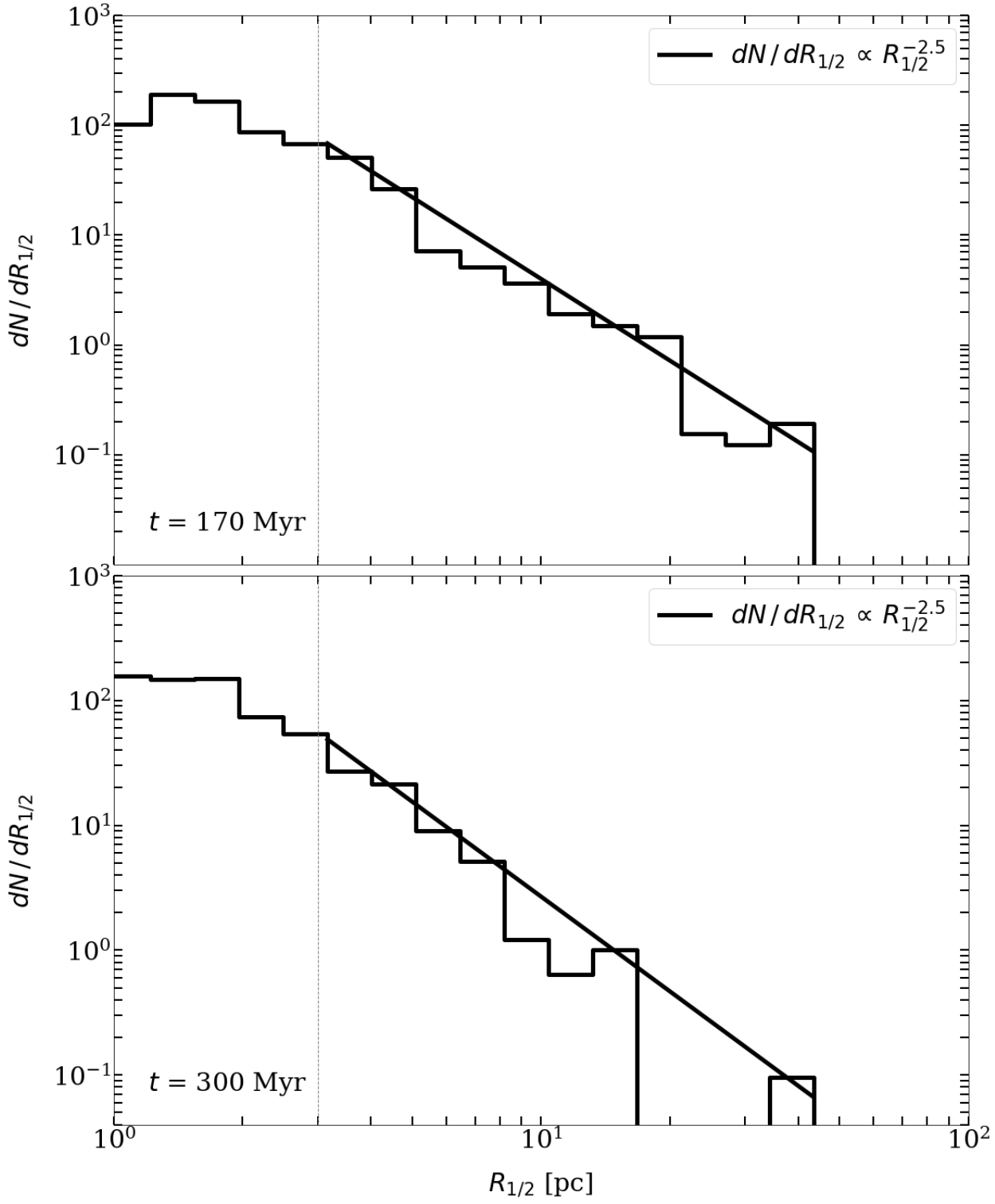

Figure 4.7: Differential size distribution of the cold clouds detected at 170 Myr (top panel) and at 300 Myr (bottom panel). The size of the clouds is represented by the projected half mass radius $R_{1/2}$. The differential size distribution of the clouds is a power law distribution with index -2.5 well in agreement with observations, e.g. Heyer et al. (2001) with $dN/dR_{1/2} \propto R_{1/2}^{-3.2(\pm 0.1)}$. The horizontal dotted line indicates the observational limit of Heyer et al. (2001) at $R_{1/2} \sim 3$ pc.

4.3 Scaling relations

The cold cloud scaling relations introduced by Larson (1981) can be understood as an indication that cold clouds are self-gravitating and, possibly, in some form virial equilibrium (see e.g. review by Heyer & Dame, 2015). The virial mass $M_{\rm vir}$ estimate and the actual mass $M_{\rm cc}$ of a cloud with an effective (half-mass) radius $R_{1/2}$, an effective surface mass density $\Sigma_{1/2}$, and a one dimensional line-of-sight velocity dispersion σ_v are:

$$M_{\rm vir} = 5 \times \frac{{\sigma_v}^2 R_{1/2}}{G} \text{ and } M_{\rm cc} = \pi \, \Sigma_{1/2} \, R_{1/2}^2, \tag{4.1}$$

respectively.

For clouds in virial equilibrium $\alpha_{\rm vir} = M_{\rm vir}/M_{\rm cc} = 1$ and from equation 4.1 we have:

$$\sigma_v = \sqrt{\frac{\pi G}{5}} \, R_{1/2}^{0.5} \, \Sigma_{1/2}^{0.5}. \tag{4.2}$$

For a constant effective mass surface density $\Sigma_{1/2} \sim$ const., equation 4.2 implies a scaling of the velocity dispersion with the square-root of the radius (see e.g. Heyer & Dame, 2015). In this case, the value of 0.5 of the power law index for the first Larson relation reported by Solomon et al. (1987) and Heyer & Dame (2015) is consistent with the assumption that the clouds are close to virial equilibrium (see equation 4.2).

In Fig. 4.8 we show the first Larson relation for the clouds identified in the simulations with our fiducial density and temperature thresholds. The three one-dimensional line-of-sight velocity dispersion values for each cloud are computed from the mass weighted gas particle velocities along the x-, y-, and z-axis of the computational domain (i.e. the simulation seen from three directions), respectively. The half mass radius is the projected radius enclosing half of the cloud mass from the densest region of the cloud. We show this relation at the previously discussed two characteristic times right after the starburst at 170 Myr (top panel) and at 300 Myr (bottom panel) when the system has reached post-merger equilibrium. The best fitting relation for clouds larger than 3 pc is indicated by the black line. For comparison we show the canonical relation derived in Solomon et al. (1987) and discussed in the review by Heyer & Dame (2015). The observed slope ($\alpha_{\rm obs} = 0.5$) and the fitted slopes ($\alpha_{\rm sim\ 170\ Myr} = 0.34$ and $\alpha_{\rm obs\ 300\ Myr} = 0.32$) agree. The scatter is of order ~ 0.3 dex in both cases. This indicates that the cold cloud structure in our simulation model has similar properties than observed cold clouds.
In Fig. 4.9 we show the relation described in equation 4.2 at the times of 170 Myr (main starburst) and 300 Myr (post-starburst equilibrium). The velocity dispersion $\sigma_{\rm v}$ is calculated in the line-of-sight. Therefore, we have a set of three one-dimensional line-of-sight velocity dispersion values for each cloud, as in Fig. 4.8: $\sigma_{\rm x}$ (black), $\sigma_{\rm y}$ (light blue) and $\sigma_{\rm z}$ (orange). The size of the

identified cold clouds in terms of the projected half-mass-radius $R_{1/2}$, as in Fig. 4.8. The empty circles represent clouds with sizes $R_{1/2} \leq 3$ pc, which is the detection threshold for Heyer et al. (2001), whereas the filled circles represent clouds with $R_{1/2} > 3$ pc. The solid, dashed and dotted lines indicate virial parameters of 1, 3, and 10, respectively, assuming a virial constant of 5 (see equation 4.1).

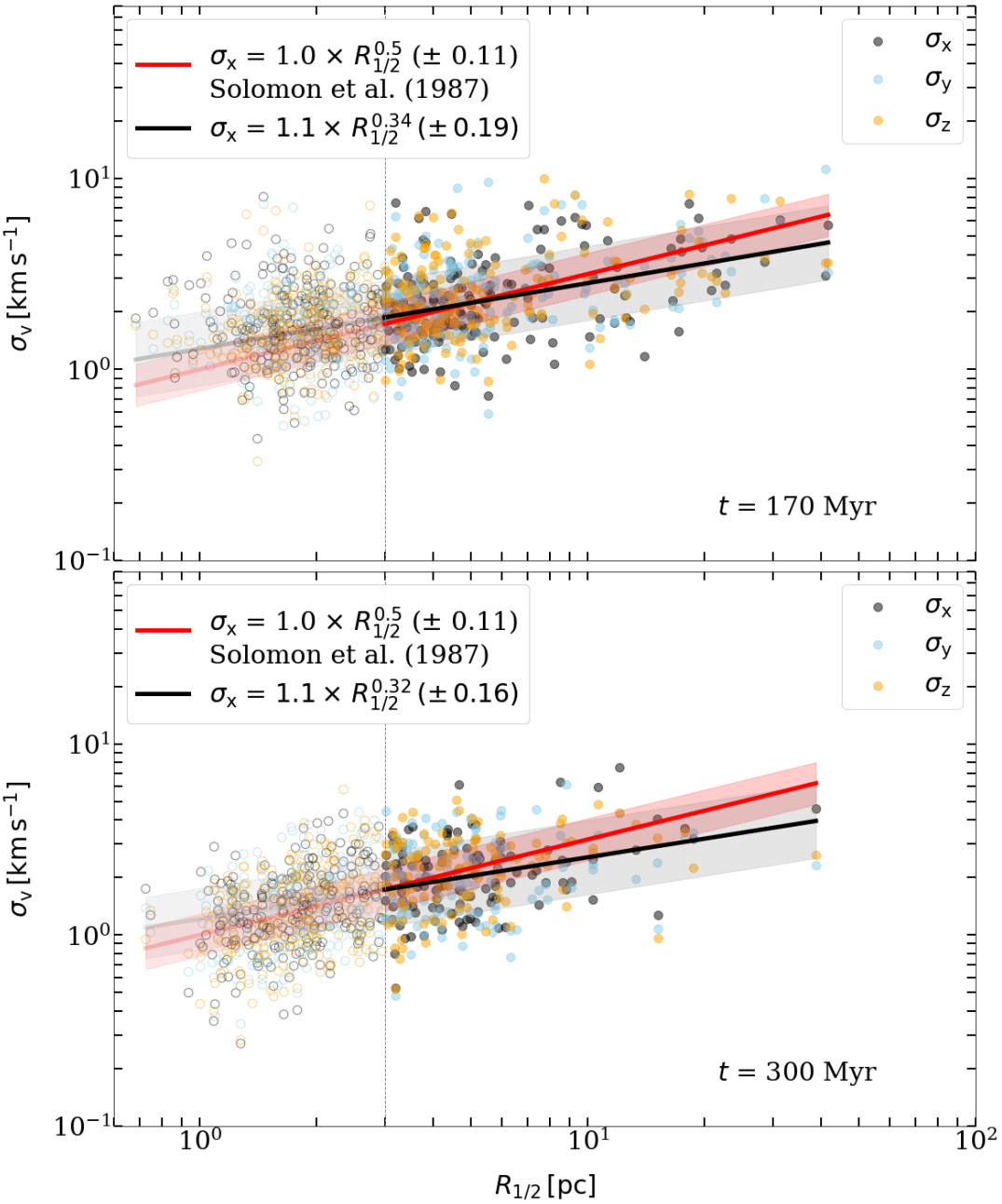

Figure 4.8: Line-of-sight velocity dispersion σ_v in the: x-direction (σ_x, black), y-direction (σ_y, light blue) and z-direction (σ_z, orange) vs. the size of the identified cold clouds in terms of the projected half-mass-radius $R_{1/2}$ at 170 Myr (top panel) and 300 Myr (bottom panel). The vertical dashed line marks the 3 pc size threshold which is the detection threshold for Heyer et al. (2001). The empty circles represent clouds with $R_{1/2} \leq 3$ pc, whereas the filled circles represent clouds with $R_{1/2} > 3$ pc. The solid red line shows the best-fit to the Solomon et al. (1987) points and the shaded red area represents the scatter. The solid black line represents the best fit to the simulation data while the shaded black area denotes the standard deviation of the cloud distribution with sizes larger than 3 pc. All of the aforementioned fittings have been performed on clouds larger than 3 pc, i.e. $R_{1/2} > 3$ pc.

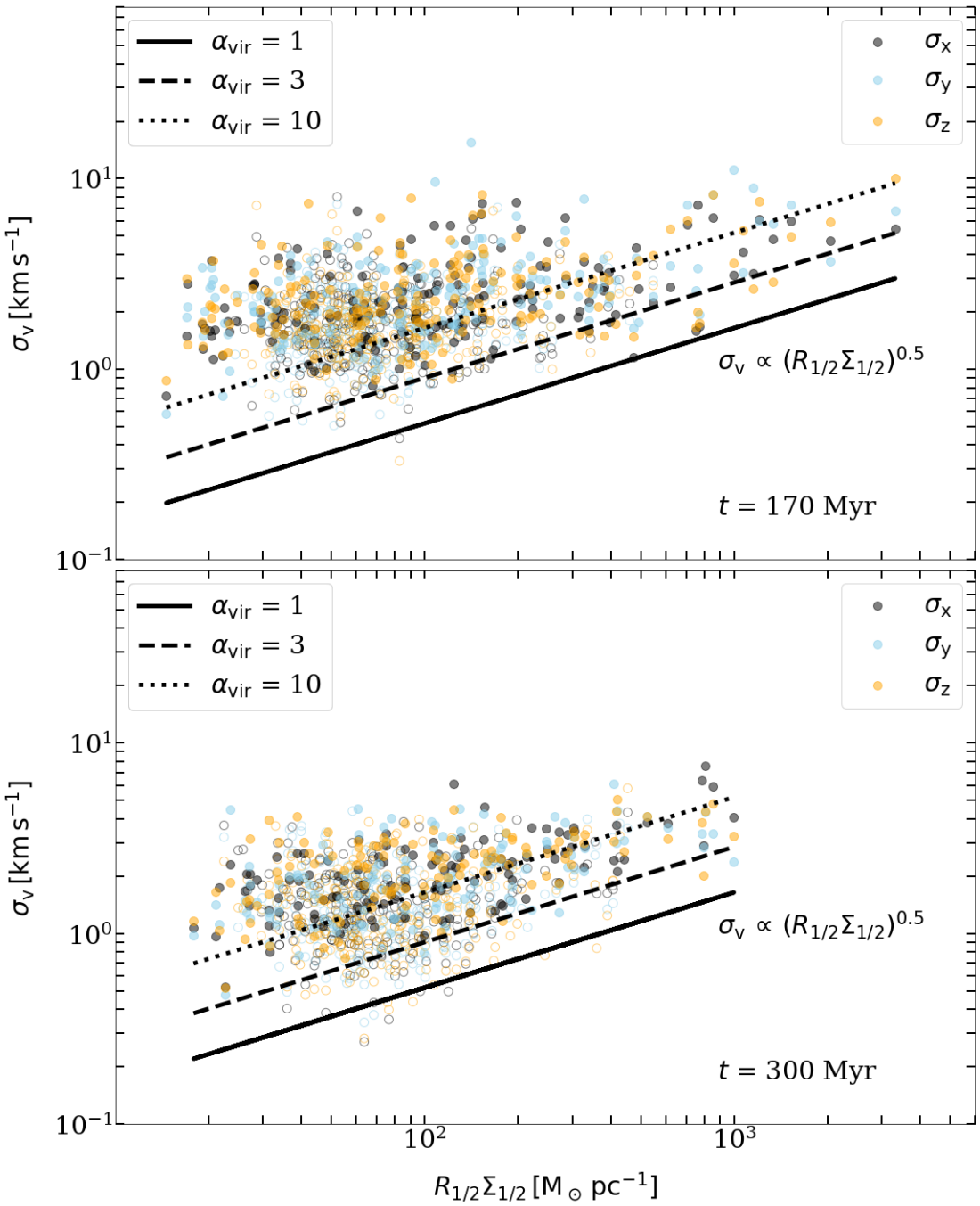

Figure 4.9: Line-of-sight velocity dispersion σ_v in the: x-direction (σ_x, black), y-direction (σ_y, light blue) and z-direction (σ_z, orange) vs. the product of the size of the identified cold clouds in terms of the projected half-mass-radius $R_{1/2}$ and the effective surface density $\Sigma_{1/2}$ at 170 Myr (top panel) and 300 Myr (bottom panel). The empty circles represent clouds with $R_{1/2} \leq 3$ pc, whereas the filled circles represent clouds with $R_{1/2} > 3$ pc. The solid line represents equation 4.2 for virial parameter $\alpha_{vir} = 1$. The dashed line is derived from equation 4.1 for $\alpha_{vir} = 3$ and the dotted line for $\alpha_{vir} = 10$. As in Fig. 4.8, all fittings have been performed on clouds larger than 3 pc.

4.4 Cold cloud life cycle

As we explained in section 1.1.6, cold clouds are destroyed by stellar feedback thus having lifetimes in the range of 10-30 Myr and within ~ 5 Myr after the emergence of very massive stars (Chevance et al., 2020, 2022). To extract the cold cloud life-cycle of in our simulation we have identified the cold clouds analysed in each snapshot as a FoF group (see section 2).

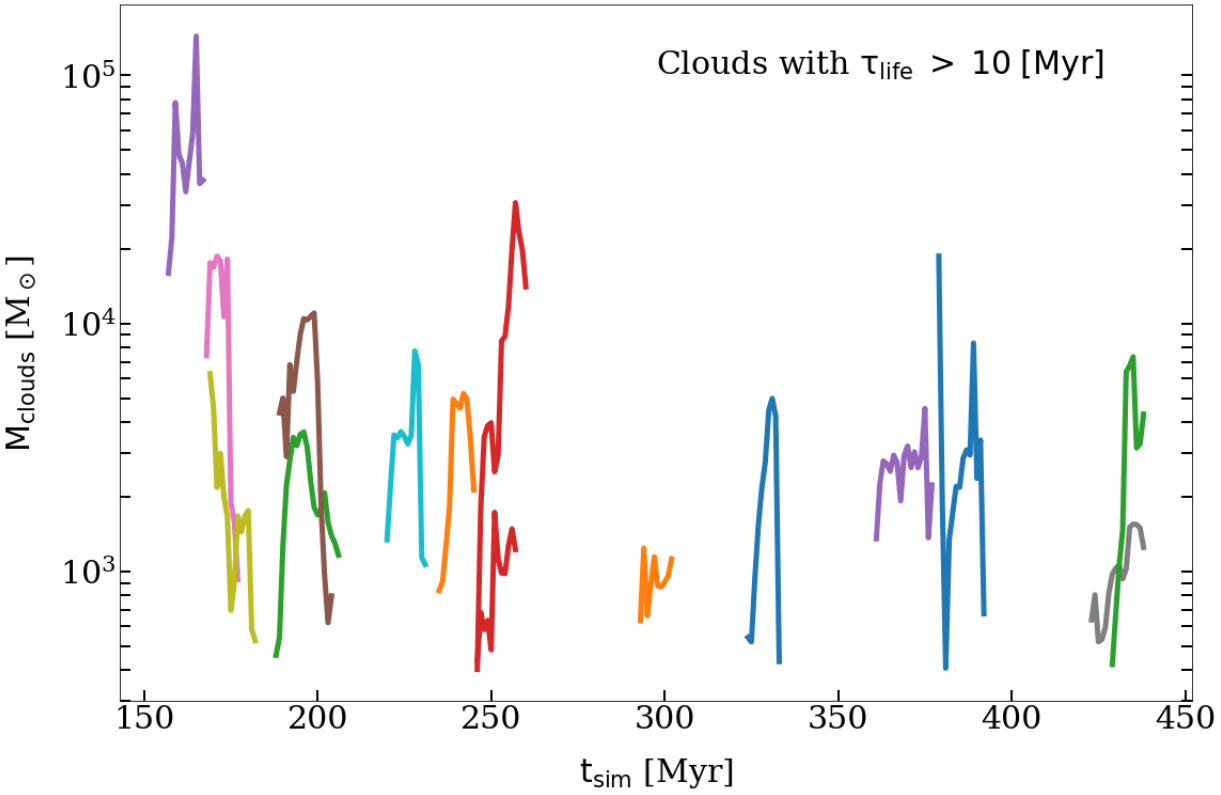

Figure 4.10: Mass evolution of 15 cold clouds, randomly selected from our sample of traced clouds, with lifetimes higher than 10 Myr. In their growth phase the clouds gain enough mass for gravitational collapse and the beginning of star formation. In their destruction phase the energy and momentum input from newly formed stars lead to the dispersal of the clouds. Both the growth and destruction phases of the clouds are visible on the selected mass traces.

In total we have followed 31222 tracks from individual clouds beginning shortly before the peak starburst (150 Myr) until the end of our simulation (457 Myr). 61 per cent of the followed tracks (i.e 19123 traced cold clouds) have lifetimes longer than 1 Myr. 91 per cent of the clouds that survive for more than 1 Myr have lifetimes shorter than 10 Myr and no cloud lives longer than ~ 30 Myr. As an example, we show the mass evolution of 15 randomly chosen clouds with lifetimes longer than 10 Myr is shown in Fig. 4.10. Star formation occurs in dense regions

inside molecular clouds. The conditions under which these regions collapse are determined by the interplay between two opposing forces: gravity and thermal pressure. After accumulating enough mass from the ambient medium some of these regions within the clouds will reach sufficiently high densities for the Jeans instability to kick in. This characteristic mass growth phase is visible in Fig. 4.10. The beginning of star formation marks a critical point in the evolution of the clouds. As more and more stars are created from the initial cloud, the mass of the cold gas drops and the feedback from these young stars will eventually disperse the cloud. This destruction phase in the cloud life-cycle marked by a continuous drop in the mass of the cold gas is visible in Fig. 4.10.

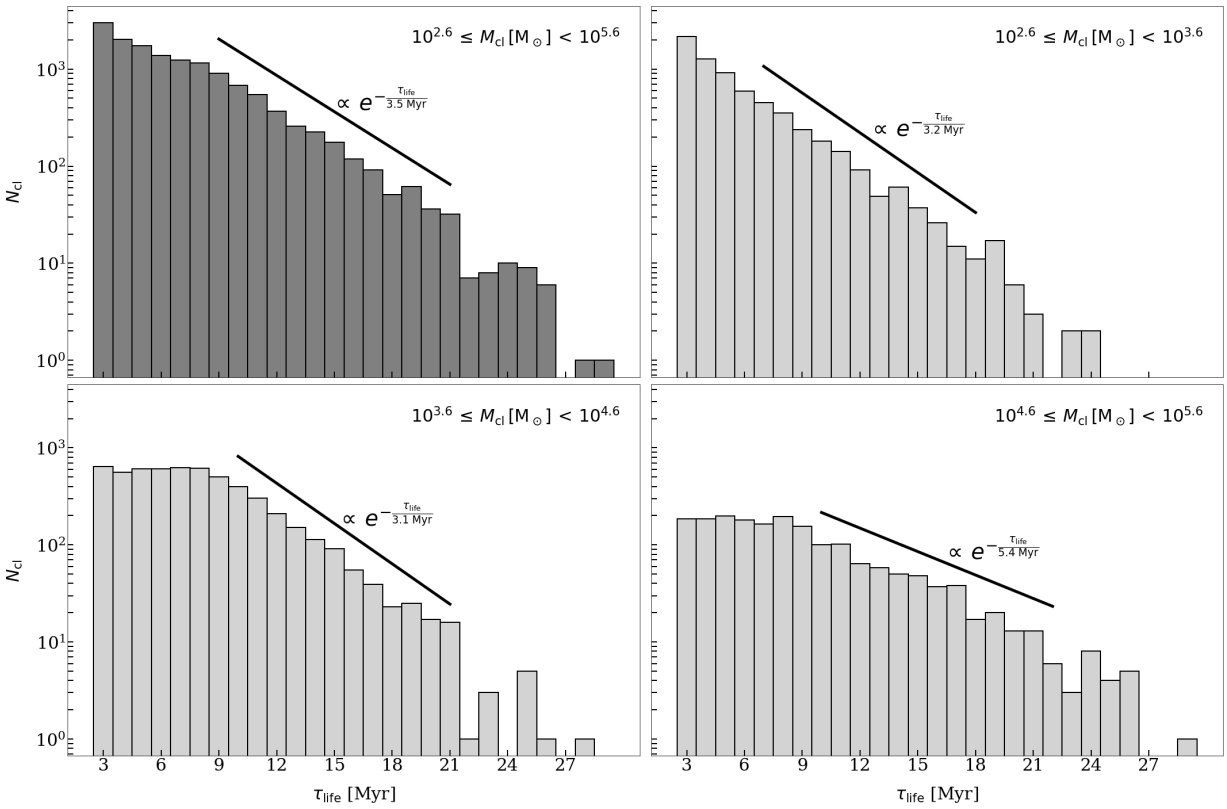

Figure 4.11: *Top left*: Histogram of the lifetimes of the total number of cold clouds that survived for at least 3 Myr traced in our simulation, i.e. in the mass range $10^{2.6} \leq M_{\rm cl}\,[{\rm M}_\odot] < 10^{5.6}$. The e-folding timescale is 3.5 Myr. *Top right*: Histogram of the cold clouds traced in the mass range $10^{2.6} \leq M_{\rm cl}\,[{\rm M}_\odot] < 10^{3.6}$ with e-folding timescale 3.2 Myr. *Bottom left*: Histogram of the cold clouds traced in the mass range $10^{3.6} \leq M_{\rm cl}\,[{\rm M}_\odot] < 10^{4.6}$ with e-folding timescale 3.1 Myr. *Bottom right*: Histogram of the cold clouds traced in the mass range $10^{4.6} \leq M_{\rm cl}\,[{\rm M}_\odot] < 10^{5.6}$ with e-folding timescale 5.4 Myr.

In Fig. 4.11 we show the lifetime distribution of all traced cold clouds that survived for at least 3 Myr (top left panel) as well as the distribution in three different mass bins covering the mass range of identified clouds, i.e. in mass bins of $10^{2.6}\,\mathrm{M}_{\odot} \lesssim M_{\mathrm{cl}} < 10^{3.6}\,\mathrm{M}_{\odot}$ (top right panel), $10^{3.6}\,\mathrm{M}_{\odot} \lesssim M_{\mathrm{cl}} < 10^{4.6}\,\mathrm{M}_{\odot}$ (bottom left panel), and $10^{4.6}\mathrm{M}_{\odot} \lesssim M_{\mathrm{cl}} < 10^{5.6}\,\mathrm{M}_{\odot}$ (bottom right panel). In general, the cold clouds follow an exponential lifetime distribution with an e-folding timescale of ~ 3.5 Myr. In the mass range of $10^{2.6}\,\mathrm{M}_{\odot} \lesssim M_{\mathrm{cl}} < 10^{3.6}\,\mathrm{M}_{\odot}$ the e-folding timescale is ~ 3.2 Myr, in the mass range $10^{3.6}\,\mathrm{M}_{\odot} \lesssim M_{\mathrm{cl}} < 10^{4.6}\,\mathrm{M}_{\odot}$ the e-folding timescale is ~ 3.1 Myr and on the high mass end of $10^{4.6}\mathrm{M}_{\odot} \lesssim M_{\mathrm{cl}} < 10^{5.6}\,\mathrm{M}_{\odot}$ the e-folding timescale is ~ 5.4 Myr. There is a moderate trend for lower and medium mass clouds to have a shorter e-folding timescale whereas more massive clouds have slightly longer typical lifetimes.

To quantify this and check if the trend holds, we make a finer binning of the cold cloud masses in our sample and we calculate the average lifetime of the clouds in each mass bin $\overline{\tau}_{\mathrm{life}}$. As a representative value of the masses we choose the peak mass that each cloud reaches during its lifetime M_{max} and for the binning we use 20 logarithmic bins. The results of our analysis are shown in Fig. 4.12. Each scatter point in Fig. 4.12 represents each mass bin and the error-bars indicate the errors on the x-y plane of the plot. In the x-axis we use the width of each logarithmic bin as the respective x-error and the in the y-axis we use the standard error of the average value of the lifetimes $\overline{\tau}_{\mathrm{life}}$ in each bin. Approximating the slope of the power-law distributions that fit the low mass range in our sample (i.e. clouds with peak masses $M_{\mathrm{max}} < 10^4\,\mathrm{M}_{\odot}$) we find that there is a power-law dependency between the peak mass M_{max} and the average lifetime $\overline{\tau}_{\mathrm{life}}$ such that $\overline{\tau}_{\mathrm{life}} \propto M_{\mathrm{max}}^{0.3}$. This dependency indicates that the cold clouds in the lower mass end of our sample have longer lifetimes the more massive they are. For the higher mass range in our sample (i.e. clouds with peak sizes $M_{\mathrm{max}} > 10^4\,\mathrm{M}_{\odot}$ we have that $\overline{\tau}_{\mathrm{life}} \propto M_{\mathrm{max}}^{0.05}$. This indicates that the more massive cold clouds in our sample have slight differences between their average lifetimes which tend to stabilise around 8 Myr.

Working as in Fig. 4.12, we perform a logarithmic binning of the sizes of the traced cold clouds. As a measure of size, we use the maximum distance that a SPH particle belonging to the cloud has from the centre of mass of the cloud. As a representative size value for the binning we chose the size each cloud has when it reaches its peak mass $R_{\mathrm{M_{max}}}$ and we calculate the average lifetime of the clouds in each size bin $\overline{\tau}_{\mathrm{life}}$ (we work with 20 logarithmic bins as in Fig. 4.12). The results are shown in Fig. 4.13. Each scatter point represents each size bin. The error in the x-axis is represented by the horizontal error bars which are drawn based on the width of each logarithmic bin. For the error in the y-axis we use the standard error of the average value of the lifetimes $\overline{\tau}_{\mathrm{life}}$ in each bin which is visualised by the vertical error bars. As in Fig. 4.12, we approximate the slope of the power-law distributions that fit the smaller size range in our sample (i.e. clouds with sizes at peak mass $R_{\mathrm{M_{max}}} < 20$ pc) and we find a power-law dependency between the size at peak mass $R_{\mathrm{M_{max}}}$ and the average lifetime $\overline{\tau}_{\mathrm{life}}$, i.e. $\overline{\tau}_{\mathrm{life}} \propto R_{\mathrm{M_{max}}}^{0.3}$. This dependency indicates that in the

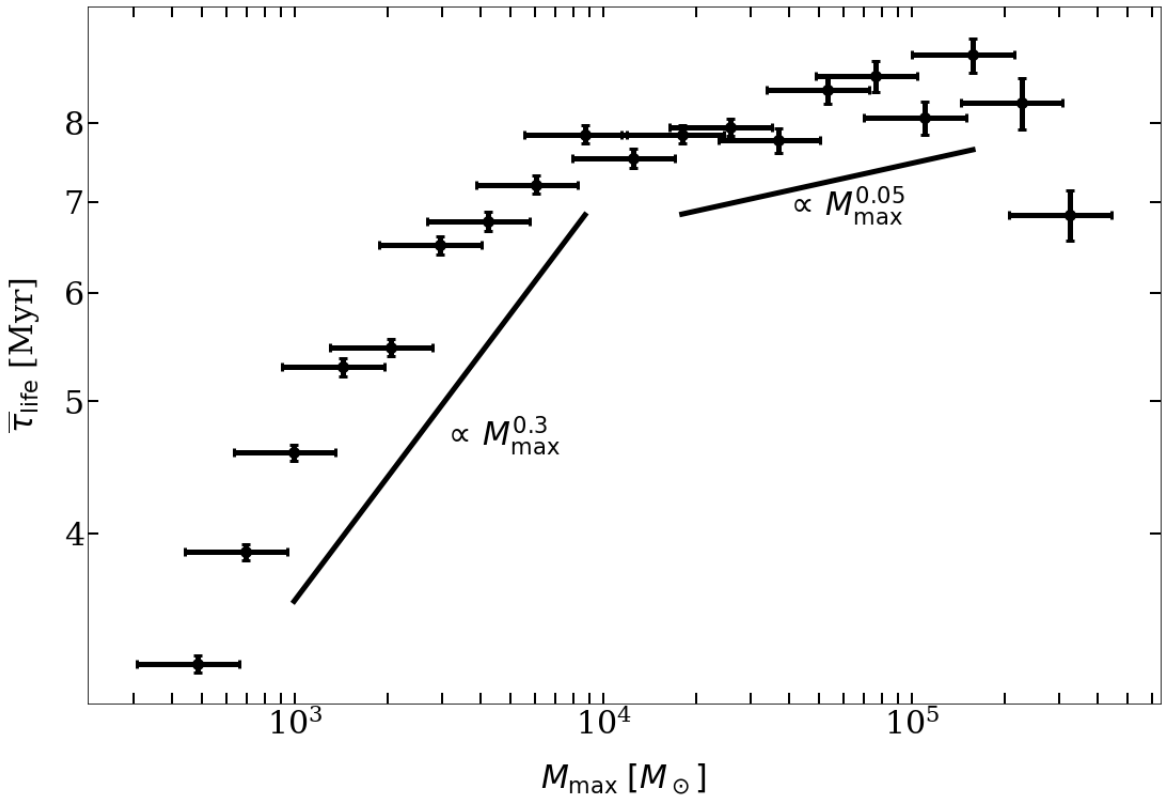

Figure 4.12: Peak mass of the traced clouds during their lifetime $M_{\rm max}$ binned in 20 logarithmic bins vs. the average lifetime of the clouds $\overline{\tau}_{\rm life}$ in each bin. Each scatter point represents each bin. The error bars indicate the errors in the x-axis (i.e. the size of the bin) and the y-axis (i.e. the standard error of the average value of the lifetimes in each bin). The solid lines indicate the indexes of the power-law distributions that represent our sample. For clouds with peak masses $M_{\rm max} < 10^4\,{\rm M}_\odot$ we have $\overline{\tau}_{\rm life} \propto M_{\rm max}^{0.3}$. For clouds with peak sizes $M_{\rm max} > 10^4\,{\rm M}_\odot$ we have $\overline{\tau}_{\rm life} \propto M_{\rm max}^{0.05}$. The trend is that more massive clouds have longer lifetimes and for clouds with peak masses larger than $10^4\,{\rm M}_\odot$ the lifetimes tend to stabilise around 8 Myr.

small size end of our sample the smaller the clouds the longer they live. For the larger cold clouds in our sample (that is clouds with sizes at peak mass $R_{\rm M_{max}} > 20$ pc) we have that $\overline{\tau}_{\rm life} \propto R_{\rm M_{max}}^{0.1}$. This indicates that the larger cold clouds in our sample have longer average lifetimes that tend to stabilise around 8 Myr.

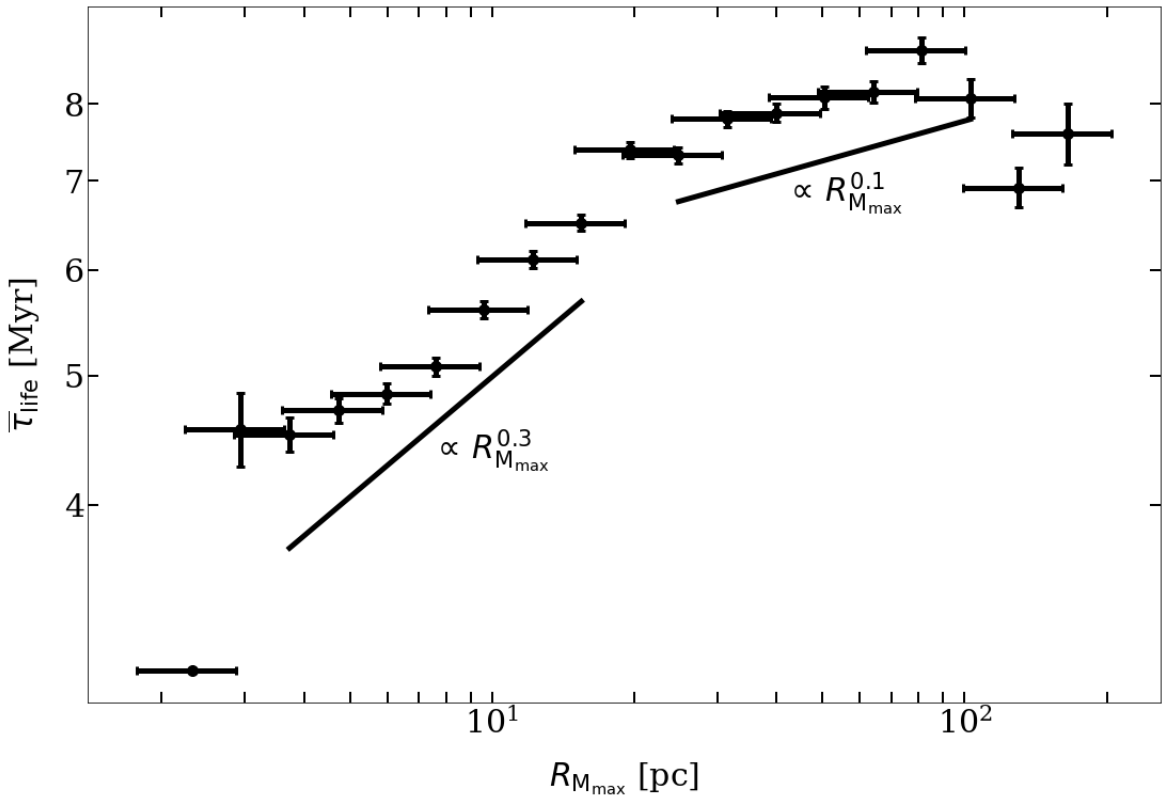

Figure 4.13: Size at peak mass $R_{\rm M_{max}}$ of the traced clouds during their lifetime binned in 20 logarithmic bins vs. the average lifetime of the clouds $\overline{\tau}_{\rm life}$ in each bin. Each scatter point represents each bin. The error bars indicate the errors in the x-axis (i.e. the size of the bin) and the y-axis (i.e. the standard error of the average value of the lifetimes in each bin). The solid lines indicate the indexes of the power-law distributions that represent our sample. For clouds with sizes at their peak mass $R_{\rm M_{max}} < 20$ pc we have $\overline{\tau}_{\rm life} \propto R^{0.3}_{\rm M_{max}}$. For clouds with sizes at their peak mass $R_{\rm M_{max}} > 20$ pc we have $\overline{\tau}_{\rm life} \propto R^{0.1}_{\rm M_{max}}$. The trend is that smaller clouds have shorter lifetimes whereas for clouds with sizes larger than 20 pc the lifetimes tend to stabilise around 8 Myr.

Combining the results of Figs. 4.12 and 4.13 we find a correlation between the mass and the size of the clouds: more massive clouds have larger sizes whereas less massive clouds are smaller. This trend is shown in Fig. 4.14 where we plot the size each traced cold cloud has when it reaches its peak mass $R_{\mathrm{M_{max}}}$ against its peak mass M_{max}. Each scatter point represents each traced cold cloud. The size of the scatter points is scaled with the size of the clouds at their peak mass $R_{\mathrm{M_{max}}}$ for better visualisation. The correlation between the size of the cold clouds and their mass is approximated by a power-law with index 0.5, i.e. $R_{\mathrm{M_{max}}} \propto M_{\mathrm{max}}^{1/2}$.

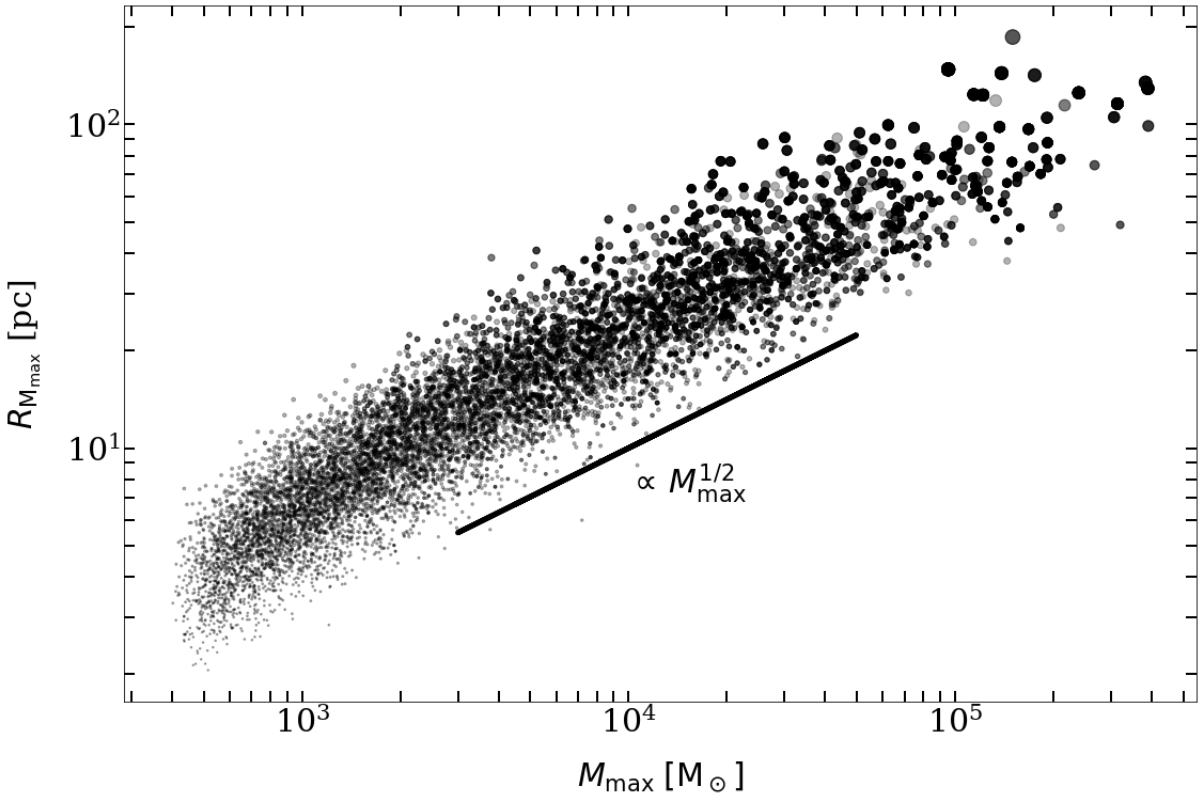

Figure 4.14: Peak mass M_{max} of each cold cloud during its lifetime vs. its size at that given point of its life $R_{\mathrm{M_{max}}}$. Each scatter point represents each traced cold cloud. The size of the scatter points is scaled with the size of the clouds at their peak mass $R_{\mathrm{M_{max}}}$ for better visualisation. The results from Figs. 4.13 and 4.12 indicate a potential correlation between the size and the mass of the traced cold clouds which is shown here: more massive clouds have larger sizes.

The cold ISM of this simulation has a filamentary and clumpy structure, especially after the starburst occurring due to the merging of the individual dwarf galaxies at around 160 Myr. The cold clouds we identified and traced in this work have the characteristic elongated shapes of observed molecular clouds, realistic masses and sizes. In this simulation the H_2 content is very low. Therefore, as we explained in section 2, we use temperature and density criteria in

order to approach realistically the properties of molecular clouds, i.e. we study gas with density $\rho_{\rm gas} > 100\,{\rm cm}^{-3}$ and temperature $T_{\rm gas} < 300\,{\rm K}$, .

The identified cold clouds have density substructure with dense cores embedded in more diffuse cold gas. This is easily seen even by eye in the gallery of massive clouds in Fig. 4.2 where the colormap indicating the mass concentration (from low mass areas in blue to high mass areas in yellow) shows cores of higher density within each cloud. Analysing this further and creating the cloud mass function (CMF) for different density thresholds in Fig. 4.4 we find out that the slope α of the CMF does not change substantially with the increase of the density threshold suggesting self-similarity. The substructure within the clouds is expected from what we know from emission line observations of actual molecular clouds. The observations reveal dense cores with even denser sub-cores and filaments within the clouds (Falgarone et al., 1992; Falgarone & Phillips, 1996; Motte et al., 1998; Testi & Sargent, 1998; Motte et al., 2001).

4.5 Discussion

For the two characteristic snapshots that we display in Fig. 4.4 the slope ranges between $-1.6 \lesssim \alpha \lesssim -1.8$ and remains well in agreement with the observational slope of Heyer et al. (2001) $\alpha_{\rm obs} = -1.8$. Other molecular line observations (Lada et al., 1991; Williams et al., 1994) put the slope in the range of: $-1.3 < \alpha < -1.9$, whereas dust continuum studies (Motte et al., 1998; Testi & Sargent, 1998) find steeper slopes in the range: $-1.9 < \alpha < -2.5$. For a constant density threshold of 100 cm^{-3} we repeat this analysis for the whole time of the simulation. The CMF for these denser cores follows the same power-law distribution with a roughly constant slope in good agreement with the observations (see Figs. 4.5 and 4.6). As we know from the observational studies and we verify with the results of our numerical analysis, the fact that the CMF slope $\alpha < 2$ implies that most of the mass is in the larger clouds. This statement is verified again by our analysis tracing the clouds (see e.g. Fig. 4.14), but we will discuss this further in the next paragraphs.

For a more in-depth comparison of the results of our simulation with observations, we calculate the cloud size function in a similar way to the cloud mass function in Fig. 4.7 using clouds with sizes larger than 3 pc which is the observational limit of Heyer et al. (2001). The cloud size function is a power-law distribution with index α = -2.5 for the two characteristic times of our simulation 170 Myr and 300 Myr, a value close to the Heyer et al. (2001) where $\alpha_{\rm obs} = -3.2$ (see also Solomon et al., 1987; Elmegreen & Falgarone, 1996, and references therein). The selection of the binning and the functions for the data fitting do not play a significant role in the calculation of the values of the power-law indexes.

Having discussed individual cloud properties in the previous sections, we now move on to examine the relationships between the different properties of the clouds. As we mentioned in the Introduction (section 1), it was established in the 1980's by Larson (1981) that molecular clouds follow a set of three scaling relations that connect their kinematic with their structural properties, known as the "Larson relations". These relations have been studied extensively in the literature (see e.g. Larson, 1981; Solomon et al., 1987; Heyer et al., 2001; Bolatto et al., 2008; Heyer et al., 2009; Lombardi et al., 2010; Ballesteros-Paredes et al., 2019, and references therein). In Fig. 4.8 we present the first Larson relation which is a power law dependence of the one-dimension velocity dispersion along the line of sight $\sigma_{\rm v}$ with the cloud size which is represented by the projected half-mass radius $R_{1/2}$: $\sigma_v \propto R_{1/2}^{\alpha}$. As we see from Fig. 4.8 the slope of the simulated power law distribution of $\sigma_{\rm v}$ is well in agreement with observations of Galactic molecular clouds in the disk (Larson, 1981; Dame et al., 1986; Solomon et al., 1987; Heyer et al., 2001; Heyer & Brunt, 2004; Heyer et al., 2009; Ripple et al., 2013) and in the Galactic centre from the CHIMPS2 survey (Eden et al., 2020) and the SEDIGISM survey (Duarte-Cabral et al., 2021).

As we mentioned in section 1 the three Larson relations are not independent but algebraically bound, i.e. if any two are valid the third one is valid, too. In section 4.3, using this bond and equating the mass of the clouds to the virial mass we derived the cohesive equation 4.2 which we use in Fig. 4.7 to check the virialisation of the identified cold clouds. At this point, we would like to mention that during our analysis we calculated the second and third Larson relations (see section 1 for the respective expressions) separately and we verified that they hold in our data-set. However, we do not display them in this work since their information is in the cohesive expression of equation 4.2 and displayed in Fig. 4.9.

Our simulated cold clouds have a virial parameter of $\alpha_{\rm vir} \sim 10$ (see Fig. 4.9). Observed molecular clouds in the Milky Way typically fall in between a virial parameter $\alpha_{\rm vir}$ of 1 and 3 (Heyer et al., 2009; Heyer & Dame, 2015) and the trend is similar in molecular clouds in nearby galaxies (Bolatto et al., 2008; Leroy et al., 2015). However, Evans et al. (2021) support that molecular clouds are not generally virialised, but the dense cores that are indeed gravitationally bound are the virialised part of a cloud. Conducting many tests with different density thresholds in the identification of the cold clouds in our study, we find that a density threshold of $\rho_{\rm gas} > 1000\,{\rm cm}^{-3}$ lowers the virial parameter to 1. Therefore, our conclusion converges with Evans et al. (2021). The relationship between the velocity dispersion $\sigma_{\rm v}$ and the product of the size $R_{\rm MC}$ and the surface density $\Sigma_{\rm MC}$ of molecular clouds has received several interpretations. Heyer et al. (2009) consider the values of $\Sigma_{\rm MC}$ in their sample as lower limits due to observational constraints, therefore their clouds only roughly equalise the effects of gravity with kinetic energy. Ballesteros-Paredes et al. (2011) consider the discrepancy a result of gravitationally collapsing clouds. Finally, McKee et al. (2010); Field et al. (2011); Hennebelle & Falgarone (2012) support that short-lived clouds

confined by external pressure can have virial parameters > 1 and still follow a relation between the velocity dispersion and the size (first Larson relation) without the presence of Σ_{MC}. The literature is not definitive as to why molecular clouds that follow the Larson relations can show this discrepancy in the σ_v - $R_{MC}\Sigma_{MC}$ relationship. In our case, given our findings, the most promising explanation is that the clouds we identify have dense cores in virial equilibrium surrounded by cocoons of diffuse gas that are not virialised.

4.6 Summary

The extended starburst has impacted the morphology and the evolution of the multi-phase ISM of the system, causing the cold ISM to have a filamentary and clumpy structure. After analysing this cold and dense phase of the ISM, we discovered hundreds of simulated cold clouds with mass and size properties well in agreement with observations of molecular clouds. The identified simulated cold clouds have also the distinctively asymmetrical geometries of molecular clouds with density substructure. The characteristics of the detected cold clouds were thoroughly researched and compared to the results of observational and numerical studies. The slope of the cloud mass function (CMF): $dN/dM \propto M^{\alpha}$ remains roughly constant independently of the density threshold, indicating self-similar density substructure. For a fixed density threshold, the slope of the CMF remains roughly constant with time and well in agreement with the observations. Similarly, the slope of the cloud size function: $dN/dR_{1/2} \propto R_{1/2}^{\alpha}$ remains roughly constant with time and well in agreement with observations. The identified cold clouds follow the "Larson relations", that connect their kinematic with their structural properties.

We traced the lifecycle of the identified cold clouds, documenting their growth and destruction phases. Our analysis of the properties of the simulated cold clouds revealed that their lifetimes scale with their masses. The e-folding timescales range from 3.2 Myr in the lower-mass end up to 5.4 Myr in the higher-mass end. Furthermore, the lifetime of the cold clouds follows a power-law distribution $\tau_{life} \propto R_{M_{max}}^{\alpha}$. Cold clouds with sizes at peak mass $R_{M_{max}}$ up to 20 pc have a power-law index α=0.3, whereas clouds with sizes at peak mass larger than 20 pc have $\alpha \sim 0.1$. This means that the larger the clouds the longer they live up to 20 pc and then their lifetimes tend to stabilise around 8 Myr.There is also a correlation between the mass and the size of the cold clouds: more massive clouds have larger sizes.

The cold clouds we identified and traced in the simulation are connected with star formation, since star clusters form within the cold and dense regions of molecular clouds. To take our study one step further, we aim to connect these simulated cold clouds with the star clusters that have been identified in our system, eventually studying the transformation of cold clouds to star clusters. This is the subject of the following chapter.

Chapter 5

From cold clouds to star clusters

In this chapter we study the evolution of the cold clouds of chapter 4 and their transformation into star clusters.
The results of this chapter are scheduled to be submitted to the "*Monthly Notices of the Royal Astronomical Society" (MNRAS)* for publication.

5.1 Star forming cold clouds

After studying the properties of the cold clouds detected in our simulation and tracing their life cycle, we proceed into expanding our analysis to the next level. We follow the evolutionary tracks of the cold clouds and study them further when they form star clusters. For this purpose, we use a different tracing routine from the one used in chapter 4 (as explained in detail in section 2), in order to trace groups of cold gas and stars. From now on we will refer to these groups of cold ($T_{\rm gas} < 300$ K) and dense ($\rho_{\rm gas} > 100$ cm^{-3}) gas and stars as "clumps".

With our analysis we tracked 60005 individual clumps consisting of cold gas and stars from shortly before the starburst (~ 150 Myr) until the end of the simulation (~ 457 Myr).
For instance, take the third most massive cold cloud that we detected at the time $t_{\rm sim}$=300 Myr of our simulation in chapter 4 (see e.g. fourth panel of Fig. 4.1 and third panel of Fig. 4.2). With the new tracing routine, we identify not only the cold gas cloud, but also the stars that have formed within. The results are presented in Fig. 5.1. In the left panel of Fig. 5.1, we present a visualisation of the SPH gas particle distribution of this particular cloud, using the mass distribution as a colormap. The colormap highlights the variations in shape and substructure of the cloud projected on the x-y plane. Blue hues map areas of low mass, whereas yellow hues map areas of high mass concentration. In the right panel of Fig. 5.1, we show the raw scatter of the SPH particles projected on the x-y plane. Blue circles represent the SPH cold gas particles, whereas yellow star markers represent the SPH star particles. The cloud is centred at its densest

region in both panels. As shown in chapter 4 of the present work, the gas mass of this cloud is $M_{\rm gas} = 5.7 \times 10^4$ M$_\odot$ which is confirmed by the new tracing routine, as well. The stellar component has a mass of $M_* = 6.7 \times 10^3$ M$_\odot$. Comparing the two panels of Fig. 5.1, we see that the projected position of the stars (right panel) coincides with the yellow areas of high mass concentration (left panel), as expected.

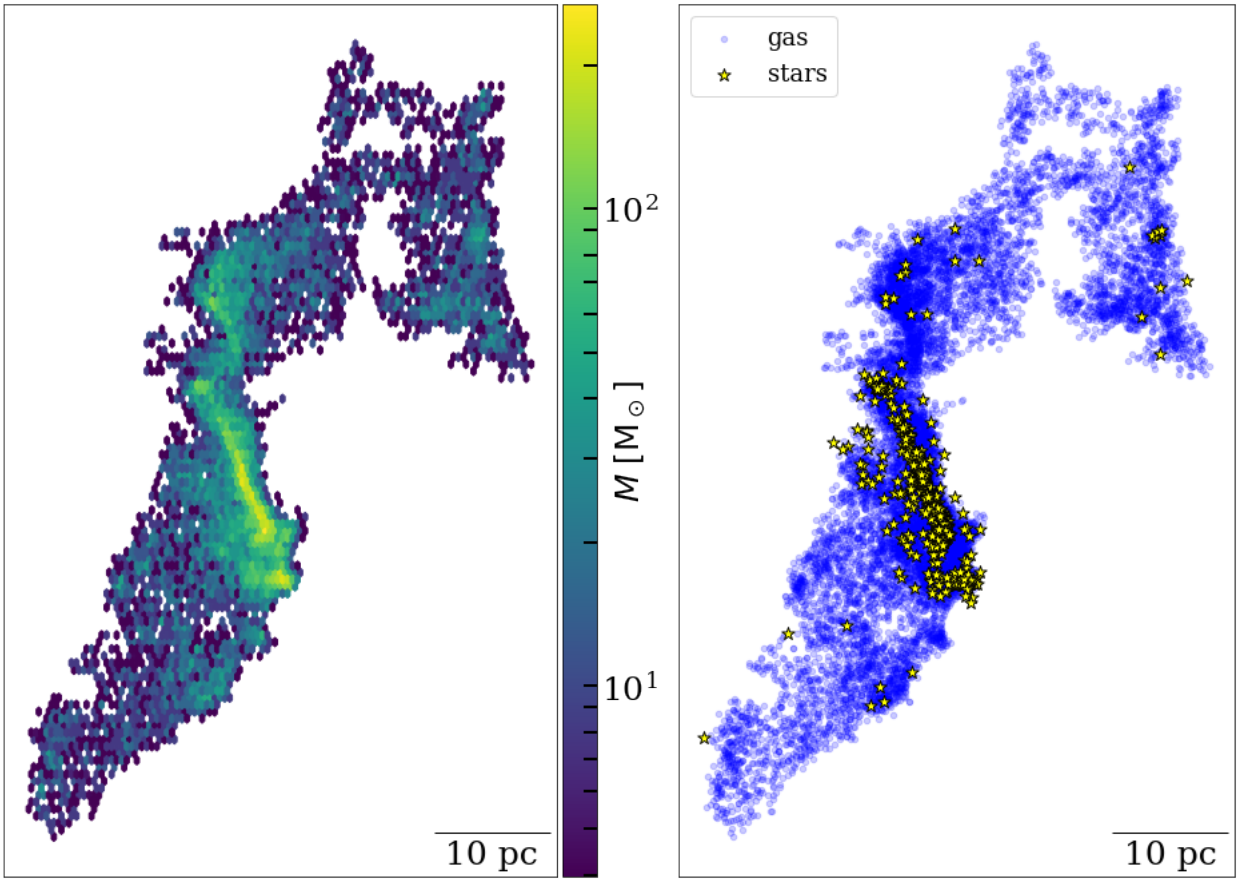

Figure 5.1: Overview figure of the SPH cold gas and stars particles distribution in the third most massive cloud at $t_{\rm sim} = 300$ Myr of the simulation. We have traced this cold gas cloud in chapter 4 of the present work (see Figs. 4.1 and 4.2). However, in chapter 4 we only mapped the cold gas in this cloud. In this chapter, using the new tracing routine (see section 2 for details) we are able to trace also the SPH stellar particle distribution, thus mapping the star formation taking place in the cloud. *Left panel*: Visualisation of the SPH gas particle distribution of the cloud, using the mass distribution as a colormap, projected on the x-y plane. Blue hues map areas of low mass, whereas yellow hues map areas of high mass concentration. The gas mass of the cloud is: $M_{\rm gas} = 5.7 \times 10^4$. *Right panel*: Raw scatter of the SPH particles projected on the x-y plane. Blue circles represent the SPH cold gas particles, whereas yellow star markers represent the star particles. The stellar mass in the cloud is: $M_* = 6.7 \times 10^3$ M$_\odot$. The cloud is centred at its densest region in both panels.

In Fig. 5.2 we plot the histogram of the lifespan of all clumps traced in our simulation. This general histogram shows all groups identified and traced, from shortly before the major starburst (∼ 150 Myr) until the end of the simulation (∼ 457 Myr) and consists of all kinds of groups: cold gas clouds consisting only of gas, star clusters consisting only of SPH stellar particles without gas or clumps of cold gas and stars. For this reason, the lifetimes of the traced groups can reach up to 300 Myr, whereas the cold gas clouds we studied in chapter 4 had maximum lifetimes of roughly 30 Myr. The oldest objects in the histogram are star clusters (star clusters have been detected in the system by Lahén et al. (2019, 2022)).

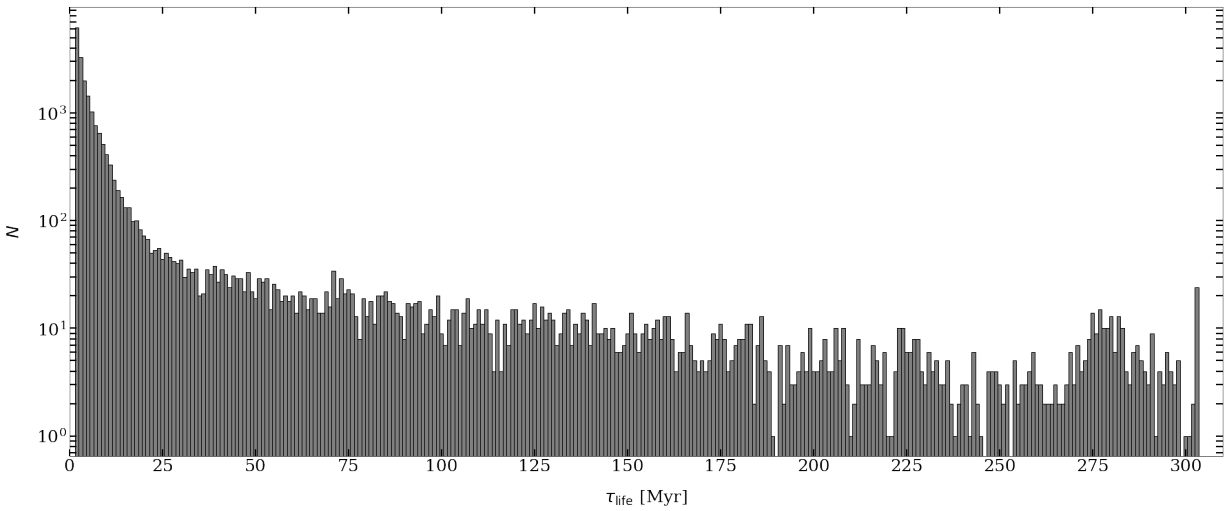

Figure 5.2: Lifespan histogram of the traced clumps in our simulation, from shortly before the major starburst (∼ 150 Myr) until the end of the simulation (∼ 457 Myr). This histogram comprises all kinds of groups: cold gas clouds consisting only of gas, star clusters consisting only of SPH stellar particles without gas or clumps of cold gas and stars.

5.2 Orbital analysis of the clumps

In Fig. 5.3, we plot the orbits of the centre of mass of the nine longest living clumps in the simulation on the x-y plane. These objects have lifespans of ∼ 300 Myr (see Fig. 5.2) and they comprise of little to no gas, therefore they are most probably star clusters. The centres of mass have orbits with compact configuration (see e.g. the third and the last panels of Fig. 5.3) or elongated orbits spanning for a few kpc during their lifetimes (see e.g. the second and the sixth panels of Fig. 5.3). No matter the orbital configuration of these clumps, they retain orbits for ∼ 300 Myr, therefore they survive from the onset of the starburst until the end of the simulation providing us with information about the whole evolution of the system.

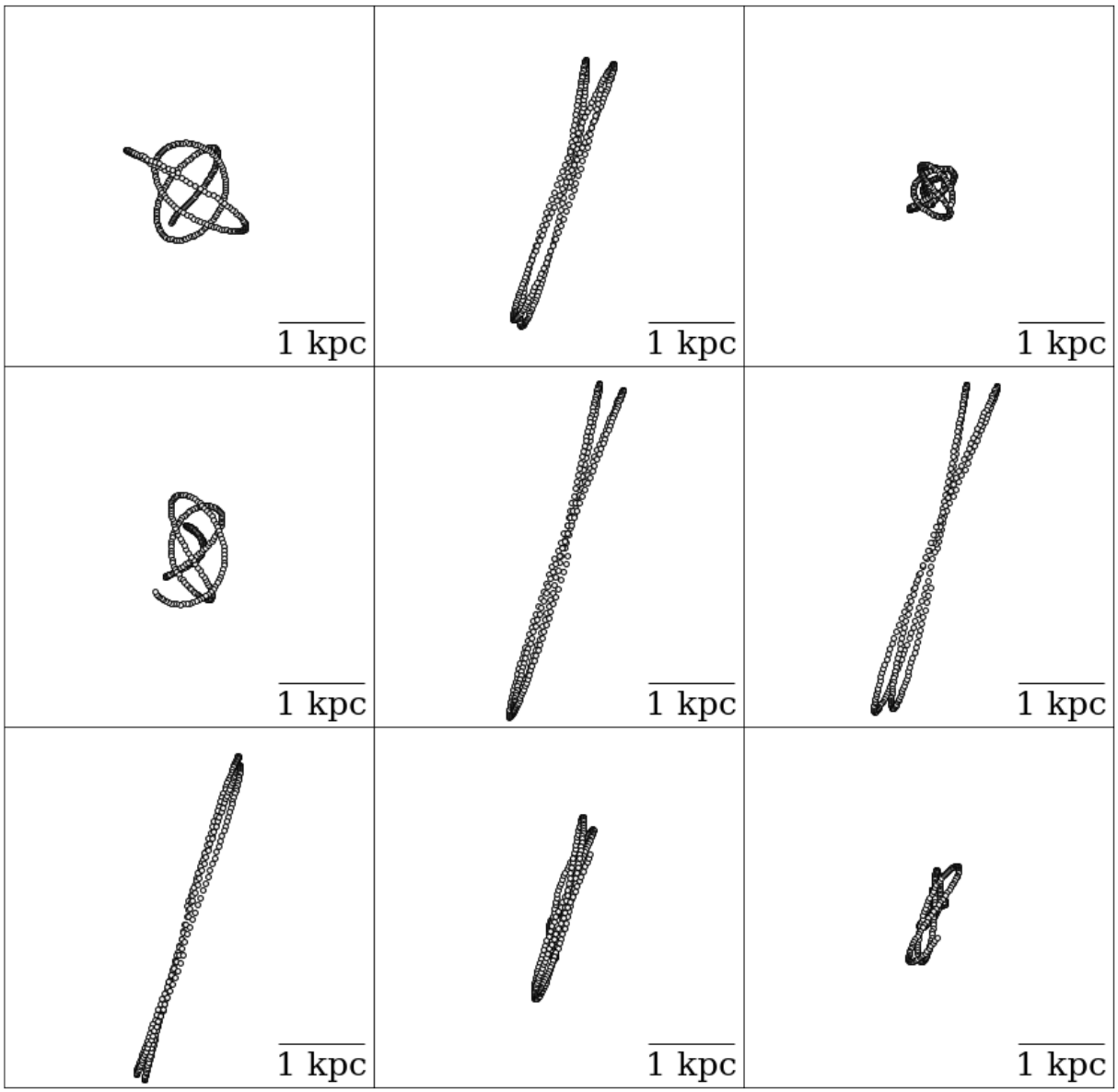

Figure 5.3: Orbits of the centre of mass of the nine longest living clumps traced in the simulation on the x-y plane. The long lifespans of these clumps ($\sim$ 300 Myr) and the fact that they consist of little to no gas, make them potential candidates for star clusters.

Except for the orbits of the centres of masses of these clumps, it is interesting to check the behaviour of the radial distances. In Fig. 5.4 we show the time evolution of the radial distance r of the centres of mass of the nine longest living clumps traced in our simulation. The radial distance of the centres of mass changes periodically as expected, since the material in the galaxy, therefore these nine clumps, as well, orbit the galactic centre. Therefore, it is expected to see symmetrical fluctuations in the radial distance of the objects, as shown in Fig. 5.4. We should

note that the clumps with compact orbital configurations in Fig. 5.3 have also smaller radial distances from the centre of the system (see e.g. the third and the last panels of Figs. 5.3 and 5.4).

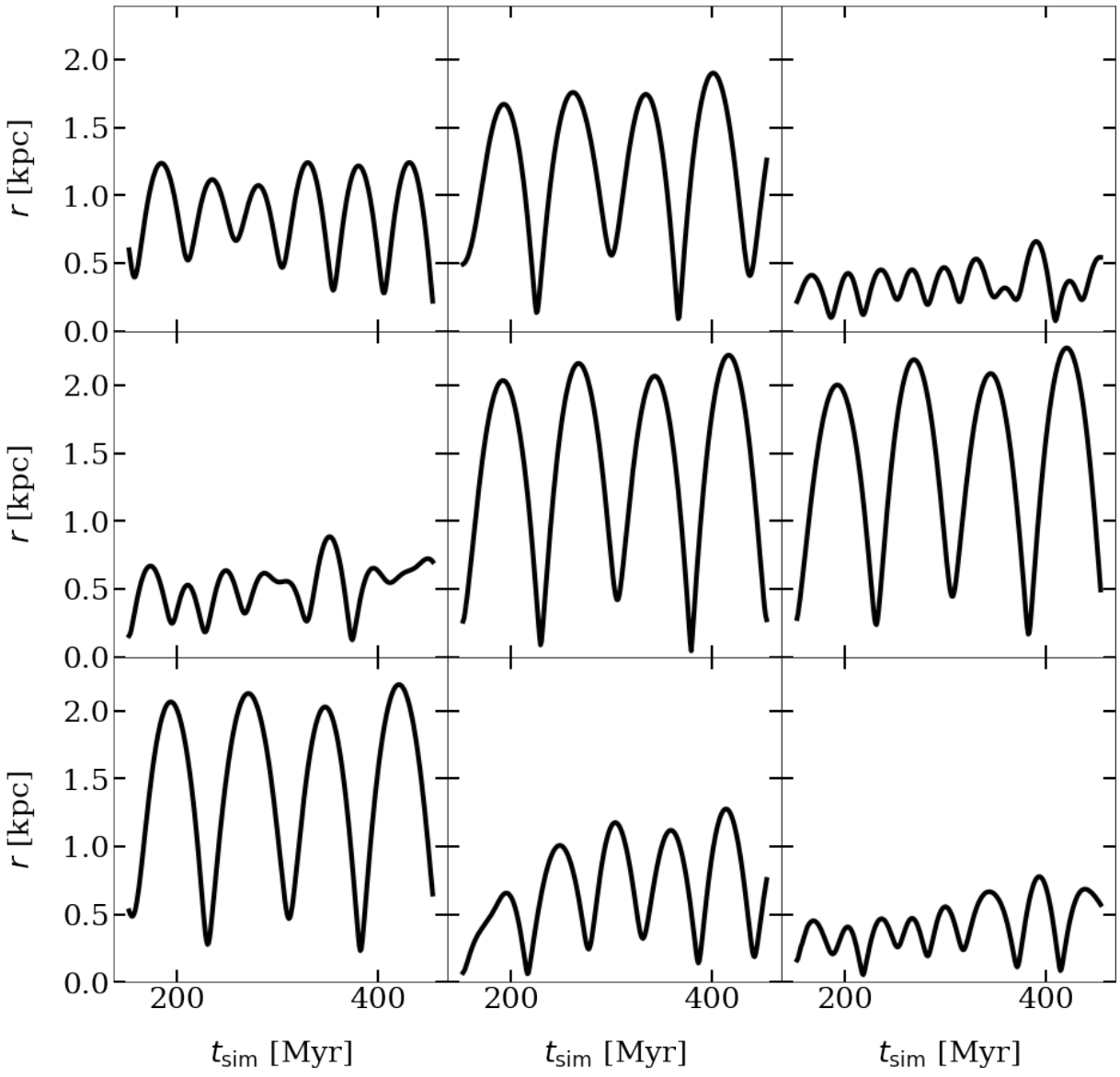

Figure 5.4: Time evolution of the radial distance of the centre of mass of the nine longest living clumps traced in our simulation.

5.3 Mass evolution of star forming clouds

In Fig. 5.3 we showed the orbits -on the x-y plane- of the centres of mass of the nine longest living clumps traced in the simulation. We deduced that these objects are most probably star clusters due their long lifespans (~ 300 Myr) and their compact configurations. In Fig. 5.5 we show the mass evolution these clumps.

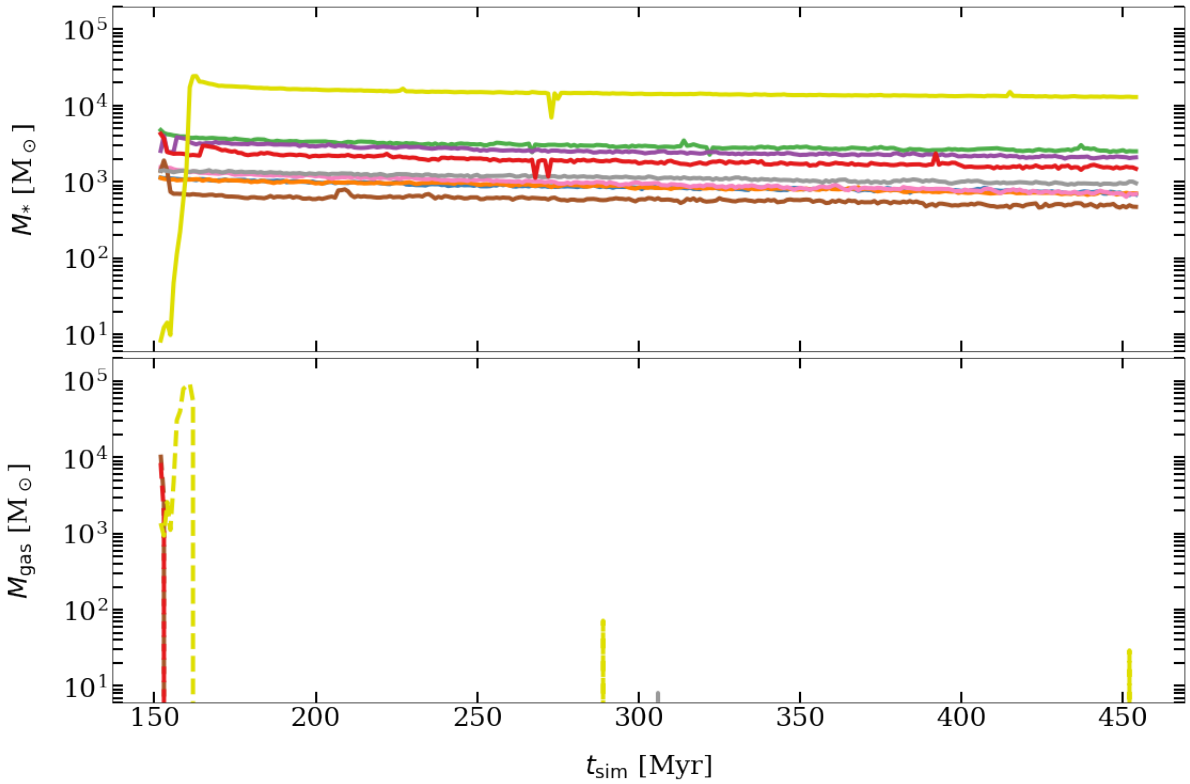

Figure 5.5: Time evolution of the mass of the nine longest living clumps traced in the simulation. Stellar mass evolution M_* (top panel) and cold gas mass evolution $M_{\rm gas}$ (bottom panel). The x-axis is the time of the simulation from shortly before the starburst (~ 150 Myr) until the end of the simulation. Each line represents one of the traced clumps.

The mass evolution of the stars is shown in the top panel of Fig. 5.5 and the mass evolution of the cold gas is shown in the bottom panel. The x-axis is the time of the simulation from shortly before the starburst (~ 150 Myr) until the end of the simulation. Each line represents one of the traced clumps. The clumps have stellar masses from ~ 10^3 M$_\odot$ up to ~ 10^4 M$_\odot$ and most of them have no or little gas mass. For the most massive clump (yellow) we see that it begins as a cold gas cloud (bottom panel) with the characteristic growth phase reaching up to ~ 10^5 M$_\odot$ and then when the mass budget is enough, the cold cloud enters its destruction phase, i.e. the cold gas

mass lowers transforming in stellar mass. In the simulation the stars form through "instantaneous star formation", meaning that SPH gas particles transform instantaneously into stellar particles. So the transition from cold gas to stars is not smooth, but it is marked by the sudden rise in stellar mass shown in the top panel of Fig. 5.5. The lifetimes of these objects ($\sim$ 300 Myr) and their masses (up to $\sim 10^4$ $M_\odot$) are strong indications that these objects are star clusters.

We perform the same analysis as in Fig. 5.5 for the 100 longest living clouds. The results are presented in Fig. 5.6. The solid lines represent the time evolution of the stellar mass M_*, whereas the dashed lines represent the time evolution of the cold gas mass $M_{\rm gas}$ in the traced clumps. Each line represents one clump. As for the nine longest living clumps, the behaviour of the mass evolution is similar. When the mass budget is sufficient, the cold clouds enter their destruction phase, during which their masses lower and transform into stellar masses. This is the case for the clumps, which start out as a cold gas clouds with the characteristic growth phases reaching up their peak gas masses before entering their destruction phases. The stellar masses reach up to $\sim 3 \times 10 * 5$ $M_\odot$ at the time of their creation. As time passes, the clumps in general lose mass (e.g. due to stellar winds) with moments of small mass increase (e.g. due to merging with other clumps) until the end of the simulation.

In Fig. 5.7 we calculate the fractions of cold gas in each of the 100 longest living clumps of Fig. 5.6. The gas fractions are defined as fractions of the cold gas mass $M_{\rm gas}$ divided by the total mass M_* + $M_{\rm gas}$ of the clumps. The dashed line indicates unity. During the early times around the starburst ($\sim$ 150 - 200 Myr) the majority of the clumps have high gas fractions reaching unity. This is when the majority of the cold clouds forms, as we showed in chapter 4. As time passes, the gas fractions in general decrease. This is expected based on our analysis so far, that shows a trend of clumps beginning as cold clouds and evolving into star clusters that live up to 300 Myr.

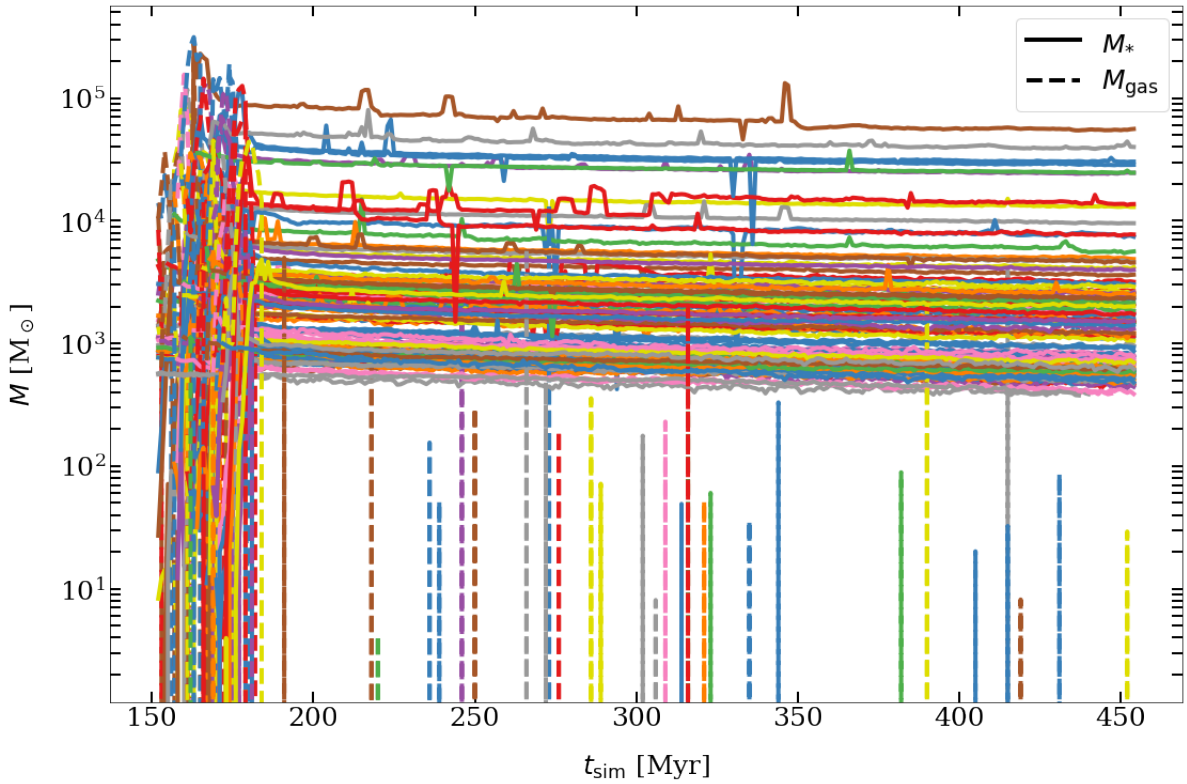

Figure 5.6: Time evolution of the mass of 100 longest living clumps traced in our simulation. Stellar mass evolution M_* (solid lines) and cold gas mass evolution M_{gas} (dashed lines). The x-axis is the time of the simulation from shortly before the starburst ($\sim$ 150 Myr) until the end of the simulation. Each line represents one of the traced clumps.

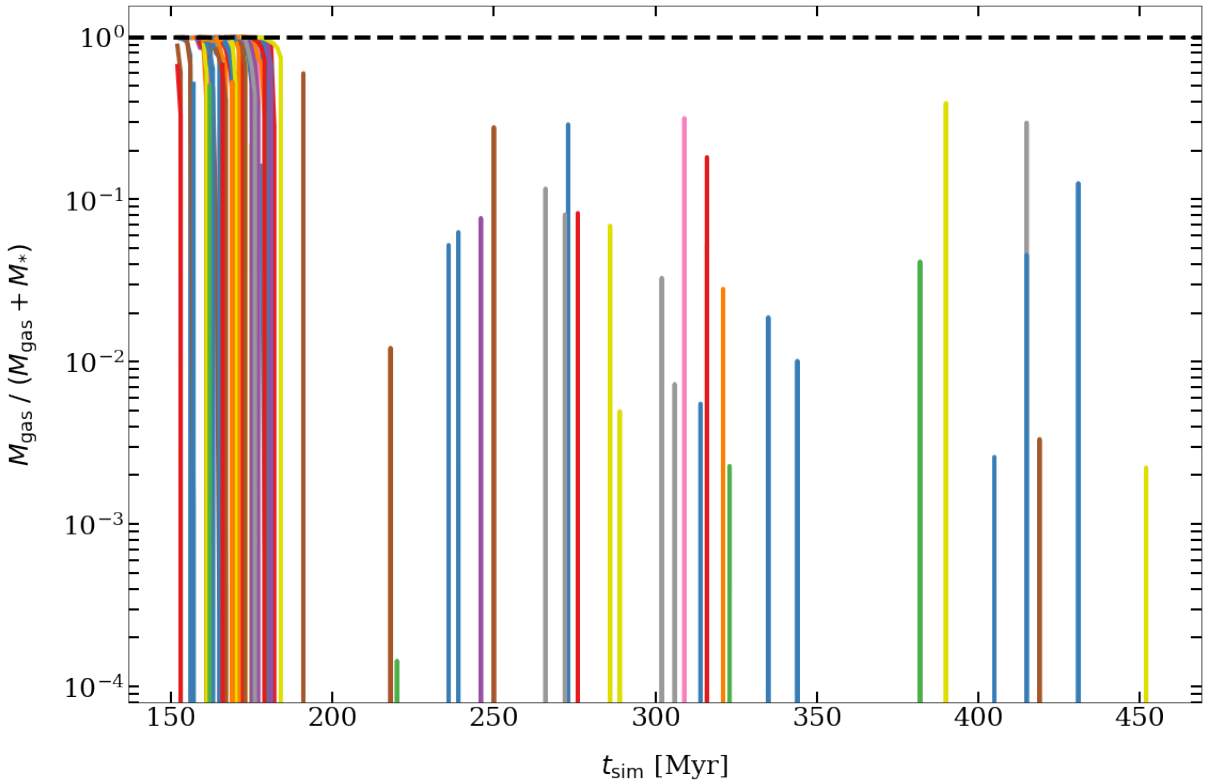

Figure 5.7: Time evolution of the cold gas mass fraction of 100 longest living clumps traced in the simulation. The cold gas mass fractions are defined as fractions of the cold gas mass M_{gas} divided by the total mass $M_* + M_{\mathrm{gas}}$ of the clumps. The dashed line indicates unity.

5.4 Summary & future goals

We studied the evolution of the cold clouds that we examined in chapter 4, using a new tracing routine. With the new tracer we had the ability to trace not only cold gas clouds, but also the stars, thus identifying star forming cold clouds, that we call "clumps". These clumps have long lifespans up to $\sim$ 300 Myr, masses of up to $\sim 10^5$ $M_\odot$ and sustain well-defined orbits throughout their lifetimes. Through our analysis, we mapped the time evolution of these clumps and identified the growth phase of the cold gas clouds and their subsequent destruction phase and transformation into star clusters. We form the conjecture that these long living clumps with the low gas fractions are actually star clusters, since they share star cluster properties, such as their high masses (see e.g. Lada & Lada, 2003; McKee & Ostriker, 2007) and their long lifespans (see e.g. Harris, 1991; Marín-Franch et al., 2009; Brandt & Huang, 2015). However, to formulate a concrete conclusion we must conduct further analysis of the properties of these clumps. We aim to calculate the cloud mass functions, construct radial stellar mass density and radial stellar surface density profiles and conduct a study of the kinematic properties of the clumps. Our future goals also include an in-depth comparison of our findings with the literature of observational and theoretical studies of star clusters and the evolution of molecular clouds.

Chapter 6

Summary & Conclusions

In this work we studied the multi-phase interstellar medium (ISM) in a very high resolution hydrodynamical simulation of a gas-rich metal-poor dwarf galaxy merger. The simulation has 4 $M_\odot$ mass resolution and 0.1 pc spatial resolution. It is resolved with individual massive stars and it supports a rapid disruption model for star-forming clouds by stellar radiation and supernova feedback. The initial conditions are set up with two identical dwarf galaxies at $z = 0$ and the evolution of the system is as follows: the dwarf galaxies first approach at 5 Myr and their first pericentric passage happens at around 50 Myr. After their initial approach, they move away from each other with their first apocentre at 80 Myr. At 160 - 170 Myr they approach for the second time and this is the onset of the major starburst.

Through our analysis of the multi-phase ISM in this simulation, we identified a surprisingly extended starburst, both in space and time. Even at great distances from the centre of the system (i.e. $r = 5$ kpc) and for the whole duration of the simulation (457 Myr), star formation continues taking place. This shows that the extended starburst drives outflows in our system that cannot exhaust the gas reservoir, from which stars form, entirely. However, the gas reservoir of the system can run out within a few dynamical times, since the inflow rates $\dot{M}_{\rm in}$ recorded after the major starburst are systematically lower than the outflow rates $\dot{M}_{\rm out}$. The outflow rates measured at various distances from the centre of the system are stronger closer to the centre with mass loadings n above unity. The strongest outflows are detected in the the "warm" phase of the ISM ($300\,{\rm K} \leq T_{\rm gas} < 2 \times 10^4\,{\rm K}$) carrying out mostly atomic (H) and ionised (H^+) hydrogen. The outflows carry out metals, as well, especially in the "warm-hot" phase ($2 \times 10^4\,{\rm K} \leq T_{\rm gas} < 2 \times 10^5\,{\rm K}$).

Overall, the morphology and the evolution of the system are significantly impacted by the extended starburst. The starburst drives multi-phase galactic outflows that accelerate or heat up the gas, thus depleting the reservoir from which stars form and it promotes extensive star formation in the system, providing us with a detailed model for the multi-phase ISM and the ideal setting to research the emergence and evolution of cold star-forming clouds.

Due to the starburst, the cold ISM of the system has filamentary and clumpy structure. We analysed

the cold and dense ISM and we identified hundreds of cold clouds with realistic mass and size properties and the characteristic irregular shapes of molecular clouds with density substructure. We studied extensively the properties of the identified cold clouds and we summarise them in the following paragraphs.

The slope of the simulated cloud mass function (CMF): $dN/dM \propto M^{\alpha}$ remains roughly constant independently of the density threshold we use, indicating self-similar density substructure. Furthermore, the slope of the CMF remains roughly constant with time and well in agreement with the observations: $dN/dM \propto M^{\alpha}$ with $\alpha_{\rm mean} = -1.78(\pm 0.08)$. Similarly, the slope of the cloud size function remains roughly constant with time and well in agreement with observations: $dN/dR_{1/2} \propto R_{1/2}^{\alpha}$, with a typical index of $\alpha = -2.5$. The identified clouds follow the Larson relations, which are observationally established relations that connect the kinematic with the structural properties of the clouds.

Furthermore, we traced the lifecycle of the identified cold clouds documenting their growth and destruction phases. The lifetime of the cold clouds scales with their masses. The e-folding timescales range from 3.2 Myr in the lower-mass end up to 5.4 Myr in the higher-mass end. The lifetime of the cold clouds follows a power-law distribution $\tau_{\rm life} \propto M_{\rm max}^{\alpha}$. Cold clouds with peak masses $M_{\rm max}$ up to 10^4 $M_{\odot}$ have a power-law index α=0.3, whereas clouds with peak masses larger than 10^4 $M_{\odot}$ have $\alpha \sim 0.05$. The more massive the clouds the longer they live up to 10^4 $M_{\odot}$ and then their lifetimes tend to stabilise around 8 Myr. The lifetime of the cold clouds follows a power-law distribution $\tau_{\rm life} \propto R_{\rm M_{max}}^{\alpha}$. Cold clouds with sizes at peak mass $R_{\rm M_{max}}$ up to 20 pc have a power-law index α=0.3, whereas clouds with sizes at peak mass larger than 20 pc have $\alpha \sim 0.1$. The larger the clouds the longer they live up to 20 pc and then their lifetimes tend to stabilise around 8 Myr. There is a correlation between the mass and the size of the cold clouds: more massive clouds have larger sizes.

The cold clouds that we identified and traced in our simulation have properties well in agreement with observed molecular clouds and simulated clouds of other numerical studies. Despite the low H_2 content in our dwarf starburst, our approach for simulating molecular clouds (i.e. low temperature $T_{\rm gas} < 300$ K and high density $\rho_{\rm gas} > 100\,{\rm cm}^{-3}$) works well. The final aim of this work is to connect these cold clouds with star clusters forming from them.

Using a novel tracing routine, we investigated the evolution of the cold clouds. We were able to identify the star-formation within the cold clouds in addition to tracing these cold star forming "clumps". These clumps have long lifespans up to $\sim$ 300 Myr, masses of up to $\sim 10^5$ M$\odot$ and sustain well-defined orbits throughout their lifetimes. We plotted the time evolution of both the cold gas and the stellar mass components of these clumps and pinpointed the phases of growth and destruction of the cold gas clouds and their subsequent transformation into star clusters, thus creating a complete and detailed study of the evolution of molecular clouds and the star formation within them.

With this thesis, we improve our understanding of the multi-phase ISM and the processes governing it and create a detailed analysis of the mechanisms regulating the emergence and evolution of

cold star-forming clouds, thus assessing how well the underlying simulation accurately reflects the observable conditions for star formation in merging galaxies.

Bibliography

Aartsen M. G., Abbasi R., Abdou Y., Ackermann M., Adams J., et al., 2013, Phys. Rev. D, 88, 042004

Ackermann M., Ajello M., Allafort A., Baldini L., Ballet J., et al., 2013, Science (80-.)., 339, 807

Bakes E. L. O., Tielens A. G. G. M., 1994, ApJ, 427, 822

Ballesteros-Paredes J., Klessen R. S., Mac Low M. M., Vazquez-Semadeni E., 2007, in Reipurth B., Jewitt D., Keil K., eds, Protostars and Planets V. p. 63 (arXiv:astro-ph/0603357)

Ballesteros-Paredes J., Hartmann L. W., Vázquez-Semadeni E., Heitsch F., Zamora-Avilés M. A., 2011, MNRAS, 411, 65

Ballesteros-Paredes J., Román-Zúñiga C., Salomé Q., Zamora-Avilés M., Jiménez-Donaire M. J., 2019, MNRAS, 490, 2648

Beck R., 2015, A&A Rev., 24, 4

Bell A. R., 1978, MNRAS, 182, 443

Benincasa S. M., Wadsley J. W., Couchman H. M. P., Pettitt A. R., Tasker E. J., 2019, MNRAS, 486, 5022

Bertoldi F., McKee C. F., 1992, ApJ, 395, 140

Bieri R., Naab T., Geen S., Coles J. P., Pakmor R., et al., 2022, arXiv e-prints, p. arXiv:2209.06842

Bolatto A. D., Leroy A. K., Rosolowsky E., Walter F., Blitz L., 2008, ApJ, 686, 948

Bolatto A. D., Wolfire M., Leroy A. K., 2013, ARA&A, 51, 207

Brandt T. D., Huang C. X., 2015, ApJ, 807, 24

Calzetti D., Meurer G. R., Bohlin R. C., Garnett D. R., Kinney A. L., et al., 1997, AJ, 114, 1834

Camps P., Behrens C., Baes M., Kapoor A. U., Grand R., 2021, ApJ, 916, 39

Chevance M., Kruijssen J. M. D., Hygate A. P. S., Schruba A., Longmore S. N., et al., 2020, MNRAS, 493, 2872

Chevance M., Kruijssen J. M. D., Krumholz M. R., Groves B., Keller B. W., et al., 2022, MNRAS, 509, 272

Chieffi A., Limongi M., 2004, ApJ, 608, 405

Cicone C., Maiolino R., Sturm E., Graciá-Carpio J., Feruglio C., et al., 2014, A&A, 562, A21

Clark P. C., Glover S. C. O., Klessen R. S., 2012, MNRAS, 420, 745

Cole S., Lacey C. G., Baugh C. M., Frenk C. S., 2000, MNRAS, 319, 168

Cox D. P., 2005, ARA&A, 43, 337

Dame T. M., Elmegreen B. G., Cohen R. S., Thaddeus P., 1986, ApJ, 305, 892

Dasyra K. M., Bostrom A. C., Combes F., Vlahakis N., 2015, ApJ, 815, 34

Dasyra K. M., Combes F., Oosterloo T., Oonk J. B. R., Morganti R., et al., 2016, A&A, 595, L7

Dobbs C. L., Pringle J. E., 2013, MNRAS, 432, 653

Dobbs C. L., Krumholz M. R., Ballesteros-Paredes J., Bolatto A. D., Fukui Y., et al., 2014, in Beuther H., Klessen R. S., Dullemond C. P., Henning T., eds, Protostars and Planets VI. p. 3 (arXiv:1312.3223), doi:10.2458/azu_uapress_9780816531240-ch001

Dolag K., Borgani S., Schindler S., Diaferio A., Bykov A. M., 2008, Space Sci. Rev., 134, 229

Dorfi E. A., Breitschwerdt D., 2012, Astron. Astrophys., 540, 77

Draine B. T., 2011, Physics of the Interstellar and Intergalactic Medium. Princeton University Press

Dressler A., Gunn J. E., 1983, ApJ, 270, 7

Duarte-Cabral A., Colombo D., Urquhart J. S., Ginsburg A., Russeil D., et al., 2021, The SEDIGISM survey: molecular clouds in the inner Galaxy, Monthly Notices of the Royal Astronomical Society, Volume 500, Issue 3, pp.3027-3049 (arXiv:2012.01502), doi:10.1093/mnras/staa2480

Eden D. J., Moore T. J. T., Currie M. J., Rigby A. J., Rosolowsky E., et al., 2020, MNRAS, 498, 5936

Ellison S. L., Patton D. R., Simard L., McConnachie A. W., 2008, AJ, 135, 1877

Ellison S. L., Patton D. R., Mendel J. T., Scudder J. M., 2011, MNRAS, 418, 2043

Ellison S. L., Mendel J. T., Patton D. R., Scudder J. M., 2013, MNRAS, 435, 3627

Elmegreen B. G., 1983, MNRAS, 203, 1011

Elmegreen B. G., Efremov Y. N., 1997, ApJ, 480, 235

Elmegreen B. G., Falgarone E., 1996, ApJ, 471, 816

Evans Neal J. I., Heyer M., Miville-Deschênes M.-A., Nguyen-Luong Q., Merello M., 2021, ApJ, 920, 126

Fabian A. C., 2012, ARA&A, 50, 455

Falgarone E., Phillips T. G., 1996, ApJ, 472, 191

Falgarone E., Puget J. L., Perault M., 1992, A&A, 257, 715

Fall S. M., Chandar R., 2012, ApJ, 752, 96

Ferguson H. C., Babul A., 1998, MNRAS, 296, 585

Ferrière K. M., 2001, Reviews of Modern Physics, 73, 1031

Field G. B., Goldsmith D. W., Habing H. J., 1969, ApJ, 155, L149

Field G. B., Blackman E. G., Keto E. R., 2011, MNRAS, 416, 710

Fixsen D. J., 2009, ApJ, 707, 916

Fotopoulou C. M., Dasyra K. M., Combes F., Salomé P., Papachristou M., 2019, A&A, 629, A30

Fujimoto Y., Chevance M., Haydon D. T., Krumholz M. R., Kruijssen J. M. D., 2019, MNRAS, 487, 1717

Fukui Y., Kawamura A., 2010, ARA&A, 48, 547

Gallagher John S. I., 1993, in Cassinelli J. P., Churchwell E. B., eds, Astronomical Society of the Pacific Conference Series Vol. 35, Massive Stars: Their Lives in the Interstellar Medium. p. 463

Girichidis P., Naab T., Hanasz M., Walch S., 2018, MNRAS, 479, 3042

Girichidis P., Offner S. S. R., Kritsuk A. G., Klessen R. S., Hennebelle P., et al., 2020, Space Sci. Rev., 216, 68

Glover S. C. O., Clark P. C., 2012, MNRAS, 421, 9

Glover S. C. O., Mac Low M.-M., 2007, ApJS, 169, 239

Greggio L., Tosi M., Clampin M., De Marchi G., Leitherer C., et al., 1998, ApJ, 504, 725

Haardt F., Madau P., 1996, ApJ, 461, 20

Haid S., Walch S., Seifried D., Wünsch R., Dinnbier F., et al., 2018, MNRAS, 478, 4799

Harris W. E., 1991, ARA&A, 29, 543

Harris J., Calzetti D., Gallagher John S. I., Smith D. A., Conselice C. J., 2004, ApJ, 603, 503

Heckman T. M., 1997, in Holt S. S., Mundy L. G., eds, American Institute of Physics Conference Series Vol. 393, The Seventh Astrophysical Conference: Star formation, near and far. pp 271–278, doi:10.1063/1.52791

Heiles C., Troland T. H., 2005, Astrophys. J., 624, 773

Hennebelle P., Falgarone E., 2012, A&A Rev., 20, 55

Hernquist L., 1990, ApJ, 356, 359

Herrera C. N., Boulanger F., Nesvadba N. P. H., Falgarone E., 2012, A&A, 538, L9

Heyer M. H., Brunt C. M., 2004, ApJ, 615, L45

Heyer M., Dame T. M., 2015, ARA&A, 53, 583

Heyer M. H., Carpenter J. M., Snell R. L., 2001, The Astrophysical Journal, 551, 852

Heyer M., Krawczyk C., Duval J., Jackson J. M., 2009, ApJ, 699, 1092

Hislop J. M., Naab T., Steinwandel U. P., Lahén N., Irodotou D., et al., 2022, MNRAS, 509, 5938

Hogg D. W., Phinney E. S., 1997, ApJ, 488, L95

Holtzman J. A., Faber S. M., Shaya E. J., Lauer T. R., Groth J., et al., 1992, AJ, 103, 691

Hopkins P. F., 2013, MNRAS, 428, 2840

Hopkins P. F., Cox T. J., Kereš D., Hernquist L., 2008, ApJS, 175, 390

Hopkins P. F., Quataert E., Murray N., 2012, MNRAS, 421, 3488

Hopkins P. F., Wetzel A., Kereš D., Faucher-Giguère C.-A., Quataert E., et al., 2018, MNRAS, 480, 800

Hoyle F., Ellis G. R. A., 1963, Australian Journal of Physics, 16, 1

Hu C.-Y., Naab T., Walch S., Moster B. P., Oser L., 2014, MNRAS, 443, 1173

Hu C.-Y., Naab T., Walch S., Glover S. C. O., Clark P. C., 2016, MNRAS, 458, 3528

Hu C.-Y., Naab T., Glover S. C. O., Walch S., Clark P. C., 2017, MNRAS, 471, 2151

Hunter D. A., Elmegreen B. G., Dupuy T. J., Mortonson M., 2003, AJ, 126, 1836

Jeffreson S. M. R., Kruijssen J. M. D., Keller B. W., Chevance M., Glover S. C. O., 2020, MNRAS, 498, 385

Jeffreson S. M. R., Keller B. W., Winter A. J., Chevance M., Kruijssen J. M. D., et al., 2021, MNRAS, 505, 1678

Jenkins E. B., Tripp T. M., 2011, ApJ, 734, 65

Johnson K. E., Leitherer C., Vacca W. D., Conti P. S., 2000, AJ, 120, 1273

Johnson K. E., Leroy A. K., Indebetouw R., Brogan C. L., Whitmore B. C., et al., 2015, ApJ, 806, 35

Karakas A. I., 2010, MNRAS, 403, 1413

Kauffmann G., Guiderdoni B., White S. D. M., 1994, MNRAS, 267, 981

Kennicutt R. C., Evans N. J., 2012, ARA&A, 50, 531

Kennicutt Robert C. J., Lee J. C., Funes J. G., Sakai S., Akiyama S., 2005, in de Grijs R., González Delgado R. M., eds, Astrophysics and Space Science Library Vol. 329, Starbursts: From 30 Doradus to Lyman Break Galaxies. p. 187, doi:10.1007/1-4020-3539-x_33

Kepley A. A., Leroy A. K., Johnson K. E., Sandstrom K., Chen C. H. R., 2016, ApJ, 828, 50

Kim C. G., Ostriker E. C., 2015, Astrophys. J., 802, 99

Kim C.-G., Ostriker E. C., 2017, ApJ, 846, 133

Klessen R. S., 2000, ApJ, 535, 869

Koudmani S., Sijacki D., Smith M. C., 2022, MNRAS, 516, 2112

Kroupa P., 2001, MNRAS, 322, 231

Krumholz M. R., McKee C. F., 2005, ApJ, 630, 250

Lada C. J., Lada E. A., 2003, ARA&A, 41, 57

Lada E. A., Bally J., Stark A. A., 1991, ApJ, 368, 432

Lahén N., Naab T., Johansson P. H., Elmegreen B., Hu C.-Y., et al., 2019, ApJ, 879, L18

Lahén N., Naab T., Johansson P. H., Elmegreen B., Hu C.-Y., et al., 2020, ApJ, 891, 2

Lahén N., Naab T., Kauffmann G., 2022, MNRAS, 514, 4560

Larson R. B., 1974, MNRAS, 169, 229

Larson R. B., 1981, MNRAS, 194, 809

Leroy A. K., Bolatto A. D., Ostriker E. C., Rosolowsky E., Walter F., et al., 2015, ApJ, 801, 25

Leroy A. K., Bolatto A. D., Ostriker E. C., Walter F., Gorski M., et al., 2018, ApJ, 869, 126

Lípari S. L., Díaz R. J., Forte J. C., Terlevich R., Taniguchi Y., et al., 2004, MNRAS, 354, L1

Lombardi M., Alves J., Lada C. J., 2010, A&A, 519, L7

Lotz J. M., Jonsson P., Cox T. J., Croton D., Primack J. R., et al., 2011, ApJ, 742, 103

Mac Low M.-M., Ferrara A., 1999, ApJ, 513, 142

Mac Low M.-M., McCray R., 1988, Astrophys. J., 324, 776

MacKey J., Gvaramadze V. V., Mohamed S., Langer N., 2015, Astron. Astrophys., 573, 10

Marín-Franch A., Aparicio A., Piotto G., Rosenberg A., Chaboyer B., et al., 2009, ApJ, 694, 1498

Martin C. L., Kobulnicky H. A., Heckman T. M., 2002, ApJ, 574, 663

Mas-Hesse J. M., Kunth D., 1999, A&A, 349, 765

Mateo M. L., 1998, ARA&A, 36, 435

Mathis J. S., Rumpl W., Nordsieck K. H., 1977, ApJ, 217, 425

McConnachie A. W., 2012, AJ, 144, 4

McKee C. F., Ostriker J. P., 1977, ApJ, 218, 148

McKee C. F., Ostriker E. C., 2007, ARA&A, 45, 565

McKee C. F., Li P. S., Klein R. I., 2010, ApJ, 720, 1612

McQuinn K. B. W., Skillman E. D., Cannon J. M., Dalcanton J., Dolphin A., et al., 2010, ApJ, 724, 49

McQuinn K. B. W., Mitchell N. P., Skillman E. D., 2015, ApJS, 218, 29

Meurer G. R., 2000, in Lançon A., Boily C. M., eds, Astronomical Society of the Pacific Conference Series Vol. 211, Massive Stellar Clusters. p. 81 (arXiv:astro-ph/0003161)

Mierkiewicz E. J., Reynolds R. J., Roesler F. L., Harlander J. M., Jaehnig K. P., 2006, ApJ, 650, L63

Moore B., Ghigna S., Governato F., Lake G., Quinn T., et al., 1999, ApJ, 524, L19

Motte F., Andre P., Neri R., Abergel A., 1998, in Yun J., Liseau L., eds, Astronomical Society of the Pacific Conference Series Vol. 132, Star Formation with the Infrared Space Observatory. p. 163

Motte F., André P., Ward-Thompson D., Bontemps S., 2001, A&A, 372, L41

Naab T., Ostriker J. P., 2017, ARA&A, 55, 59

Navarro J. F., Frenk C. S., White S. D. M., 1995, MNRAS, 275, 56

Nelson R. P., Langer W. D., 1997, ApJ, 482, 796

Ochsendorf B. B., Zinnecker H., Nayak O., Bally J., Meixner M., et al., 2017, Nature Astronomy, 1, 784

Oka T., Hasegawa T., Sato F., Tsuboi M., Miyazaki A., et al., 2001, ApJ, 562, 348

Patton D. R., Qamar F. D., Ellison S. L., Bluck A. F. L., Simard L., et al., 2016, MNRAS, 461, 2589

Price D. J., 2012, Journal of Computational Physics, 231, 759

Puls J., Vink J. S., Najarro F., 2008, Astron. Astrophys. Rev., 16, 209

Rathjen T.-E., Naab T., Girichidis P., Walch S., Wünsch R., et al., 2021, MNRAS, 504, 1039

Reynolds R. J., Scherb F., Roesler F. L., 1973, ApJ, 185, 869

Ripple F., Heyer M. H., Gutermuth R., Snell R. L., Brunt C. M., 2013, MNRAS, 431, 1296

Robertson B., Bullock J. S., Font A. S., Johnston K. V., Hernquist L., 2005, The Astrophysical Journal, 632, 872

Rodriguez-Gomez V., Pillepich A., Sales L. V., Genel S., Vogelsberger M., et al., 2016, MNRAS, 458, 2371

Rosolowsky E., 2005, PASP, 117, 1403

Röttgers B., Naab T., Cernetic M., Davé R., Kauffmann G., et al., 2020, MNRAS, 496, 152

Rupke D. S. N., Veilleux S., 2011, ApJ, 729, L27

Saitoh T. R., Daisaka H., Kokubo E., Makino J., Oakmoto T., et al., 2010, in Smith B., Higdon J., Higdon S., Bastian N., eds, Astronomical Society of the Pacific Conference Series Vol. 423, Galaxy Wars: Stellar Populations and Star Formation in Interacting Galaxies. p. 185 (arXiv:1101.3708), doi:10.1017/s1743921311000846

Sampath R., Montanari N., Akinci N., Prescott S., Smith C., 2016, Journal of Ocean Engineering and Marine Energy, 2, 313

Satyapal S., Ellison S. L., McAlpine W., Hickox R. C., Patton D. R., et al., 2014, MNRAS, 441, 1297

Schaerer D., Contini T., Kunth D., 1999, A&A, 341, 399

Schulte-Ladbeck R. E., Hopp U., Greggio L., Crone M. M., Drozdovsky I. O., 2001, AJ, 121, 3007

Scudder J. M., Ellison S. L., Torrey P., Patton D. R., Mendel J. T., 2012, MNRAS, 426, 549

Seifried D., Walch S., Girichidis P., Naab T., Wünsch R., et al., 2017, Monthly Notices of the Royal Astronomical Society, 472, 4797

Shadloo M., Oger G., Le Touzé D., 2016, Computers & Fluids, 136, 11

Simpson C. M., Pakmor R., Marinacci F., Pfrommer C., Springel V., et al., 2016, Astrophys. J., 827, L29

Smith B. J., Struck C., Hancock M., Appleton P. N., Charmandaris V., et al., 2007, AJ, 133, 791

Smith M. C., Bryan G. L., Somerville R. S., Hu C.-Y., Teyssier R., et al., 2021, MNRAS, 506, 3882

Solomon P. M., Rivolo A. R., Barrett J., Yahil A., 1987, ApJ, 319, 730

Spitzer L., 1978, Physical Processes in the Interstellar Medium. Wiley, doi:10.1002/9783527617722

Springel V., 2005, MNRAS, 364, 1105

Springel V., 2010, MNRAS, 401, 791

Springel V., Pakmor R., Pillepich A., Weinberger R., Nelson D., et al., 2017, Monthly Notices of the Royal Astronomical Society, 475, 676

Steinwandel U. P., Moster B. P., Naab T., Hu C.-Y., Walch S., 2020, MNRAS, 495, 1035

Stinson G. S., Dalcanton J. J., Quinn T., Kaufmann T., Wadsley J., 2007, ApJ, 667, 170

Strong A. W., Moskalenko I. V., Ptuskin V. S., 2007, Annual Review of Nuclear and Particle Science, 57, 285

Tan J. C., Beltrán M. T., Caselli P., Fontani F., Fuente A., et al., 2014, in Beuther H., Klessen R. S., Dullemond C. P., Henning T., eds, Protostars and Planets VI. p. 149 (arXiv:1402.0919), doi:10.2458/azu_uapress_9780816531240-ch007

Testi L., Sargent A. I., 1998, ApJ, 508, L91

Thornley M. D., Förster Schreiber N. M., Lutz D., Genzel R., Spoon H. W. W., et al., 2000, ApJ, 539, 641

Tolstoy E., Hill V., Tosi M., 2009, ARA&A, 47, 371

Toomre A., Toomre J., 1972, ApJ, 178, 623

Tremonti C. A., Calzetti D., Leitherer C., Heckman T. M., 2001, ApJ, 555, 322

Tumlinson J., Peeples M. S., Werk J. K., 2017, Annu. Rev. Astron. Astrophys., 55, 389

Vázquez-Semadeni E., Colín P., Gómez G. C., Ballesteros-Paredes J., Watson A. W., 2010, ApJ, 715, 1302

Wakelam V., Bron E., Cazaux S., Dulieu F., Gry C., et al., 2017, Molecular Astrophysics, 9, 1

Walch S., Girichidis P., Naab T., Gatto A., Glover S. C. O., et al., 2015, MNRAS, 454, 238

Weaver R., McCray R., Castor J., Shapiro P., Moore R., 1977, Astrophys. J., 218, 377

Webber W. R., Lockwood J. A., 2001, J. Geophys. Res., 106, 29323

Westera P., Lejeune T., Buser R., Cuisinier F., Bruzual G., 2002, A&A, 381, 524

White S. D. M., Frenk C. S., 1991, ApJ, 379, 52

Whitmore B. C., Chandar R., Schweizer F., Rothberg B., Leitherer C., et al., 2010, AJ, 140, 75

Wiersma R. P. C., Schaye J., Smith B. D., 2009, MNRAS, 393, 99

Williams J. P., de Geus E. J., Blitz L., 1994, ApJ, 428, 693

Wolfire M. G., McKee C. F., Hollenbach D., Tielens A. G. G. M., 2003, ApJ, 587, 278

Zeeman P., 1897, Nature, 55, 347

Zhang Q., Fall S. M., 1999, ApJ, 527, L81